# The Measurement of Radical Species of Atmospheric Importance

A Thesis Submitted for the degree of Doctor of Philosophy

by

Claire Louise Bell


Christ Church, University of Oxford

Trinity Term, 2010

**The Measurement of Radical Species of Atmospheric Importance**

Claire Louise Bell, Christ Church

A thesis submitted for the degree of Doctor of Philosophy

Trinity Term, 2010

## Abstract

The measurement of radical species in the atmosphere has far reaching implications. For example, it is necessary to both understand and improve our knowledge of radicals in the atmosphere to better inform the models which in many cases are the best way of predicting future air quality and climate change. Although many of these models are often not fully representative of all the processes occurring, they are the current best estimate based on the knowledge available, and can be useful in informing and directing future policy. The numerous, varied and interlinked cycles in the atmosphere are complex and only by obtaining data on specific species can accurate concentrations be retrieved and fed back into the models to improve their accuracy.

This work is concerned with the development and application of an ultra-sensitive absorption spectroscopy technique to the problem of detection of the peroxy radical, $HO_2$. Noise Immune Cavity Enhanced Optical Heterodyne Molecular Spectroscopy (NICE-OHMS) combines cavity enhancement tech-

niques (in order to increase the path length) with frequency and wavelength modulation techniques (in order to reduce the noise).

Following a discussion of the current detection methods used by atmospheric scientists to accurately measure and quantitative concentrations, some preliminary work on the detection of ammonia by a simple cavity enhanced absorption setup is presented. Pressure broadening and shift results were obtained for a number of ammonia transitions in the near infrared region, broadened by He, Ne, Ar, Xe, $O_2$ and $N_2$.

The bulk of the work concentrates on the implementation of the NICE-OHMS technique, presenting the first results with the use of an external cavity diode laser and a ring shaped cavity. A sensitivity of $4 \times 10^{-11}$ $cm^{-1}$ $Hz^{-1/2}$ is obtained on an individual rovibrational transition of methane at 6610.063 $cm^{-1}$, along with a selection of other data from the atmospherically important molecules methane, nitrogen dioxide and carbon dioxide, highlighting the broad wavelength range over which the instrument can operate. Finally, the NICE-OHMS technique is used to probe $HO_2$ radicals formed through the photolysis of a $Cl_2/CH_3OH/O_2$ mixture. Following the creation and detection of $HO_2$ radicals in the cavity, and based on the optimum sensitivity outlined above, a minimum concentration of $1 \times 10^9$ molecules $cm^{-3}$ has been demonstrated.

# Acknowledgements

An inordinate number of people have worked tirelessly over the past 4 years, both directly and indirectly helping and supported me throughout, culminating in this work. Two sheets of paper in the front of a thesis seems an underwhelming way to represent the enormous debt of gratitude I owe to so many people, but I hope that it goes some of the way. Perhaps the rest of the way might be accomplished with beverages.

Firstly, I must thank Gus for allowing me to come and work in his group. Crossing the car park four years ago (leaving my colouring pencils behind) was, I thought, a brave decision on my part. However, that was nothing to the trust that Gus put in me, for which I am very grateful. My somewhat unorthodox and eclectic mix of experiences previously to arriving here would (should!) have discouraged lesser supervisors, and so to Gus, thank you.

In the same vein, to Grant I also owe a huge amount. From the outset, answering my "interview" question of "tell me something interesting about geochemistry" with a puzzled stare, rather set the tone for the next 4 years. In the gaps between the "fluffy bunny" quips, a huge thank you must go to Grant for all his day to day guidance and support, something this thesis would not exist without.

Dr Pev, your patience knows no bounds, and well I have tried to find them! From my first trip into your office, holding a glass cell at the ends with my fingers all over the windows, your patient correction and tutelage has enabled the continued correction of my (and NICE-OHMS') experimental errors, the development of my chemistry and physics knowledge and an added bonus of my squash and cricket. In what proportions, I will leave to you. For everything, thank you.

JP – you have been amazing, thank you so much for everything. You were undoubtedly delighted when Nicola so generously left NICE-OHMS in your care, but your tireless trekking to the end lab to poke the electronics or try to get the experiment to lock (weather permitting) has not gone un-noticed. Particular thanks go to you for your un-

failing presence in the lab - when helping me to finish everything off, your help has been invaluable – I simply could not have done it without you, so thank you. The exchange of weeks of your time for the odd quirky English word to add to your vocabulary doesn't really seem fair!

To Nicola, apart from the bit where you left me (!), your support and help has been what has kept me here. Your patience teaching me the intricacies of the experiment was limitless and I hope you are happy to see the years of work you put in come to fruition. For keeping the experiment working, Kevin and Neville and everyone in electronics and workshops, your help and detailed knowledge has been invaluable. Your ability to decipher what the problem is from little more than my bringing it to you and smiling is astonishing, and your work is never unappreciated. To Paul and lab services, you have simply held the place together, so thank you.

The members, past and present, of the Hancock and Ritchie group are too numerous to thank individually, but are collectively fantastic. You make this group a great place to be. Particular thanks must go to the fellow (some time) end lab occupants; Stuart, you provided hours of amusement, keeping me on my (nano) toes, and Katy and Ann, thank you for being wonderful part IIs and now D.Phils. – you have been a pleasure to share a lab with, and I thank you for your friendship. Tom, although the only Part II who hasn't wanted to stay (!), you too were amazing. Together we have championed NICE-OHMS sufficiently well (fingers crossed) so that it avoids the wrecking ball, and can move to a new home – so congratulations! To the rest of the group, thank you for being you – keep it up, the people are what make this group. GraHam, keep your pranks razor sharp, don't slack off! I look forward to seeing everyone at group dinners in the future!

Finally, but most importantly, I owe everything to Mark and my Mum and Dad. You have provided support all the way through, whatever I decided I wanted to do and for that I am grateful. Mark, from the outset of starting this project, you encouraged and supported me throughout everything, and I would not be still standing at the end of it without you. You are amazing - thank you.

# Contents

## 6. Future Directions for NICE-OHMS

# Chapter 1
# Introduction to methods for atmospheric detection

## 1.1. Atmospheric Sensing

Accurate measurements of the absolute concentrations of trace gases present in the atmosphere are invaluable for better understanding of atmospheric processes and their impact on earth systems. Atmospheric events such as photochemical smog can be exceptionally hazardous to human health and so accurate understanding of the processes occurring and their outcomes are essential. Field measurements add tremendous value to theoretical modelling

thus driving the development of increasingly effective measurement techniques [1]. Trace gas monitoring is an enormous field which presents a bewildering array of measurement challenges. For example, the atmospheric lifetime of species can vary from many years through to fractions of a second; requirements for measurement locations can present hostile, inaccessible or transient environments, and complex interactions and cycles between atmospheric species require accurate modelling to be undertaken. Much trust is placed in climate models which predict various future climate scenarios, on which many important and far reaching global economic decisions are based. Accurate measurement of atmospheric species is imperative to verify and refine the models on which such important decisions are based.

This introductory chapter aims to provide an overview of the work presented in this thesis, followed by a discussion of the role that certain species of atmospheric importance play in atmospheric chemistry. These species have been selected as they play a critical role in tropospheric cycling of $HO_2$, the hydroperoxyl radical, for which a new method of detection is presented in this thesis. The remainder of this chapter highlights some important examples of trace gas detection in the atmosphere, demonstrating, by virtue of the broad range of techniques applied to their detection, the various requirements that each species demands.

## 1.2. Overview of the thesis

The work presented in this thesis involves the use of diode lasers and optical cavities to perform absorption spectroscopy on trace gases of atmospheric importance. As outlined in this chapter, the preferred method of detection depends on the atmospheric concentrations of the species under investigation; the lower the concentration, the larger the measurement challenge and as a result the more experimentally complex the detection technique required. For species which have concentrations on the ppb (parts per billion) level, such as ammonia, their detection can involve the use of the relatively simple experimental cavity technique of cavity enhanced absorption spectroscopy (CEAS). In Chapter 2, a full theoretical description of the CEAS technique is given. As well as using this technique to perform relatively sensitive detection of ammonia, results are presented involving more specific transition properties, including pressure broadening and shift coefficients for a selection of rare gas colliders.

Following on from the relatively simple technique of CEAS presented in Chapter 2, starting from Chapter 3 the thesis focuses on the more taxing detection requirements for radical species such as $HO_2$, employing absorption within a resonant optical cavity. With the daytime maximum concentrations

$HO_2$ around 2 x $10^8$ $cm^{-3}$ (10 ppt), improvements in the minimum detection sensitivity must be implemented in order to meet the detection requirements. In an attempt to meet these particularly stringent detection requirements with absorption spectroscopy, there is currently only one technique which has reached the required sensitivity: Noise Immune Cavity Enhanced Optical Heterodyne Molecular Spectroscopy (NICE-OHMS) [2]. The remainder of the thesis is concerned with the theory, experimental implementation, characterisation and measurements involving a diode laser based NICE-OHMS spectrometer.

Chapter 3 outlines the various techniques such as locked-CEAS, frequency modulation spectroscopy (FMS) and wavelength modulation spectroscopy (WMS) which are combined together in the NICE-OHMS technique in order to attain higher sensitivities. Each technique is discussed individually, including its theoretical description, with specific relevance to the NICE-OHMS experimental technique. Following this, a description of the synergic combination of these techniques is discussed resulting in the full NICE-OHMS signals being elicited.

Having discussed the relevant theory for the NICE-OHMS technique, Chapter 4 moves on to the experimental implementation of the various techniques in

the setup, and characterising the performance of the setup by sensitive analysis of a selection of trace gases including $CH_4$, $N_2O$ and $CO_2$. As well as presenting the first application of the NICE-OHMS technique in an optical ring cavity, the most sensitive detection results to date for a NICE-OHMS spectrometer using an external cavity diode laser (ECDL) are presented.

Finally, building on the characterisation work outlined in Chapter 4, Chapter 5 moves to the application of the NICE-OHMS technique to the detection of atmospherically important $HO_2$. The method of generating $HO_2$ within the cavity is outlined, including a kinetic study of the reactions involved. Following this, results are presented for $HO_2$ detection, with a study of potential interfering species as part of the $HO_2$ verification process. This work constitutes the first measurements of radical species of atmospheric importance with a laboratory based NICE-OHMS spectrometer, including the significant progression towards direct measurements of $HO_2$. The thesis ends with a critique of the method and its possible improvements.

## 1.3. Detection methods for trace gases

With their critical importance to science policy makers, climate scientists and atmospheric chemists alike, the measurement of trace gases in the atmosphere

is a crucial input to climate models. When measuring trace gases, particularly in the field, as well as achieving detection at the necessary sensitivity, it is also highly desirable that any detection system can operate at room temperature and pressure, without the need for extensive sample preparation. It is also an important requirement that absolute number densities of molecules can be obtained.

Furthermore, when detecting trace gases in the atmosphere, as well as retrieving absolute concentrations of species, determining the isotopic composition can often be very useful as it can indicate the origin of a certain compound e.g. discerning anthropogenic $CO_2$ from biogenic sources of $CO_2$. A technique which can be applied for this purpose, is gas chromatography isotope ratio mass spectrometry (GC-IRMS), which can achieve very precise measurements, within 0.1 % accuracy [3]. For example, Rice *et al*, [4] use GC-IRMS to monitor formaldehyde concentrations in urban air via the measurement of carbon and hydrogen isotope ratios. Given the relatively short lifetime of formaldehyde in the atmosphere (of the order of hours) and its temporal variability, a method that can provide temporal resolution is particularly advantageous. However, despite the impressive accuracies that instruments such as these can reach, they are less than practical for field

measurements, due to time consuming requirements such as sample preparations, and physical size and cost of the instrument.

A more practical approach involves the use of laser based absorption spectroscopy which can produce the requirement of quantitative measurements at a sufficiently sensitive level. In order to minimise the economic outlay, it is highly desirable to utilise established laser technology. The availability of relatively cheap laser sources in the near-infrared (NIR) means that these laser sources are integral to many of these detection systems. Their commercial importance in the telecommunications industry drives their ongoing development, resulting in lasers being available at a wide range of wavelengths (375 - 2700 nm) with suitable powers and narrow linewidths [5]. Furthermore, developments in Quantum Cascade Lasers (QCLs), enables expansion into the ca. 3 - 300 μm range [6].

With laser based absorption spectroscopy enabling selective measurements to be undertaken, the most appropriate detection scheme in terms of sensitivity must be investigated. Direct absorption spectroscopy over extended path lengths could be used; initially this was by the use of multi pass cells, such as Herriott [7] or White [8] cells giving rise to interaction lengths of tens of metres. Coupled with the addition of a noise reducing technique such as

wavelength modulation spectroscopy (WMS), minimum detectable absorption coefficients (detection sensitivities) of the order of 4 x $10^{-9}$ $cm^{-1}$ $Hz^{-1/2}$ can be achieved [9].

Another technique experiencing a renaissance from its origins in the 1880s is the photoacoustic effect (PA) [10]. The photoacoustic effect is based on the detection of acoustic waves produced by the absorption of pulsed or modulated laser radiation and the subsequent transient localized heating and expansion in a gas. The absorption of modulated laser radiation generates an acoustic signal, which can be amplified by tuning the modulation frequency to one of the acoustic resonances of the sample cell, e.g. a longitudinal mode in a cylindrical chamber. In this resonant case the cell works as an acoustic amplifier and the photoacoustic signal is amplified by the Q factor of the resonance which usually is in the range between 10 and 300; the signal is proportional to the optical power on the sample. With this zero background technique, sensitivities of ~ $10^{-10}$ $cm^{-1}$ $Hz^{-1/2}$ can be achieved [11].

The benefits of utilising a long path length for trace gas monitoring has been outlined with the use of multi pass cells. An alternative absorption based technique is long path Differential Optical Absorption Spectroscopy (DOAS) [12] which has been used for detection of $NO_2$, IO and BrO along with $SO_2$

[13]. However, with the advent of very highly reflective mirrors working in the spectral region of interest, optical cavities are especially useful in trace gas detection. With high mirror reflectivities (~0.9997) path length enhancements result in interaction lengths of kilometres in a tabletop setup, meaning that optical cavity techniques are particularly suitable for application to trace gas detection. There are currently a number of cavity based detection techniques which have been employed in atmospheric detection, such as the use of a broadband CEAS spectrometer to measure $NO_2$ [14], $NO_3$ [15] and $I_2$ [16], and Cavity Ring Down Spectroscopy (CRDS) measurements on $NO_3$ [17] and IO [18], and a few of these techniques are now briefly outlined.

### 1.3.1. Examples – Broadband CEAS

As will be outlined in the following section, NO and $NO_2$ are important in ozone creation; NO and $NO_2$ (collectively known as $NO_x$) undergo catalytic photochemical cycling, the net result of which provides the principal source of tropospheric ozone [19]. Ozone is a respiratory irritant and thus a hazardous component of urban photochemical smog. Ozone photochemistry also produces hydroxyl radicals which are key tropospheric oxidants during the day, and reaction of $NO_2$ with ozone produces the $NO_3$ radical which is an important oxidant at night.

Broadband cavity enhanced absorption spectroscopy (BB-CEAS) was introduced in 2003 by Fiedler *et al*. who employed a short-arc Xenon lamp to record absorption features of oxygen and gaseous azulene [20]. The advantages of utilising BB-CEAS include a broad wavelength range over which multiple species can be detected at the same time, enabling more specific targeting of spectral regions in order to avoid interfering species. As well as specific targeting of spectral regions containing isolated transitions, BB-CEAS has the flexibility to record spectra related to broadband absorbers.

CEAS involves measuring the transmitted light intensities through an optical cavity, consisting of two highly reflective mirrors between which the light is reflected multiple times, thereby greatly increasing the effective path length. The change in the time integrated intensity of the transmitted light with and without an absorber can be related to the concentration of the absorbing species present. In order to provide quantitative measurement of gas concentrations, it is necessary to know both the reflectivity values of the cavity mirrors by wavelength, and to perform regular calibrations. The wavelength dependent absorption coefficient of the gas sample is given by [14]:

$$\alpha(\lambda) = \left( \frac{I_0(\lambda)}{I(\lambda)} - 1 \right) \times \frac{1 - R(\lambda)}{d} \qquad \textbf{Equation 1.1}$$

where $I(\lambda)$ is the light intensity transmitted through the cavity when an absorbing gas sample is present within the cavity, $I_0(\lambda)$ is the intensity transmitted when the cavity is flushed with an non-absorbing gas, $d$ is the cavity length, and $R(\lambda)$ *is* the wavelength dependent reflectivity of the mirrors. It is necessary to know $R(\lambda)$ accurately, and this can be achieved in the field by calibration with the use of an absorber with a specific transition of well characterised parameters.

Langridge *et al* [14] used a BB-CEAS instrument based upon a light emitting diode (LED) to record absolute NO and $NO_2$ concentrations compared to that of a commercial chemiluminescence analyser and found good agreement.

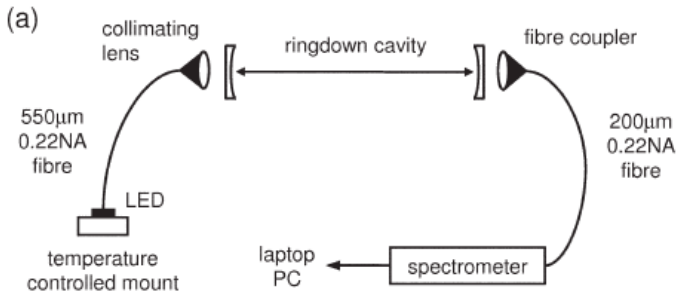


**Figure 1.1 - BB-CEAS setup**

Coupled with the flexibility of the instrument, the potential for further application of LED based BB-CEAS to compact atmospheric field instruments

is far reaching. In addition to $NO_2$, a wide range of species that absorb throughout the visible and near UV spectrum are accessible without significant modification of the experimental approach: in principle, only the light source and the cavity mirrors need be exchanged to access a different wavelength range. The experimental setup, shown in Figure 1.1 shows the simple nature of the technique, and indeed its applicability to field sensing requirements.

Following the development of the BB-CEAS technique, a number of field studies have exploited its compact and portable nature, including the measurement of molecular iodine in marine environments [21]. Iodine chemistry has an important impact on the trace gas composition of the marine boundary layer. $I_2$ undergoes solar photolysis and the subsequent I atoms react with ozone to form IO radicals which drive catalytic cycles and act to deplete tropospheric ozone. They also affect the oxidising capacity of the coastal atmosphere by perturbing the partitioning within the $NO_2$/NO and $HO_2$/OH radical families [22, 23, 24]. The iodine measurements were taken at the sample site with spectra recorded over the spectral range 522 - 554 nm, a region in which $I_2$ exhibits characteristic and highly structured absorption bands. The detection limit of the system for $I_2$ was around 25 pptv (parts per

trillion by volume) for an integration time of 7.5 s, thus allowing the emission of even small quantities of $I_2$ to be monitored at high time resolution, broadening the diversity of seaweed species (which emit $I_2$) under investigation.

The application of a portable and flexible cavity based trace gas detection scheme to this situation has enabled some interesting conclusions to be drawn, not available with previous measurement techniques. Molecular iodine is notoriously difficult to measure in the field due to its specific spatial variability dependent on time, tide and species of plant. Similarities between seaweed species not previously believed to exist were found due to the fast time resolution of the BB-CEAS detection method, notably that large emitters of $I_2$ (such as *L. digitata*) produce a burst of $I_2$ when first exposed to air. It was also noted that the strongest hotspots are likely to be found over areas of kelp species in the first few minutes after having been exposed by a receding tide, which is useful for temporal modelling. Although examples of seaweed species similarities are beyond the scope of this thesis, it can be seen from this example that the application of a simple BB-CEAS technique to field measurements can progress the understanding, enabling better modelling and directing future studies [25].

Direct transference of such a portable technique, covering a broad wavelength range, as discussed above, to the detection of transient species and highly reactive molecules, such as radicals (OH, $HO_2$, $NO_3$ or IO), is not immediately possible as their short lived nature results in lower concentrations than can be detected by this system. Furthermore, species such as these cannot be collected and transported to a laboratory for analysis, and so they must be measured in-situ. Cavity ring down spectroscopy (CRDS) is an alternative sensitive absorption based technique which is capable of detecting target species below the 1 ppbv level.

### 1.3.2. Examples – Cavity Ring Down Spectroscopy

CRDS has been used as a sensitive absorption technique for a number of years, being first described in 1988 [26], but since the development of appropriate dielectric highly reflective mirrors, the number of applications to which CRDS has been applied has increased. CRDS employs a similar setup to CEAS, i.e. an optical cavity is constructed between two very highly reflective mirrors. However, rather than measuring the change in light intensity of light exiting the cavity both with and without an absorber present, CRDS measures the loss rate of light intensity from the cavity when the source is abruptly switched off, allowing the cavity to "ring down". A time domain measurement is

advantageous as it is free from laser intensity fluctuations that decrease the sensitivity of direct laser absorption techniques, and as such is generally more sensitive than CEAS.

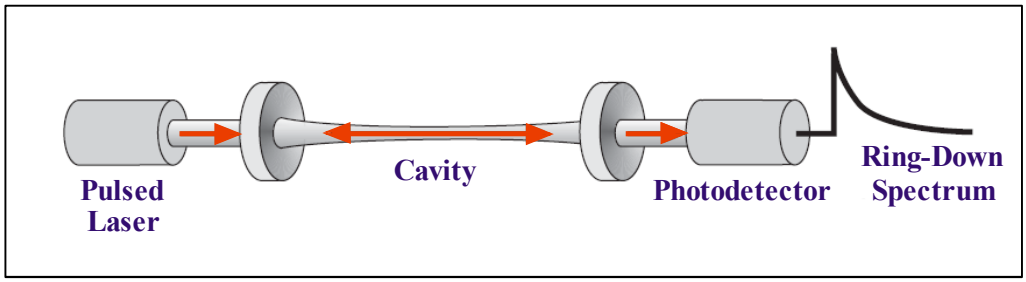


**Figure 1.2 – A Cavity Ring-Down Experimental setup. From the ring-down times taken for the cavity with and without the absorbing species concentrations of absorbing species can be deduced [27].**

The intensity of light exiting the cavity decays exponentially with time according to [28]:

$$I_{CRD}(t) \;\alpha\; \int_0^{\infty} I(\nu)\exp\left[-\frac{t}{\tau(\nu)}\right]\, d\nu \qquad \textbf{Equation 1.2}$$

where $I(\nu)$ is the spectral intensity distribution of the incident laser light pulse, and $\tau(\nu)$ is the cavity ring-down time (CRD time), defined as the time taken for the intensity exiting the cavity to decay to 1/e of its initial value. In an empty cavity the ring-down time $\tau_0(\nu)$, is solely dependent on losses at the mirrors. Typical ring-down times for field instrumental setups are on the order of tens of μs, corresponding to path lengths in the range 1-30 km travelled by the light [17]. As described previously, the increase in path length afforded is the root

of the sensitivity in CRDS, with the added benefit of it being a time domain measurement conducted within a compact instrumental housing.

When considering atmospheric trace gas detection, CRDS has often been used to measure the $NO_3$ radical [17], due to its importance in night time atmospheric cycles, and a good match between commercially available laser sources, suitably coated highly reflective mirrors and broad spectral regions free from interference from other absorbers [29].

The benefits afforded by using CRDS to measure atmospheric $NO_3$ include the possibility to perform air column analysis revealing the vertical structure, something not possible with the traditional techniques such as long path DOAS [30]. This is particularly important given the suggestion that the $NO_3$ concentrations in the night time boundary layer were not well represented in the previous approach to modelling which used input data from ground based observation techniques [31]. The requirement for better vertical spatial resolution when detecting $NO_3$ concentrations demonstrates the benefits of progressing laboratory based investigation with a view to develop spectrometers for field measurements, a topic with which the following chapters of this thesis is concerned. King *et al* [17] demonstrated the facility to measure $NO_3$ radical concentrations using a CRDS absorption spectrum with a

baseline noise of 1 x $10^{-9}$ $cm^{-1}$ in a 30 s acquisition time, being equivalent to a mixing ratio of 2 pptv for $NO_3$. They also represented the first in-situ measurements of $NO_3$ at fast timescales. Following on from this, the technique has been used in field campaigns on airborne craft, such as the NOAA WP-3D Orion aircraft used to fly tracts over the North-Eastern seaboard of the USA. A CRDS instrument was used to simultaneously collect $NO_3$ and $N_2O_5$ measurements on board the aircraft [32] with detection limits reported of 6 x $10^6$ $cm^{-3}$, corresponding to 0.2 pptv at 1 atm and 294K. Further developments in laser source stability, accurate correction for Rayleigh and Mie scattering losses and in-situ calibration methods in field instruments will improve their applicability to field based situations, increasing the accuracy and breadth of data for input to improve the atmospheric modelling.

So far in this discussion, the techniques under consideration have involved the detection of molecules, however, it is noted that aerosols are another important constituent of the atmosphere. Extending the measurement range to include measurement of aerosols presents an alternative set of challenges, to which cavity techniques have been applied. Atmospheric aerosols are important radiative forcing agents in the atmosphere; however the magnitude of this forcing is not well known, and so is insufficiently modelled. The

forcing effects of aerosols are determined by their optical properties, which depend not only on the physical characteristics of the aerosol (size, shape, etc.), but also on the wavelength-dependent refractive index of the particle medium. The measurement of aerosol optical properties to retrieve refractive index information is critical to understanding and predicting perturbations in the radiative balance of the atmosphere [33]. Measurements must be able to retrieve extinction data, morphology and refractive index information, presenting further challenges in detection techniques [34].

Having outlined a selection of direct monitoring examples and methods, focus now turns to the detection of the $HO_2$ radical, its importance in the atmosphere and possible improvements to its current detection by the implementation of cavity based absorption techniques.

## 1.4. The importance of $HO_2$ in the atmosphere

Radical species, such as OH and $HO_2$, control virtually all of the oxidative chemistry in the atmosphere, and they are responsible for the transformation of primary emissions into secondary pollutants such as $NO_2$, $O_3$ and particulates [36]. The complex atmospheric cycles which exist can be represented diagrammatically, as shown in Figure 1.3.

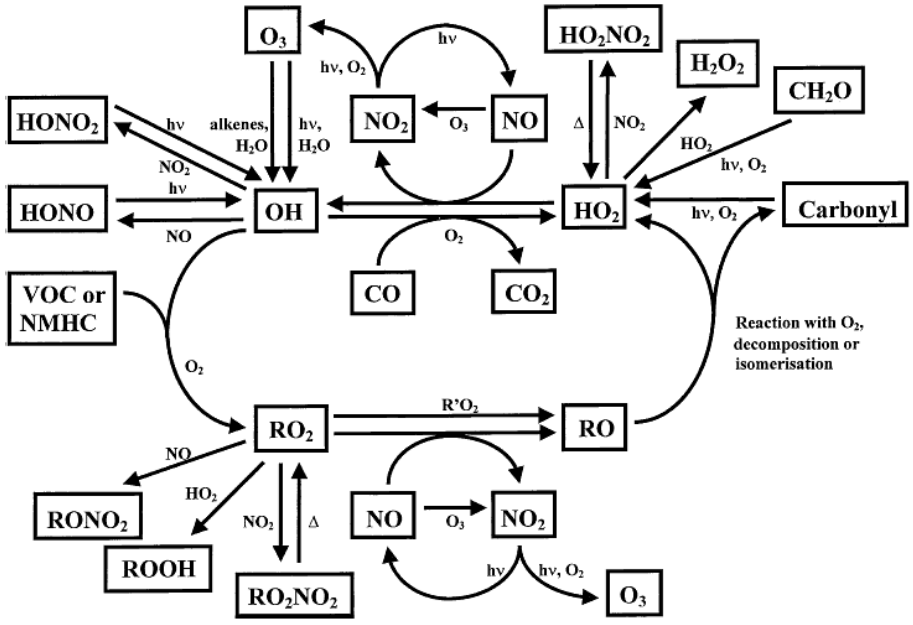


**Figure 1.3 Day-time tropospheric chemistry of the formation of $O_3$, $H_2O_2$, ROOH, $RONO_2$, $RO_2NO_2$, $HO_2NO_2$, HONO, $HONO_2$, $CH_2O$ and other carbonyls via OH initiated oxidation of Volatile Organic Compounds (VOCs) or non methyl hydrocarbons (NMHCs) and CO in the presence of NO and $NO_2$ [37].**

Important climate gases such as methane and ozone are also intricately related to the radical concentrations of $HO_2$. Their atmospheric lifetimes depend on the concentration of $HO_2$ which also controls the production of acidic species, with their well known detrimental effects to the environment. Current predictive models for future air quality and climate change necessarily contain complex chemical schemes. In order for these to be refined and improved, comparison with measurements of radicals in the present atmosphere constitutes the best validation of these schemes. It is often problematic when the measurement of these short lived species is technically too demanding,

and the lack of data for even a few of the input species can seriously limit the usefulness of the climate model. This has been evident when some field campaigns report significant discrepancies between models and in situ observations of OH and $HO_2$ radicals, for example in marine, forested and urban environments [35]. Although the proportional composition of these radical species (such as $HO_2$, OH, NO and $NO_2$) is very small, their chemistry is very important.

### 1.4.1. Current measurement techniques for $HO_2$

$HO_2$ provides a range of challenges when considering appropriate detection techniques. Atmospheric daytime levels of $HO_2$ are very small ($2 \times 10^8$ molecules $cm^{-3}$ (10 ppt)) and so require very sensitive detection techniques. It is desirable to use absorption spectroscopy as the detection technique as it offers the required selectivity and is absolute and may have the required sensitivity levels. In the UV portion of the spectrum, where optical techniques traditionally operate, the cross sections for electronic excitation of $HO_2$ are large, but yield a broad and structureless spectrum, and there is interference from other molecules and radicals, such as $RO_2$. Moving to the near-infrared region means that the spectra are far less congested, and although the

transitions are much weaker, diode laser spectroscopic techniques offer the potential for the prerequisite specificity and sensitivity. Currently, $HO_2$ is measured by the indirect techniques FAGE (Fluorescence Assay by Gas Expansion) which is essentially laser-induced fluorescence at low pressure [36, 37, 38, 39, 40, 41, 42], and PERCA (PEroxy Radical Chain Amplification) whereby $HO_2$ and $RO_2$ catalyse the oxidation of NO and CO into $CO_2$ and $NO_2$, which can then be measured [43, 44, 45, 46, 47]. Although FAGE specifically measures $HO_2$ (indirectly via its conversion into OH), PERCA measures the sum of all $RO_2$ and so it is desirable to have a direct and speciated technique.

#### 1.4.1.1. The FAGE Technique

The FAGE (Fluorescense Assay by Gas Expansion) method has provided an accurate and reliable method of detecting OH and hence $HO_2$ for a number of years [36], and is sufficiently robust to have been used in various field campaigns, such as NAMBLEX [36] and RHaMBLe [48]. The FAGE technique specifically measures OH by using laser induced fluorescence coupled with gas expansion, and measures $HO_2$ by first chemically converting it to OH by adding NO, and then proceeding with the detection regime, as outlined below. The initial reaction proceeds as follows:

$HO_2 + NO \rightarrow OH + NO_2$

The strong transition $A^2\Sigma^+$ (v′= 0) ← $X^2\Pi_i$ (v′′= 0) $Q_1(2)$ at 308 nm is used for the laser excitation of the OH as well as for the detection of the resultant fluorescence. In order to better discriminate between the desired laser induced fluorescence and the scattering from the source laser radiation, the laser induced flourescence is measured 50 ns after the laser source is switched off. Experiments are carried out at low pressures (~1 Torr) which also has the added benefit of both prolonging the lifetime of the fluorescence of the OH radical and reducing the interference effects of water vapour. The short time delay also avoids detector saturation, with the detector being inoperative during the duration of the laser pulse. The fluorescence process from which the concentrations of OH are measured competes with non-radiative collisional quenching at high pressures. Although the expansion leads to a reduction in the concentration of the OH radicals, this is more than compensated for by the increase in fluorescence quantum yields, due to the reduced collisional quenching of the OH $^2\Sigma^+$ excited state.

The size requirements of the system are quite large – having to house a suitable laser system, fluorescence detection system and calibration cells, data acquisition and calibration analysis equipment means that instruments used in field campaigns must be housed in large containers, up to 20 feet long.

Detection limits of $10^6$ - $10^7$ molecules $cm^{-3}$ for $HO_2$ have been achieved [49], however the system is complicated to use and does require careful calibration. Although suitable for detection requirements of long term static field campaigns, a more mobile, compact system would be beneficial, to enable better spatial coverage and ease of use.

### 1.4.1.2. The PERCA Technique

Peroxy radical chain amplification is an alternative, but still indirect, method of measuring the sum of all $RO_x$ in a sample. Although this technique is sensitive to the total concentration of $RO_x$ ($OH + HO_2 + RO + RO_2$), in reality with atmospheric concentrations of OH and RO being much lower than $HO_2$ and $RO_2$, the technique can be assumed to record concentrations of $HO_2$ and $RO_2$ only.

With the PERCA technique, the key features are to use NO and CO to convert $HO_2$ and $RO_2$ to $NO_2$, by reactions with an excess of NO, and subsequently recycle most of the OH products back to $HO_2$ (with an excess of CO in $O_2$) to create an amplified level of $NO_2$, which can be measured in a flowing system, by various techniques [50]. The concentrations of $RO_2$/ $HO_2$ are then

calculated by determining the number of $NO_2$ molecules produced per peroxy radical – the chain length. The reaction scheme is as follows:

$R'CHO_2 + NO \rightarrow NO_2 + R'CHO$ **Equation 1.3**

$R'CHO + O_2 \rightarrow HO_2 + R'CO$ **Equation 1.4**

Following on from the formation of $HO_2$ (in addition to that already under investigation from the initial sample), a chain reaction is set up which converts NO to $NO_2$ through the following reaction scheme:

$HO_2 + NO \rightarrow NO_2 + OH$ **Equation 1.5**

$OH + CO \rightarrow CO_2 + H$ **Equation 1.6**

$H + O_2 + M \rightarrow HO_2 + M$ **Equation 1.7**

In summary,

$R'CHO_2 + 2NO + CO + 2O_2 \rightarrow 2NO_2 + R'CO + HO_2 + CO_2$ **Equation 1.8**

These amplified levels of $NO_2$ can subsequently be measured by sensitive detection techniques, such as a chemiluminescence reaction with luminol [45] (detection sensitivity of 0.2 to 2 pptv over a 30 minute acquisition time), LIF (detection sensitivity of around 3 pptv) [51] or in more recent examples, detection by cavity ring down spectroscopy (with a reported detection sensitivity of 0.1 ppbv in 50 s at atmospheric pressure) [52].

To measure accurately the concentrations of $RO_2/HO_2$ in the PERCA method, the number of $NO_2$ molecules produced per peroxy radical, which is called the amplification factor or chain length (*CL*) is required. This can be defined as:

$$CL = \frac{\Delta[NO_2]}{[HO_2]+[RO_2]}$$ **Equation 1.9**

where $\Delta[NO_2]$ is the amount of $NO_2$ produced from the difference between the average of ~20 s of amplification mode data and ~20 s of termination mode data (amplification and termination mode refer to whether the reactions are occurring at the inlet or outlet of the monitoring equipment [45]). The chain length depends on the intermediate reactions. In order to obtain accurate concentrations, the number of $NO_2$ molecules produced per peroxy radical must be accurately known (shown in Equation 1.8). This is determined by a variety of factors including concentrations of species present, flow rates, removal rates and processes and other losses. Twice daily calibration measurements are required with known $NO_2$/air mixtures. A further drawback of the technique is that it is not speciated – it does not discriminate between concentrations of $RO_2$ and $HO_2$.

### 1.4.1.3. The NICE-OHMS Technique

In this thesis, a NICE-OHMS spectrometer is characterised which could provide a feasible alternative to the $HO_2$ detection problems currently faced. The technique enables the fast, accurate and direct detection of $HO_2$ and here its potential is shown by measurements of $HO_2$ in a laboratory environment.

## References


[1] D.E. Heard, *Annual Review of Physical Chemistry*, **57**, 191-216 (2006)
[2] J. Ye, L.S. Ma, J.L. Hall, *Journal of the Optical Society of America B - Optical Physics*, **15(1)**, 6-15 (1998)
[3] T. Röckmann, J. Kaiser, C.A.M. Brenninkmeijer, W.A. Brand, *Rapid Communications in Mass Spectrometry*, **17**, 1897-1908 (2003)
[4] A.L. Rice, P.D. Quay, *Analytical Chemistry*, **78**, 6320-6326 (2006)
[5] M.W. Sigrist, R. Bartlome, D. Marinov, J.M. Rey, D.E. Vogler, H. Wächter, *Applied Physics B - Lasers and Optics*, **90**, 289-300 (2008)
[6] R.F. Curl, F. Capasso, C. Gmachl, A.A. Kosterev, B. McManus, R. Lewicki, M. Pusharsky, G. Wysocki, F.K. Tittel, *Chemical Physics Letters*, **487**, 1-18 (2010)
[7] D. Herriott, H. Kogelnik, R. Kompfner, *Applied Optics*, **3**, 523-526 (1964)
[8] J.U. White, *Journal of the Optical Society of America*, **32**, 285-288 (1942)
[9] D.C. Hovde, J.T. Hodges, G.E. Scace, J.A. Silver, *Applied Optics*. **40**, 829-839 (2001)
[10] E. Kritchman, S. Shtrikman, M. Slatkine, *Journal of the Optical Society of America*, **68**, 1257-1271 (1978)
[11] F.J.M. Harren, F.G.C. Bijnen, J. Reuss, L.A.C.J. Voesenek, C.W.P.M. Blom, *Applied Physics B - Lasers and Optics*, **50**, 137-144 (1990)
[12] L.J. Kramer, R.J. Leigh, J.J. Remedios, P.S. Monks, *Journal of Geophysical Research*, **113**, D16S39 (2008)
[13] A.J.S. McGonigle, C.L. Thomson, V.I. Tsanev, C. Oppenheimer, *Atmospheric Environment*, **38**, 21-25 (2004)
[14] J.M. Langridge, S.M. Ball, R.L. Jones, *Analyst*, **131**, 916-922 (2006)
[15] J.M. Langridge, S.M. Ball, A.J.L. Shillings, R. L. Jones, *Review of Scientific Instruments*, **79**, 123110 (2008)
[16] G. McFiggans, C.S.E. Bale, S.M. Ball, J. M. Beames, W.J. Bloss, L.J. Carpenter, J. Dorsey, R. Dunk, M.J. Flynn, K.L. Furneaux, M.W. Gallagher, D.E. Heard, A.M. Hollingsworth, K. Hornsby, T. Ingham, C.E. Jones, R.L. Jones, L.J. Kramer, J.M. Langridge, C. Leblanc, J.-P. LeCrane, J.D. Lee, R.J. Leigh, I. Longley, A.S. Mahajan, P.S. Monks, H. Oetjen, A.J. Orr-Ewing, J.M.C. Plane, P. Potin, A.J.L. Shillings, F. Thomas, R. von Glasow, R. Wada, L.K. Whalley, J.D. Whitehead, *Atmospheric Chemistry and Physics*, **10**, 2975–2999, (2010)
[17] M.D. King, E.M. Dick, W.R. Simpson, *Atmospheric Environment*, **34**, 683-686 (2000)
[18] R. Wada, J.M. Beames, A.J. Orr-Ewing, *Journal of Atmospheric Chemistry*, **58**, 69-87, (2007)
[19] P.S. Monks, *Chemical Society Reviews*, **34**, 376-396 (2005)
[20] S.E. Fiedler, A. Hese, A.A. Ruth, *Chemical Physics Letters*, **371**, 284-294 (2003)
[21] S.M. Ball, A.M. Hollingsworth, J. Humbles, C. Leblanc, P. Potin, G. McFiggans, *Atmospheric Chemistry and Physics*, **10**, 6237-6254 (2010)
[22] D. Davis, J. Crawford, S. Liu, S. McKeen, A. Bandy, D. Thornton, F. Rowland, D. Blake, *Journal of Geophysical Research*, **101**, 2135-2147 (1996)
[23] W.J. Bloss, S.M. Ball, *Bulletin of the Environmental Chemistry Group, Royal Society of Chemistry* (http://www.rsc.org/images/ECGBulletinJuly2009_tcm18-157764.pdf), 2040-1469, (2009)
[24] A.S. Mahajan, H. Oetjen, A. Saiz-Lopez, J.D. Lee, G.B. McFiggans, J.M.C. Plane, *Geophysical Research Letters*, **36**, L16803 (2009)
[25] T. Gherman, D.S. Venables, S. Vaughan, J. Orphal A.A. Ruth *Environmental Science and Technology*, **42**, 890-895 (2008)

[26] A. O'Keefe, D.A.G.Deacon, *Review of Scientific Instruments*, **59**, 2544-2551 (1988)
[27] T. Blakie, Part II Thesis, University of Oxford (2010)
[28] G. Berden, R. Peeters, G. Meijer, *International Reviews in Physical Chemistry*, **19**, 565-607 (2000)
[29] G. Berden, R . Engeln (eds), *Cavity Ring Down Spectroscopy: Techniques and Applications* , Wiley (2009)
[30] B.J Allan, N. Carslaw, H. Coe, R.A. Burgess, J.M.C. Plane, *Journal of Atmospheric Chemistry*, **33**, 129-154 (1999)
[31] D.J. Fish, D.E. Shallcross, R.L. Jones, *Atmospheric Environment*, **33**, 687-691 (1999)
[32] H. Stark, S.S. Brown, P.D. Goldan, M. Aldener, W.C. Kuster, R. Jakoubek, F.C. Fehsenfeld, J. Meagher, T.S. Bates, A.R. Ravishankara, *Journal of Geophysical Research*, **112**, D10S10 (2007)
[33] R.E.H. Miles, S. Rudic, A.J. Orr-Ewing, J.P. Reid, *Journal of Physical Chemistry A*, **114**, 7077-7084 (2010)
[34] R.M. Varma, D.S. Venables, A.A. Ruth, U. Heitmann, E. Schlosser, S. Dixneuf, *Applied Optics*, **48**, B159-B171 (2009)
[35] S.C. Smith, J.D. Lee, W.J. Bloss, G.P. Johnson, T. Ingham, D.E. Heard, *Atmospheric Chemistry and Physics*, **6**, 1435-1453 (2006)
[36] D.E. Heard, M.J. Pilling, *Chemical Reviews*, **103**, 5163-5198 (2003)
[37] K.C. Clemitshaw, *Critical Reviews in Environmental Science and Technology*, **34**, 1-108 (2004)
[38] D.E. Heard, *Encyclopedia of Atmospheric Sciences*, J.R. Holton, J.A. Pyle, J.A. Curry (eds), Amsterdam: Elsevier, 2185–2193 (2003)
[39] P.S. Monks, *Chemical Society Reviews*, **34**, 376-395 (2005)
[40] J. Parra, L.A. George, *Applied Optics*, **48**, 3355-3361 (2009)
[41] S. Dusanter, D. Vimal, P.S. Stevens, R. Volkamer, L.T. Molina, *Atmospheric Chemistry and Physics*, **9**, 1665-1685 (2009)
[42] L.K. Whalley, K.L. Furneaux, A. Goddard, J.D. Lee, A. Mahajan, H. Oetjen, K.A. Read, N. Kaaden, L.J. Carpenter, A.C. Lewis, J.M.C. Plane, E.S. Saltzman, A. Wiedensohler, D.E. Heard, *Atmospheric Chemistry and Physics*, **10**, 1555-1576, (2010)
[43] C.A. Cantrell, D.H. Stedman, G.J. Wendel, *Analytical Chemistry*, **56**, 1496-1502 (1984)
[44] R.C. Cohen, E.C. Wood, *Analytical Techniques for Atmospheric Measurement*, ed. D.E. Heard, Oxford: Blackwells (2006)
[45] K.C. Clemitshaw, L.J. Carpenter, S.A. Penkett and M.E. Jenkin, *Journal of Geophysical Research*, **102**, 25,405-25,416 (1997)
[46] T.J. Green, C.E. Reeves, N. Brough, G.D. Edwards, P.S, Monks, S.A. Penkett, *Journal of Environmental Monitoring*, **5**, 75-83 (2003)
[47] Y. Liu, R. Morales-Cueto, J. Hargrove, D. Medina, J. Zhang, *Environmental Science and Technology*, **43**, 7791-7796 (2009)
[48] J.D. Lee, G. McFiggans, J.D. Allan, A.R. Baker, S.M. Ball, A.K. Benton, L.J. Carpenter, R. Commane, B.D. Finley, M. Evans, E. Fuentes, K. Furneaux, A. Goddard, N. Good, J.F. Hamilton, D.E. Heard, H. Herrmann, A. Hollingsworth, J. R. Hopkins, T. Ingham, M. Irwin, C.E. Jones, R.L. Jones, W.C. Keene, M.J. Lawler, S. Lehmann, A.C. Lewis, M.S. Long, A. Mahajan, J. Methven, S. J. Moller, K. Müller, T. Müller, N. Niedermeier, S. O'Doherty, H. Oetjen, J. M. C. Plane, A.A.P. Pszenny, K. A. Read, A. Saiz-Lopez, E.S. Saltzman, R. Sander, R. von Glasow, L. Whalley, A. Wiedensohler, D. Young , *Atmospheric Chemistry and Physics*, **10**, 1031-1055 ( 2010)

[49] Y. Kanaya, Y. Sadanaga, J. Hirokawa, Y. Kajii, H. Akimoto, *Journal of Atmospheric Chemistry*, **38**, 73-110 (2001)
[50] J. Burkert, M.-D. Andrés-Hernández, D. Stöbener, J.P. Burrows, M. Weissenmayer, A. Kraus, *Journal of Geophysical Research*, **106**, 5457-5477 (2001)
[51] Y. Sadanaga, J. Matsumoto, K. Sakurai, R. Isozaki, S. Kato, T. Nomaguchi, H. Bandow, Y. Kajii, *Review of Scientific Instruments*, **75**, 864-872 (2004)
[52] R. Wada, A.J. Orr-Ewing, *Analyst*, **130**, 1595 - 1600 (2005)

# 2. Chapter 2

# Spectroscopic Measurements of Ammonia using CEAS

As described previously in chapter 1, one of the primary aims of this thesis is to develop spectroscopic measurements for $HO_2$. As will be described in Chapter 5, the most appropriate band for detection is centred around 1504 nm, therefore the work in this thesis utilises an external cavity diode laser operating between 1480 – 1540 nm. Ammonia is another atmospherically important species, with transitions in the ($\upsilon_1$ + $\upsilon_3$) combination band lying within this wavelength range, convenient for its detection. In this chapter, cavity enhanced absorption spectroscopy (CEAS), a key component of the NICE-OHMS

setup, is performed on a low pressure sample of ammonia around 1516 nm. The experimental setup is detailed, followed by a demonstration of a CEAS sensitivity of $6 \times 10^{-8}$ $cm^{-1}$ $Hz^{-1/2}$ within a cavity whose finesse is 1150. The technique is then utilised to measure pressure induced broadening and shift coefficients with six gases (helium, neon, argon, xenon, oxygen and nitrogen) at room temperature for four transitions of ammonia. Comparisons of the broadening coefficients with previous work in this region, where it existed, showed good agreement. Following this, an application of the Parmenter-Seaver formalism to estimate the potential well depth of the ammonia dimer from the measured broadening coefficients is presented, with the obtained well depth agreeing well with theoretical calculations.

## 2.1. Importance of Ammonia Detection

Atmospheric ammonia is increasingly being recognised as a key environmental pollutant [1]. Ammonia as a trace gas in the atmosphere contributes to several environmental problems such as: direct toxic effects on vegetation, atmospheric nitrogen deposition leading to the eutrophication and acidification of sensitive ecosystems, and to the formation of secondary particulate matter in the atmosphere with effects on human health, atmospheric visibility and global radiative balance [2]. Produced from activities including livestock

breeding and the use of nitrogen fertilizers, emissions of ammonia are increasing rapidly in many parts of the world, and so without intervention, the environmental concerns outlined will be expected to grow in future. Across Europe, air quality targets and associated efforts are currently being made to reduce ammonia emissions, alongside reductions in other air pollutants, notably sulphur dioxide and nitrogen oxides. However, reducing ammonia emissions has proved to be challenging, with only modest regional reductions achieved to date. As the emissions of sulphur dioxide and nitrogen oxides are reduced, ammonia will increasingly dominate the air pollution climate of Europe. The consequent environmental impacts highlight the importance for its atmospheric detection.

As an introduction to the sensitive detection techniques forming the basis of investigation in this thesis, an application of laser spectroscopy is used to determine the pressure broadening and shift coefficients for transitions in the ($\upsilon_1$ + $\upsilon_3$) combination band of ammonia using basic cavity enhanced absorption spectroscopy (CEAS). For accurate monitoring, specific knowledge of the impact of broadening and shifting effects on line shape parameters is essential [3, 4, 5, 6, 7]. Following on from this, a more theoretical discussion is presented in order to demonstrate that for rare gases, the obtained pressure broadening co-

efficients can be used to estimate the intermolecular well depth of the ammonia dimer.

## 2.2. Cavity Enhanced Absorption Spectroscopy (CEAS)

A large number of industrial applications and environmental monitoring techniques require accurate, fast and species specific detection of trace gases. With the development of diode lasers for the telecommunications industry, laser spectroscopic techniques in the near infrared have become popular for trace gas detection due to their ease of use and the low costs involved [8, 9, 10, 11]. CEAS, with its low cost and robust, flexible and simple experimental setup can meet the requirements of speciated gas phase detection. CEAS involves measuring the transmission of light through an optical cavity, consisting of two highly reflective mirrors between which the light is reflected multiple times, thereby greatly increasing the effective path length [8, 9]. The basic CEAS experimental setup is shown schematically in Figure 2.1.

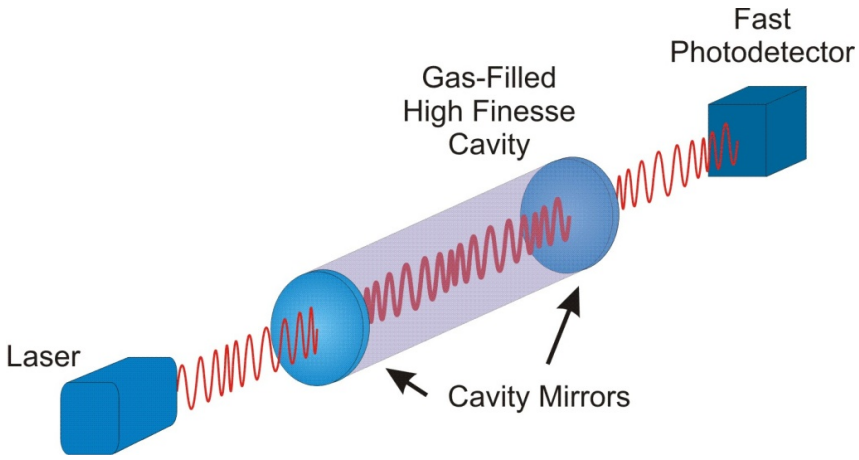


**Figure 2.1 Basic setup for a CEAS experiment – light is passed into the high finesse cavity, with the change in intensity being recorded on a photodetector as the laser is scanned.**

The change in time integrated intensity of the transmitted light can be related to the concentration of the absorbing species present through a modification of the Beer-Lambert law [8]. This will be described in Section 2.2.2 following a discussion of cavity modes.

### 2.2.1. Cavity Modes

In general, when the distance travelled by the light in one round trip of the cavity equals an integer multiple of the wavelength, $n\lambda$, constructive interference (resonance) occurs, allowing light intensity to build up within the cavity and correspondingly enhancing the transmission. These resonant frequencies are termed cavity modes. The light exiting the cavity when the resonant condition is satisfied (and the cavity modes are excited), can be observed by placing an IR camera at the exit cavity mirror, as shown in Figure 2.2.

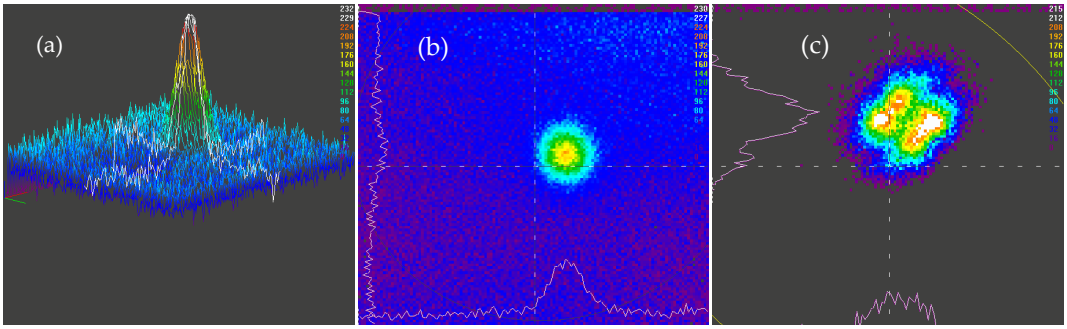


**Figure 2.2 Cavity modes observed using a near IR camera, showing the $TEM_{00}$ mode (a and b), and the higher order $TEM_{11}$ mode (c).**

The modes of an optical cavity are properly described as solutions to the three dimensional wave equation. In full, the frequencies of the modes of a two-mirror optical cavity of length $L$, with mirror g-parameters $g_1$ and $g_2$, where $g_n = 1\text{-}L/r_n$, can be expressed as [12]:

$$\nu_{m,n,q} = \frac{c}{2L}\left[q + \frac{n+m+1}{\pi}\arccos\sqrt{g_1 g_2}\right] \qquad \textbf{Equation 2.1}$$

where $q$ is the longitudinal mode index, and $m$ and $n$ specify the number of optical nodes in the two directions perpendicular to the propagation axis with $r$ being the radius of curvature of the mirror. Two modes with the same values of $m$ and $n$, but consecutive $q$ values (longitudinal modes), define the free spectral range of the cavity by their difference in frequency, i.e. $\Delta\upsilon_{FSR} = c/2L$. Modes of the same $q$, but differing in their values of $m$ and/or $n$, are termed the transverse modes of the cavity, and are generally denoted $TEM_{mn}$ modes.

The $TEM_{00}$ mode, where $m = n = 0$, is the highest-intensity mode of a simple two-mirror optical cavity. Shown in Figure 2.2 (a) and (b), it describes a Gaussian beam. Higher order transverse modes, $TEM_{mn}$ modes, where the stable cavity mode is non-Gaussian, also exist and have slightly different resonance frequencies, as shown in Figure 2.2 (c), where the cavity has been aligned such that the $TEM_{11}$ mode is dominant.

If the laser is allowed to remain at a fixed frequency matching the mode frequency, these individual modes will be excited to resonance but then quickly fall out of resonance due to mechanical perturbations; the transmission of the cavity will show strong cavity mode-structure that is transient. In CEAS, the mirrors are misaligned to excite as many of the cavity modes as possible, giving a congested mode structure as a function of frequency. By rapidly scanning the laser frequency back and forth in the region of interest, resonance with any single mode is suppressed to give a smooth average transmission so that absorptions occurring within the cavity can be easily identified [10, 11]. This simple technique utilises the path length enhancement of the optical cavity without the need for complicated locking as is used in locked CEAS experiments presented later in this thesis [13, 14].

The cavity's ability to support constructive interference over the extent of the enhanced path length of the cavity can be described by the finesse of an optical cavity *F*, whereby:

$$F = \frac{\pi\sqrt{R}}{1-R} \qquad \textbf{Equation 2.2}$$

where *R* is the geometric mean of the mirror reflectivities. The cavity finesse can also be defined as the ratio of the cavity free spectral range to the mode width of the cavity resonances.

## 2.2.2. Theoretical Description of CEAS

The Beer-Lambert law provides the basis of the theory for CEAS to obtain concentrations of absorbing species. It relates the transmitted ($I$) and incident ($I_0$) light to the concentration ($C$), interaction length ($L$) with the sample and the wavelength dependent strength of the absorption of the medium (the absorption cross section, $\sigma(\lambda)$):

$$I = I_o \exp\{-\sigma(\lambda)CL\}. \qquad \textbf{Equation 2.3}$$

For small absorptions where $\sigma(\lambda)CL \ll 1$,

$$I = I_o(1-\sigma(\lambda)CL) \qquad \textbf{Equation 2.4}$$

giving

$$\frac{I - I_o}{I_o} = \alpha(\lambda)L \qquad \textbf{Equation 2.5}$$

where $\alpha(\lambda) = \sigma(\lambda)C$, the absorption coefficient of the sample at wavelength $\lambda$.

For CEAS, the transmission through the cavity can be represented by the modified Beer-Lambert law

$$\frac{(I_o - I)}{I} = \frac{\alpha(\upsilon)L}{(1 - R)} \qquad \textbf{Equation 2.6}$$

where $I$ and $I_0$ are the transmitted intensities with and without an absorbing species present respectively, $\alpha(\upsilon)$ is the frequency dependent absorption coefficient (the product of the absorption cross section, $\sigma$, and the absorber number density, $N$), and $L$ is the cavity length [15]. It is noted that the CEAS signal does not result in an absolute measurement; it is necessary to calibrate the setup for a well defined transition at a known volume of gas, to determine the mirror reflectivity $R$. The total concentration of the absorbing species $C$ is commonly determined by integrating the area under the recorded absorption feature using:

$$\int \frac{(I_o(\upsilon) - I(\upsilon))}{I(\upsilon)} d\upsilon = \frac{CSL}{(1 - R)} \qquad \textbf{Equation 2.7}$$

where $S$ is the integrated absorption cross section, $cm^2\ cm^{-1}$, as used in for instance the HITRAN database. It should be noted that the integrated absorption

cross section defined in this way is temperature dependent, via the Boltzmann relation between the total concentration $C$ and the concentration, $C_{v,J}$, of the level for which the absorption is measured.

The typical path lengths achieved for CEAS are in the order of kilometres. For example, for a high finesse cavity of 10500, a path length of the order of 6 km can be obtained using a bench top setup with a resonant optical cavity of length around 1 m formed from mirrors with reflectivity $R$ of 0.9997. This is in contrast with a simple multipass cell, where the equivalent 1 m cell used for infrared absorption measurements gives an effective path length between 3 and 150 m [16].

The derivation of Equation 2.6 has been described in the review of Mazurenka *et al* [12], where the output intensity was related to the incident light, considering mirror reflections (each giving rise to a term in $1-R$) and single-pass absorptions ($1-A$) for an infinite number of passes within the cavity:

$$I_{trans} = I_{in}(1-R)^2(1-A)\sum_{n=0}^{\infty} R^{2n}(1-A)^{2n} \qquad \textbf{Equation 2.8}$$

For $R < 1$ and $A < 1$, this can be rewritten as the sum of a geometric progression:

$$I_{trans} = I_{in}\frac{(1-R)^2(1-A)}{1-R^2(1-A)^2} \qquad \textbf{Equation 2.9}$$

The ratio of intensities measured both with and without an absorber present, $I/I_0$ can be calculated, and with substitution of the one-pass fractional intensity change caused by absorption, $(1\text{-}A) = e^{-\alpha L}$ is:

$$\frac{I_0}{I} = \frac{1 - R^2 \exp\{-2\alpha L\}}{(1 - R^2)\exp\{-\alpha L\}} \qquad \textbf{Equation 2.10}$$

In the limit where $R$ is approaching 1 and $\alpha$ is approaching 0, this results in Equation 2.6.

### 2.2.3. Signal, Noise and Sensitivity

As in all detection techniques, the maximum sensitivity that can be attained is governed by an optimal relationship between signal and noise. It is generally desirable to measure a large change in signal upon a relatively noise free background, however, particularly in absorption methods such as CEAS, limitations are imposed due to the requirement of being able to discriminate very small changes in light intensity against a background of high intensity transmitted light [12].

Laser absorption spectroscopy fundamentally relies on the change in intensity of light recorded on a detector as the light is passed through an absorbing medium. The maximum detection sensitivity that can be attained is referred to as the shot-noise limit and occurs when the laser has no additional amplitude

modulations other than its statistical/intensity fluctuations. The minimum detectable absorption signal, at the shot-noise limit is defined by:

$$(\alpha L)_{\min} = \left( \frac{2eB}{\eta P_0} \right)^{1/2}$$ **Equation 2.11**

where $e$ is the electron charge (C), $B$ is the detection bandwidth (Hz), $\eta$ is the responsivity of the photodetector (in A/W) and $P_0$ is the incident power (W) [17]. In the ideal case, where 1 mW of radiation travelling over a path length of 1 m, is incident on the detector with a (typical) responsivity of 1 A/W, and a bandwidth of 400 Hz, the system is limited to a maximum absorption sensitivity of ~4 x $10^{-7}$ $cm^{-1}$. However, in practice, it is unlikely that this limit will be reached, due to interfering noise from various sources such as variations in the laser intensity, 1/f noise, detector noise and external instability influences. In order to try to attain the more demanding detection sensitivities required for practical applications in sensitive trace gas detection, improvements must be made by increasing the optical pathlength whilst also reducing the noise inherent in the measurement; both of these improvements are implemented in the NICE-OHMS technique.

Sensitivity is used as a metric for comparing different spectroscopic techniques in order to assess their effectiveness, and so it is necessary to clearly de-

fine what is meant by the term. In absorption spectroscopy, sensitivity is generally defined as the minimum detectable absorption coefficient, $\alpha_{\min}$ (in $cm^{-1}$), associated with a S/N = 1. Including the option for varying the interaction length term, the minimum detectable absorbance, ($\alpha L_{\min}$) in the case of CEAS, is equivalent in amplitude to the shot-noise limit for a cavity with finesse *F*:

$$(\alpha L)_{\min} = \frac{\pi}{F}\left(\frac{2eB}{\eta P_0}\right)^{1/2} \qquad \textbf{Equation 2.12}$$

If the sensitivity of a given technique could be improved by averaging, then it is generally given that the sensitivity is reported in terms of either a defined bandwidth ($cm^{-1}$), or a bandwidth reduced sensitivity ($cm^{-1}\ Hz^{-1/2}$). This enables a fair comparison across different absorption techniques to assess their respective performance. In CEAS, the average transmission of a CEAS cavity is very small (< 100 μW generally reaches the detector), resulting typically in sensitivities of around ~ $10^{-8}$ – $10^{-9}$ $cm^{-1}$. Improvements in the light levels and therefore the signal to noise ratio are required for more sensitive gas phase measurements to be undertaken.

## 2.3. Experimental details

The experimental setup used for the acquisition of the data presented in this chapter is shown schematically in Figure 2.3. A tunable external cavity diode

laser (Sacher Lasertechnik, quoted bandwidth < 2 MHz) operating around 1516 nm provided the light source.

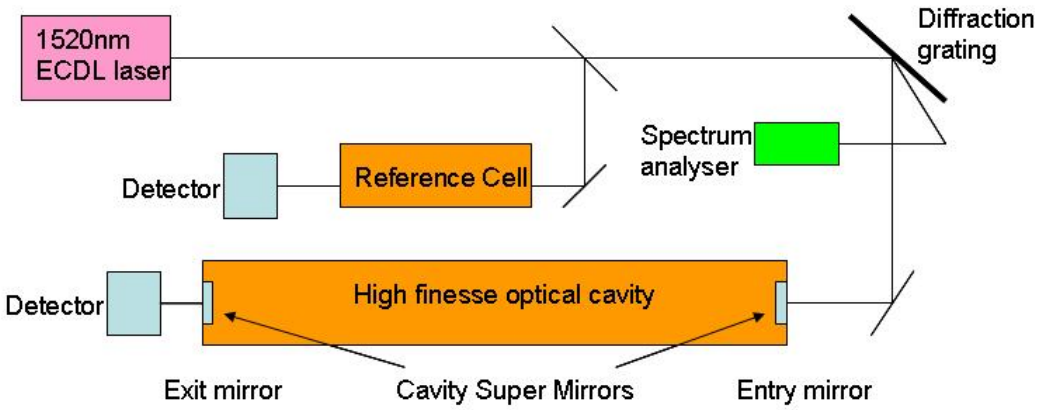


**Figure 2.3 Experimental setup for the CEAS measurements.**

The laser was operated around 34 °C with a current of approximately 100 mA which gave an output power of 1.8 mW. The frequency of the laser diode was ramped via the PZT of the external cavity, with a triangular wave at 5.1 Hz to scan the frequency over approximately 0.6 $cm^{-1}$. The wavelength of the laser was monitored with a wavemeter (Burleigh WA-1000) and a frequency scale for the scan was generated by monitoring the laser output with a spectrum analyser (10 GHz Melles Griot 1300-1500 nm, aligned for a free spectral range of 0.752 GHz).

The laser radiation was directed onto a diffraction grating (Thorlabs GR-13-0646) and then passed through a pinhole to remove the amplified spontaneous emission (ASE) from the laser output. The radiation was then coupled into the

cavity formed by two high reflectivity mirrors (Newport 10CV00SR.70T), which were separated by a distance of 0.67 m. The light transmitted through the cavity was detected on a photodiode (Thorlabs DET410) and the amplified signal then recorded with a digital oscilloscope (LeCroy 9304) and passed to a computer. A chopper motor, operated at 400 Hz, was placed on top of the cavity housing in order to disrupt the mode structure further and thereby provide a smoother baseline.

In order to perform pressure shift measurements, an accurate frequency reference is needed with which to concurrently compare the data acquired. A beam sampler (Thorlabs BSP10-C1) was used to direct 10% of the light through a glass reference cell containing a pressure of 12.1 Torr of ammonia, and the transmitted intensity was recorded on a photodetector (New Focus 1611). This cell was held at a constant pressure with the respective ammonia absorption spectra recorded simultaneously with the data from the cavity to provide an absolute frequency reference from which the line shift could be measured.

The optical cavity was enclosed within a glass and steel vacuum assembly with separate inlets for the ammonia and broadening gases. The pressure in the system was recorded with two gauges (Edwards Pirani gauge PRM-10 and

Edwards Active Strain Gauge). Ammonia was introduced to the evacuated cavity at a pressure of 150 mTorr in order to passivate the cavity. During this time, the pressure in the cavity decreased as ammonia was adsorbed on to the cavity walls. Once the ammonia pressure in the cell had stabilised, the broadening gas was added to obtain a total pressure of 700 Torr and the mixture was allowed to equilibrate over 5 minutes. The initial pressure of ammonia was chosen to provide a sensible cavity enhanced absorption signal throughout the range of pressures investigated whilst ensuring that the contribution of the self-broadening of ammonia was negligible in comparison with the measured linewidths.

For each measurement, data were recorded simultaneously from the two photodetectors, following the $NH_3$ cell and cavity respectively, along with data from the spectrum analyser, all using the acquisition software on the oscilloscope. The first measurement, at 700 Torr, was recorded after the gas mixture had stabilised. Following this, a portion of the gas mixture in the cavity was removed using the vacuum system attached to the cavity and then the next set of data recorded. This was repeated at pressures from 700 Torr down to 5 Torr with all experiments carried out at room temperature (295 ± 2 K). The procedure was repeated for the six broadening gases (helium, neon, argon, xenon, oxygen and nitrogen) for the four ammonia transitions under investi-

gation. A measurement was taken of the evacuated cavity with no absorbing species present in order to have a background signal for data processing.

### 2.3.1. Calibration and sensitivity measurement

To determine the frequency dependent mirror reflectivities, and thus the finesse of the cavity, absorption measurements of well known transitions of $N_2O$, at a known pressure, were made. This also enabled the calculation of the sensitivity of the setup. As ammonia may adsorb onto the mirror surfaces and affect the reflectivity, a finesse measurement using $N_2O$ was taken both before and after the broadening and shift measurements had been carried out. As no degradation of the mirror reflectivities was observed by monitoring the signal level and seeing no change over time after the initial introduction of ammonia to the cavity, a single finesse measurement is sufficient to describe the measurement conditions. A known pressure of $N_2O$ (19.5 Torr) was added to the cavity and the absorption spectrum recorded, shown in Figure 2.4; the inset shows the fit to the recorded spectrum for the R51e transition of the $3\nu_3$ band at 6595.74 $cm^{-1}$ used for the finesse calculation which has an integrated absorption coefficient $S$ of 5 x $10^{-25}$ $cm^{-1}$ $cm^2$ [18]. The spectral features on either side of the transition in question were significantly stronger leading to distorted line profiles and so could not be used for the finesse calculation.

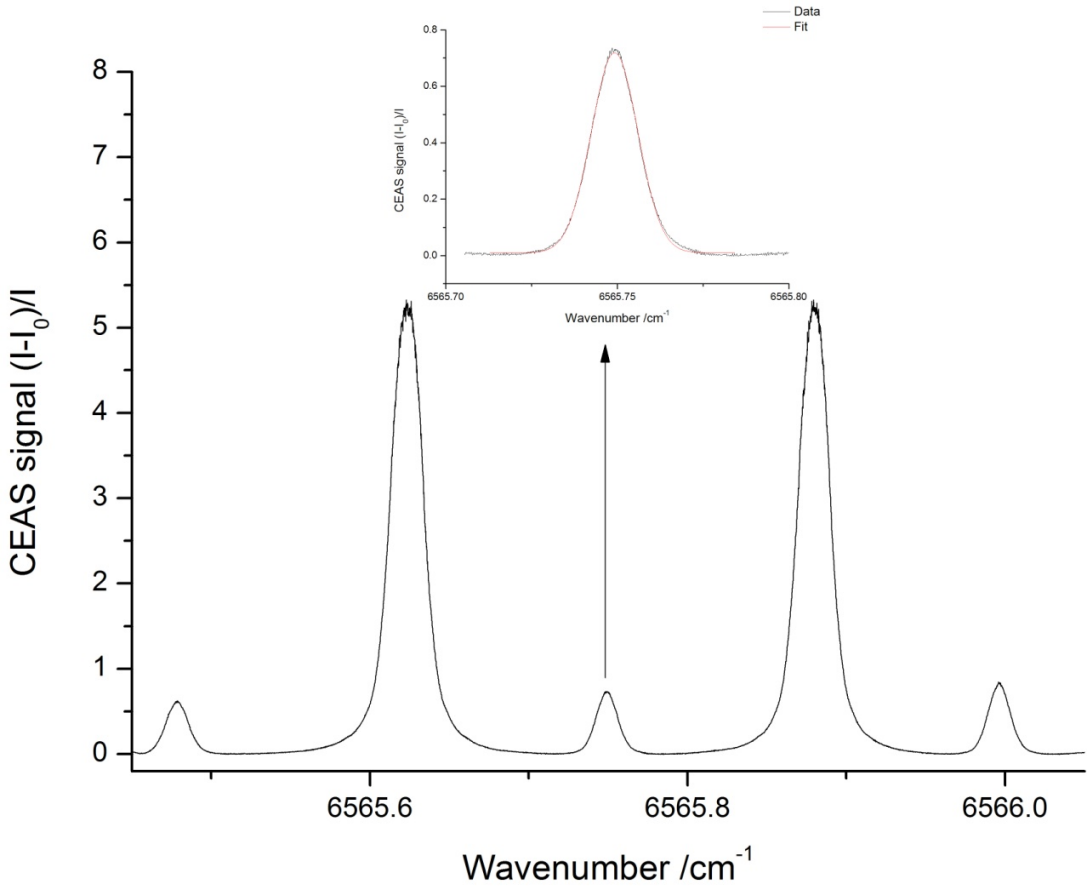


**Figure 2.4 Recorded absorption spectrum of 19.5 Torr of $N_2O$. Shown in the inset is a fit to the recorded $N_2O$ spectrum for the R51e transition of the $3\nu_3$ band at 6595.74 $cm^{-1}$ used for the calibration.**

From the CEAS signal amplitude returned from the Gaussian fit shown in the inset in Figure 2.4 and using Equation 2.6 a mean mirror reflectivity of 0.997 ± 0.01 was calculated, which corresponds to a finesse of 1150.

## 2.3.2. Region of Interest

The four ammonia transitions investigated in this work arising from transitions in the ($\upsilon_1 + \upsilon_3$) combination band are in the region from 6595 to 6596 $cm^{-1}$

as shown in Figure 2.5, with the upper two traces, each including two transitions of interest, being CEAS data acquired with the setup as described and the lower trace showing a simulation using the data from reference [21]. These transitions are relatively strong, well separated, and free from interference by other absorbers [19] making them ideal for use in detection systems [20].

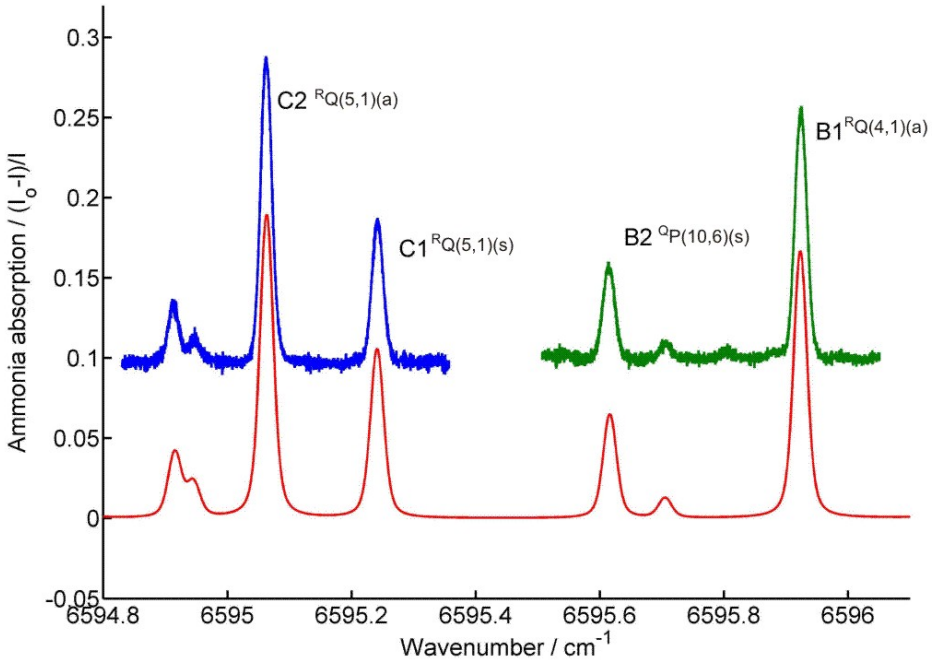


**Figure 2.5 The ammonia absorption spectrum around 6595 cm$^{-1}$. The lower spectrum is a simulated spectrum based on the data in reference [21] with the upper two spectra showing data in the two regions of study (B and C) recorded using the cavity filled with 150 mTorr of ammonia. The absorption feature at 6595.8 seems to be an unreported $NH_3$ transition. The data have been offset (in the y-axis) for clarity.**

This region has previously been studied by Gibb *et al* [19] with the earlier work involving measuring nitrogen, oxygen, air and self-broadening coefficients for six ammonia transitions in the ($\upsilon_1 + \upsilon_3$) combination band of ammo-

nia within the region 6595 to 6600 $cm^{-1}$ using Wavelength Modulation Spectroscopy (WMS). The transitions measured here were described by Gibb *et al*. as regions B and C, with two transitions in each region in the publication. The work presented by Gibb *et al* [19] also included transitions A1 and A2 at 6600.182 and 6599.893 $cm^{-1}$, respectively. However, these transitions are unassigned, and due to their position in the spectrum, careful realignment of the system would have been necessary to extend the work to include them, hence only the B and C lines have been considered here. This naming convention is continued here to refer to the four transitions studied in this chapter, with their labelled positions being indicated on Figure 2.5 and Table 2.1 respectively.

**Table 2.1 Details of the ammonia transitions studied with their wavenumbers and assignments (for notation see main text).**

| Line | Wavenumber / $cm^{-1}$ | Assignments [ref 21] |
|---|---|---|
| **B1** | 6595.923 | $^{R}Q(4,1)$ (a) |
| **B2** | 6595.616 | $^{Q}P(10,6)$ (s) |
| **C1** | 6595.241 | $^{R}Q(5,1)$ (s) |
| **C2** | 6595.063 | $^{R}Q(5,1)$ (a) |

The transitions have been assigned by Lundsberg-Nielsen *et al*. [21] with their line positions given in Table 2.1. The assignment notation corresponds to $^{\Delta K}\Delta J$ (J'', K'') where (J'', K'') are the lower state quantum numbers of the (J', K') ←

(J'', K'') transition and (s) and (a) relate to the symmetric and asymmetric inversion symmetry of the ground vibrational state. The four transitions studied are well separated, but there are also other weaker absorption features in this region, including some not reported by Lundsberg-Nielsen *et al*., which appear on the spectrum and should be noted. During the fitting routines undertaken, the smaller absorption features were included in order to achieve the most accurate fit.

### 2.3.3. Data analysis

Figure 2.6 shows three typical CEAS spectra for 150 mTorr of $NH_3$ broadened and shifted by three different pressures of Xenon for the B1 transition at 6595.923 $cm^{-1}$. As the pressure of broadening gas is increased from 5 to 250 Torr, the absorption profiles become wider due to the pressure broadening effects. Figure 2.6 also shows the pressure shift effect with the absorption profile centres shifting to lower frequencies at higher pressures. In order to obtain the broadening and shift coefficients for each gas, the data were transformed into the form $(I_0\text{-}I)/I$, where $I_o$ was taken from the empty cavity measurement recorded with each data set.

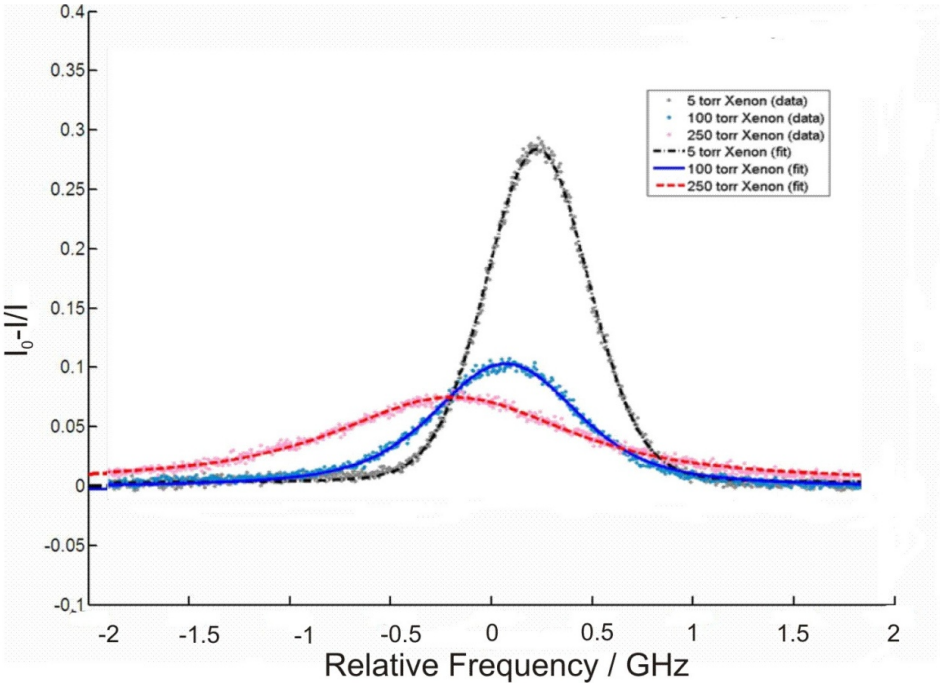


**Figure 2.6 The absorption profile for the B1 line of ammonia at 6595.923 cm$^{-1}$ broadened and shifted by three different pressures of xenon.**

The low pressure absorption traces, shown in Figure 2.5, (~150 mTorr of $NH_3$ before the broadening gases were added) were well represented by a Gaussian profile returning a Gaussian width of 591 ± 5 MHz (FWHM) compared with the theoretical value of 593 MHz. With the broadening gas present, the data were fitted using a Voigt profile (a convolution of a Gaussian profile and a Lorentzian profile) as given in Equation 2.13:

$$f(\upsilon) = A\int_{-\infty}^{\infty} \frac{e^{-x^2}}{\left(\sqrt{\ln 2}\,\frac{\Delta\nu_L}{\Delta\nu_G}\right)^2 + \left[\sqrt{4\ln 2}\,\frac{\nu-\nu_o}{\Delta\nu_G} - x\right]^2} dx \qquad \textbf{Equation 2.13}$$

where $A$ is a scaling factor, $\nu_o$ is the central transition frequency, $\Delta\nu_G$ is the half width at half maximum (HWHM) of the Gaussian component of the fit and $\Delta\nu_L$ is the HWHM of the Lorentzian component of the fit. The fitting routine had $\Delta\nu_G$ fixed to the theoretical value, while $\Delta\nu_L$ , $\nu_o$, and $A$ were allowed to vary. From this fit, the Lorentzian width of each absorption profile and the central frequency were obtained. As demonstrated by the fits shown in Figure 2.6, throughout the fitting procedure the absorption feature was well represented by a Voigt profile and no evidence of collisional narrowing and/or line mixing was observed.

To determine the pressure broadening coefficient, the HWHM of the Lorentzian component from each absorption feature was plotted as a function of pressure. A straight line fit (without forcing the intercept through zero) through these data returns a gradient $\gamma$, the pressure broadening coefficient. Data were recorded at pressures from 5 to 700 Torr, however, in some cases, at higher pressures (above 500 Torr), the pressure broadening can cause merging of the transitions and can compromise the accuracy of the fitting routine for the features, with the features becoming indiscernible as specific transitions.

When calculating the pressure shifts, it was necessary to record the change in the line centre ($\nu_o$) of the absorption feature relative to a constant low pressure

gas sample and measure the difference between the centre frequency of the transition at pressure, $P$, in the cavity and the centre of the same transition in the fixed pressure static cell. This difference was plotted against pressure and a linear fit through these data returned a gradient $\delta$, the pressure shift coefficient.

The errors (corresponding to one standard deviation uncertainty, $1\sigma$, as will be the case throughout this thesis) on the individual measured data points for broadening and shift are those arising from the Voigt fitting procedure along with an estimate of the reproducibility of the results acquired and systematic errors from readings of the pressure gauge. The errors reported for broadening and shift coefficients are from a weighted linear fit of the data. Error bars are shown on the figures, however, in the case of the broadening data, the error bars are small and so cannot be clearly seen.

## 2.4. Results and Discussion

### 2.4.1. Pressure Broadening Measurements

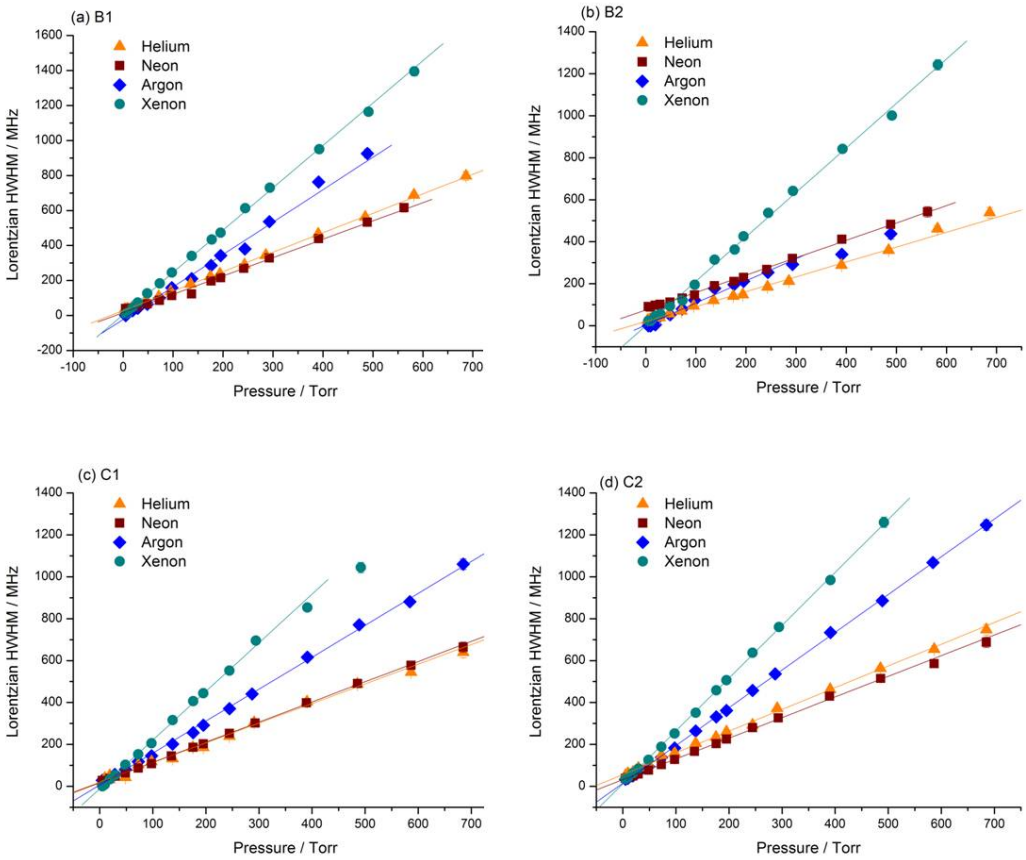


**Figure 2.7 The Lorentzian HWHM as a function of pressure for the (a) B1, (b) B2, (c) C1 and (d) C2 lines of ammonia for broadening by the rare gases-He, Ne, Ar and Xe.**

The recorded Lorentzian HWHM's were plotted as a function of pressure, as shown in Figure 2.7 for each of the four ammonia lines under consideration broadened by four noble gases: Helium, Neon, Argon and Xenon with the gradients through these points returning the pressure broadening coefficients,

shown in Table 2.2. Also shown in the table are the results for previously published work on the same transitions, with which these results show good agreement.

**Table 2.2 Pressure broadening coefficients for the four absorption lines with six collision partners, all referring to HWHM values. Also shown are previously published measurements for the same lines where available [19]. Errors were calculated as explained in the text.**

| | | Pressure broadening coefficients / MHz Torr$^{-1}$ | | | | | | | |
|---|---|---|---|---|---|---|---|---|---|
| **Line** | Frequency / cm$^{-1}$ | γ-He | γ-Ne | γ-Ar | γ-Xe | γ-$O_2$ | γ-$N_2$ | γ-$O_2$ [ref. 19] | γ-$N_2$ [ref.19] |
| **B1 $^{R}$Q(4,1)** | 6595.923 | 1.11±0.02 | 1.05±0.02 | 1.85±0.02 | 2.42±0.02 | 2.10±0.02 | 3.45±0.03 | 1.93±0.10 | 3.63±0.19 |
| **B2 $^{Q}$P(10,6)** | 6595.616 | 0.71±0.02 | 0.83±0.02 | 1.05±0.02 | 2.12±0.03 | 1.44±0.02 | 2.75±0.03 | 1.48±0.10 | 2.74±0.15 |
| **C1 $^{R}$Q(5,1)** | 6595.241 | 0.96±0.02 | 0.94±0.02 | 1.52±0.02 | 2.32±0.03 | 2.19±0.02 | 2.80±0.02 | 1.73±0.08 | 2.97±0.16 |
| **C2 $^{R}$Q(5,1)** | 6595.063 | 1.04±0.02 | 0.99±0.02 | 1.80±0.02 | 2.52±0.02 | 1.81±0.02 | 3.52±0.02 | 1.69±0.09 | 3.39±0.18 |

Pressure broadening effects result from the increasing collisions at higher pressures causing an associated reduction in the average lifetime of both levels involved in the transition [22]. It should be noted, however, that the pressure broadening parameters are not solely dependent on collision rate but are subtly determined by the intermolecular forces which operate during the interaction between the molecule and the radiation field [23]. The broadening coefficients are therefore expected to increase through the rare gases as their polarisability increases. The rare gases have a dipole induced dipole interaction with ammonia and so a larger temporary induced dipole results in a stronger

interaction and associated larger broadening coefficient. This trend of increasing broadening coefficients through the rare gases is observed in the pressure broadening results for all lines and broadening gases, as shown in Table 2.2, and illustrated in Figure 2.7.

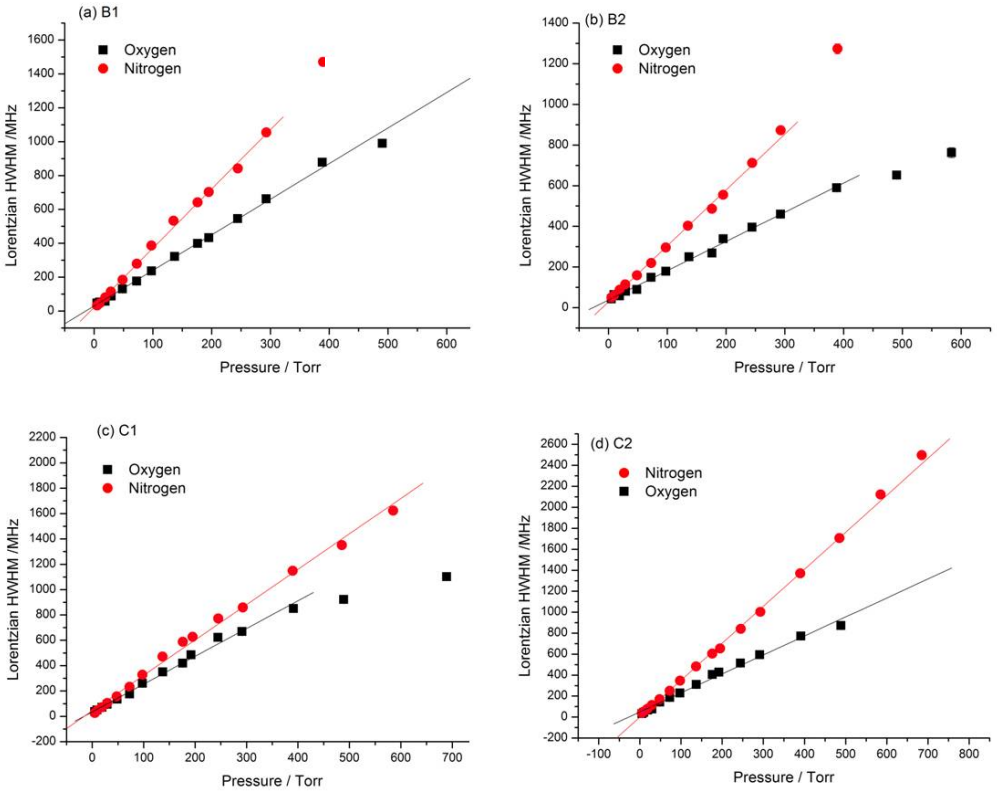


**Figure 2.8 The Lorentzian HWHM as a function of pressure for the (a) B1, (b) B2, (c) C1 and (d) C2 lines of ammonia for broadening by the diatomic gases $O_2$ and $N_2$.**

The broadening coefficients for $N_2$ and $O_2$ measured are shown in Table 2.2 and illustrated again for the four ammonia lines in Figure 2.8. Both oxygen and nitrogen have a quadrupole-dipole interaction with the ammonia, with nitrogen having the larger quadrupole moment and, as such, would be ex-

pected to have the larger broadening coefficient. Recently Koshelev *et al*. [20] have measured pressure broadening coefficients, $\gamma$, for a number of $^{R}P(J'',0)$ transitions in the ($\upsilon_1 + \upsilon_3$) band of $NH_3$ with $N_2$ and $O_2$ as collision partners. They find, as have studies of pressure broadening in other bands [24, 25, 26, 27, 28, 29], that $\gamma$ decreases with increasing J″, by approximately a factor of 2 for $N_2$, and 1.8 for $O_2$ between J″ = 2 and 9. For the $\upsilon_1$ [27, 28] and $\upsilon_4$ [29] bands $\gamma$ increases with increasing K″ for a given J″, with the increase being of the order of 10% over the available K″ space for all measured colliders except for self-broadening, where a more marked variation is observed [27]. As the transition J'' (initial rotational level) → J' (upper rotational level) involves transfer of energy, it can be suggested the decrease in $\gamma$ for a increasing J'' could be accounted for by the increased difficulty of transferring larger amounts of energy as J'' increases. The limited results obtained in this work, shown in Table 2.2 generally confirm this trend ($\gamma$ values are lower for the J″ = 10 line than for J″ = 4, 5 for all colliders), and thus the results in this work for J″ = 4, K″ = 1 can be confidently compared to with those of Koshelev *et al*. for J″ = 4, K″= 0. For $O_2$ and $N_2$, the measured broadening coefficients were $\gamma$ = 2.10 and $\gamma$ = 3.5 MHz $Torr^{-1}$, respectively, which is in excellent agreement with the reported values of 2.08 and 3.60 MHz $Torr^{-1}$ [20]. They are also in good agreement with measurements undertaken at higher frequencies [30].

Koshelev *et al*. [20] have shown that for given values of J" and K", $\gamma$ is largely independent of the vibrational band measured, and this has been previously noted [31]. It follows thus that the results from this work should be able to undergo comparison with previous measurements and calculations in other bands [29, 32, 33], particularly the extensive calculations carried out by Dhib *et al*. on $NH_3$ broadening coefficients [29, 33, 34], on the $\upsilon_4$ band in collisions with He and Ar [29], and $N_2$ and $O_2$ [33]. The calculated values for the $\upsilon_4$ band are in good agreement with the experimental data: for example the averaged values on the $^{R}Q(5,1)$ lines in Table 2.2 (C1 and C2) are 1.00 and 1.66 MHz $Torr^{-1}$, respectively, compared with the calculated values for He and Ar on the $^{P}P(5,1)$ lines of 1.12 and 1.64 MHz $Torr^{-1}$ [29].

The calculations referred to above are based on the semiclassical formalism of Robert and Bonamy (RB) [35] and have also been performed for the transitions presented here by Dr Dhib, (Laboratoire de Physique Moleculaire, Ecole Superieure des Sciences et Techniques de Tunis) in a collaboration for this work and associated publication [36]. In this theory, the relative trajectories of $NH_3$ and perturber are treated classically and are developed up to second order in time. The collisional half-width, $\gamma$, and frequency shift, $\delta$, of an isolated, pressure broadened transition are given by

$$\gamma + i\delta = \frac{n}{2\pi c}\sum_J \rho_J \int_0^\infty u f(u)du \int_{r_{c0}}^\infty 2\pi r_c dr_c \left(\frac{u'_c}{u}\right)^2 S(r_c, u, J), \qquad \textbf{Equation 2.14}$$

where $n$ is the number density of the perturber gas, $f(u)$ is the Maxwellian distribution of relative speed, $u$, of the absorber-perturber collision pair, $\rho_J$ is the relative population of the perturber in the $|J, v = 0\rangle$ state, and $S$ is the complex differential cross section representing the collisional efficiency, which includes contributions from the intermolecular potential. $r_{c0}$, $r_c$ and $u'_c$ are position and velocity parameters related to the parabolic relative trajectories [33, 35, 37, 38].

For the $N_2$ and $O_2$ colliders the intermolecular potential is calculated directly from the known dipole, quadrupole, octapole and hexadecapole moments of $NH_3$ and the colliders as well as the induction and dispersion energy contributions. For the rare gases, where no accurate interaction potential is known, a potential described by Legendre polynomials up to second order terms is used [29]. The four coefficients of the repulsive and attractive parts in this potential are treated as adjustable variables. Since the data presented constitute only four transitions, any calculations based on these data should be treated with caution and should be tested over a wider range of measurements. Therefore, calculations for the rare gas data are not reported here. Since the calculations for $N_2$ and $O_2$ colliders require only known parameters to calculate the intermolecular potential, these have been undertaken for the transitions studied

here. The molecular parameters used in these calculations are shown in Table 2.3 and Table 2.4.

**Table 2.3 Molecular parameters for $NH_3$, $O_2$ and $N_2$ used in the theoretical calculations.**

| **Molecule** | **$NH_3$** | **$O_2$** | **$N_2$** |
|---|---|---|---|
| M (u.m.a) | 17.03 | 31.9988 | 28.013 |
| $\mu_i$ (D) | 1.4715 [56] | 0 | 0 |
| Q (D Å) | -2.32[39] | -0.40[37] | -1.30[37] |
| Ω (D Å$^2$) | -1.20[39] | 0 | 0 |
| Φ (D Å$^3$) | – | 4.30[39] | 2.7[39] |
| σ (Å) | 3.018[40] | 3.58[41] | 3.816[42] |
| ε (K) | 294.3[40] | 117.51[42] | 92.91[42] |
| $\alpha_i$ (Å$^3$) | 2.18[39] | 1.5812[40] | 1.74[40] |
| U (ev) | 10.16[43] | 12.063[43] | 15.576[43] |
| γ | 0.054[39] | 0.238[39] | 0.137[39] |
| $A_{//}$ (Å$^4$) | -0.0633[35] | 0 | 0 |
| $A_{\perp}$ (Å$^4$) | 0.793[35] | 0 | 0 |

**Table 2.4 Rovibrational parameters used in the calculations for $NH_3$ in the ground and ($\upsilon_1$ + $\upsilon_3$) states, and for $O_2$ and $N_2$ in the ground vibrational state.**

| **Molecule** | **State** | | **B (cm$^{-1}$)** | **(C-B) (cm$^{-1}$)** | **D (10$^{-4}$cm$^{-1}$)** | **$D_{JK}$ (10$^{-4}$cm$^{-1}$)** | **$D_K$ (10$^{-4}$cm$^{-1}$)** |
|---|---|---|---|---|---|---|---|
| $NH_3$ | Grd. [44] | s | 9.94664 | -3.71828 | 8.4953 | -15.783 | 10.107 |
| | | a | 9.94159 | -3.71123 | 8.32742 | -15.3197 | 9.78949 |
| | $\nu_1+\nu_3$ [45] | s | 9.9500 | -3.8309 | 8.3370 | -24.5772 | 5.9024 |
| | | a | 9.9444 | -3.8405 | 21.6163 | -59.0978 | 23.9308 |
| $O_2$ | Grd.[46] | | 1.437654 | _ | 4.837 10$^{-2}$ | _ | _ |
| $N_2$ | Grd.[47] | | 1.989622 | – | 5.763 10$^{-2}$ | – | – |

The calculated pressure broadening coefficients, together with the experimental results obtained, are shown in Table 2.5. The calculated values show good agreement with the experimental data considering that the expected accuracy of the calculations is around 20% [55].

**Table 2.5 Experimental and theoretical values of the broadening coefficients for diatomic gases.**

| Line | Frequency | $\gamma$-$O_2$ | | $\gamma$-$N_2$ | |
|---|---|---|---|---|---|
| | | Exp | Calc | Exp | Calc |
| **B1 $^{R}$Q(4,1)** | 6595.923 | 2.10 | 1.94 | 3.45 | 3.90 |
| **B2 $^{Q}$P(10,6)** | 6595.616 | 1.44 | 1.48 | 2.75 | 3.42 |
| **C1 $^{R}$Q(5,1)** | 6595.241 | 2.19 | 1.93 | 2.80 | 3.58 |
| **C2 $^{R}$Q(5,1)** | 6595.063 | 1.81 | 1.93 | 3.52 | 3.58 |

## 2.4.2. Parmenter Seaver Calculations

It has been shown that it is possible to estimate the well depth of the ammonia dimer from the broadening coefficients for a range of the colliders using the Parmenter-Seaver relationship [22], however it is emphasised that this relationship is best used as a qualitative tool for prediction and comparison.

The collisional cross section, $\sigma_M$, is related to the pressure measured broadening parameter, $\gamma$, as follows:

$$\sigma_M = \frac{\gamma 2\pi k_B T}{V_{rel}}$$ **Equation 2.15**

where $k_B$ is the Boltzmann constant, T is the temperature and $V_{rel}$ is the mean relative speed of the collision partners.

For collision induced state changes between an excited molecule A* and a collider M, Parmenter and Seaver [48] defined the following correlation between the collisional cross-section, $\sigma_M$, and the intermolecular well depth:

$$\sigma_M = C\exp(\varepsilon'_{A*M}/k_BT) \qquad \textbf{Equation 2.16}$$

where C is a collection of constants (depending on the model used) and $\varepsilon'_{A*M}$ is proportional to the intermolecular well depth for A* with collider M, where A* and A refer to the excited and relaxed states of the perturbed species. Well depths involving the excited state, A*, are assumed to be approximately equal to those involving the relaxed state, A.

As noted by Parmenter and Seaver [48], the interpretation of $\varepsilon'_{A*M}$ should be approached with caution as it is only proportional to the true well depth $\varepsilon_{A*M}$ to within a factor of 2, with the exact proportionality constant dependent on the form of the model chosen to represent the potential. Assuming that $\varepsilon'_{A*M} \approx \varepsilon_{A*M}$ and the proportionality constant = 1, then, a plot of ln $\sigma_M$ against $\varepsilon_{A*M}$ should yield a straight line, with a slope of $1/(k_BT)$.

Since the intermolecular potentials for the interaction between the colliding species have not always been investigated, the interspecies well depth is usually substituted by the geometric mean:

$$\varepsilon'_{A^*M} = (\varepsilon'_{A^*A^*} \times \varepsilon_{MM})^{1/2} \qquad \textbf{Equation 2.17}$$

Here $\varepsilon_{MM}$ is the well depth for the dimer species MM (and is generally well known) and $\varepsilon'_{A^*A^*}$ is proportional to that of the A* molecules and contains the well depth correction. The cross-section, therefore, becomes:

$$\sigma_M = C \exp[\beta(\varepsilon_{MM} / k_B)^{1/2}] \qquad \textbf{Equation 2.18}$$

with

$$\beta = (\varepsilon'_{A^*A^*} / k_B T^2)^{1/2} \qquad \textbf{Equation 2.19}$$

From this, a plot of $\ln(\sigma_M)$ against $(\varepsilon_{MM}/k)^{1/2}$, yields a gradient $\beta$, from which the broadening with different gases can be calculated. Equation 2.19 gives the gradient of the linear fit of the data as $\beta$, from which $\varepsilon'_{A^*A^*}$ can be extracted (usually assumed to be roughly equal to $\varepsilon_{AA}$) and used to estimate the potential well depth of the dimer. In Figure 2.9, the Parmenter-Seaver plot for the C2 transition is shown.

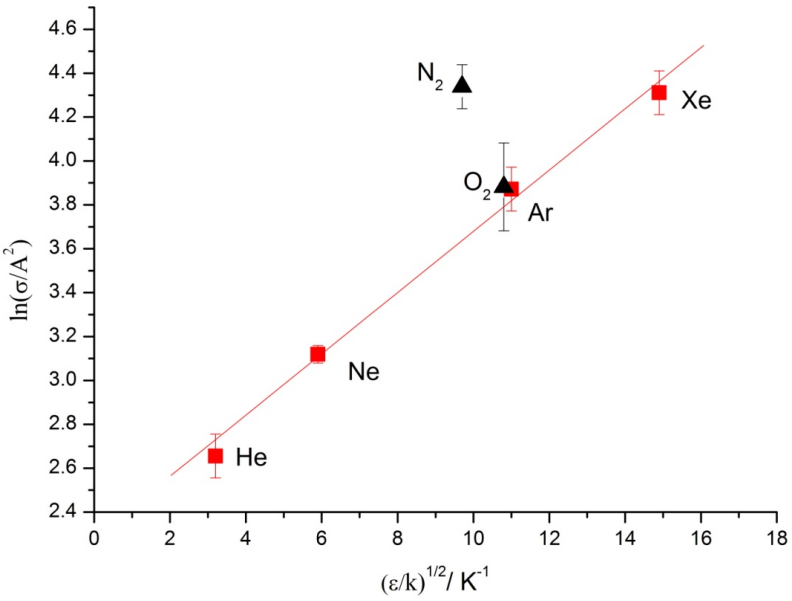


**Figure 2.9 Parmenter-Seaver plot using the pressure broadening coefficients of the C2 line of ammonia.**

The data points for the rare gases, which all have a dipole induced dipole interaction with the ammonia gas, lie on a straight line. The fitted line does not include the points for the diatomic molecules, oxygen and nitrogen, since the dominant intermolecular interaction is of a different type (e.g. dipole quadrupole as in the case of $N_2$). The slope of the rare gas data on the Parmenter-Seaver plot was thus used to calculate the dimer binding energies and the results for each transition are given in Table 2.6. These binding energies show variation, as might be expected given the transitions have different upper rotational states.

**Table 2.6 Measured and theoretical values for the potential dimer well depth for ammonia, U, calculated as explained in the text.**

| Ammonia | This work line B1 | This work line B2 | This work line C1 | This work line C2 | This work average | Theory result [49] | Theory result [50] |
|---|---|---|---|---|---|---|---|
| **U (kJ mol$^{-1}$)** | 13.9 ± 0.2 | 14.5 ± 0.2 | 11.6 ± 0.1 | 15.8 ± 0.1 | 13.9 ± 1.8 | 13.6 | 13.2 |

The average binding energy from these transitions is 13.9 ± 1.8 kJ mol$^{-1}$. Theoretical calculations of the dimer well depth of ammonia have been reported in the literature [49, 50] and give values of 13.6 and 13.2 kJ mol$^{-1}$, respectively, corresponding well with the average value found from the slopes of the Parmenter-Seaver plots.

## 2.4.3. Pressure Shift Measurements

Figures 2.10 and 2.11 show the shift in line centre as a function of pressure for each of the six added gases, for which the gradient of the linear fit yields the pressure shift coefficient, δ. The results for the measured shift coefficients, δ, in MHz Torr$^{-1}$ for He, Ne, Ar, Xe, $O_2$ and $N_2$ are given in Table 2.7.

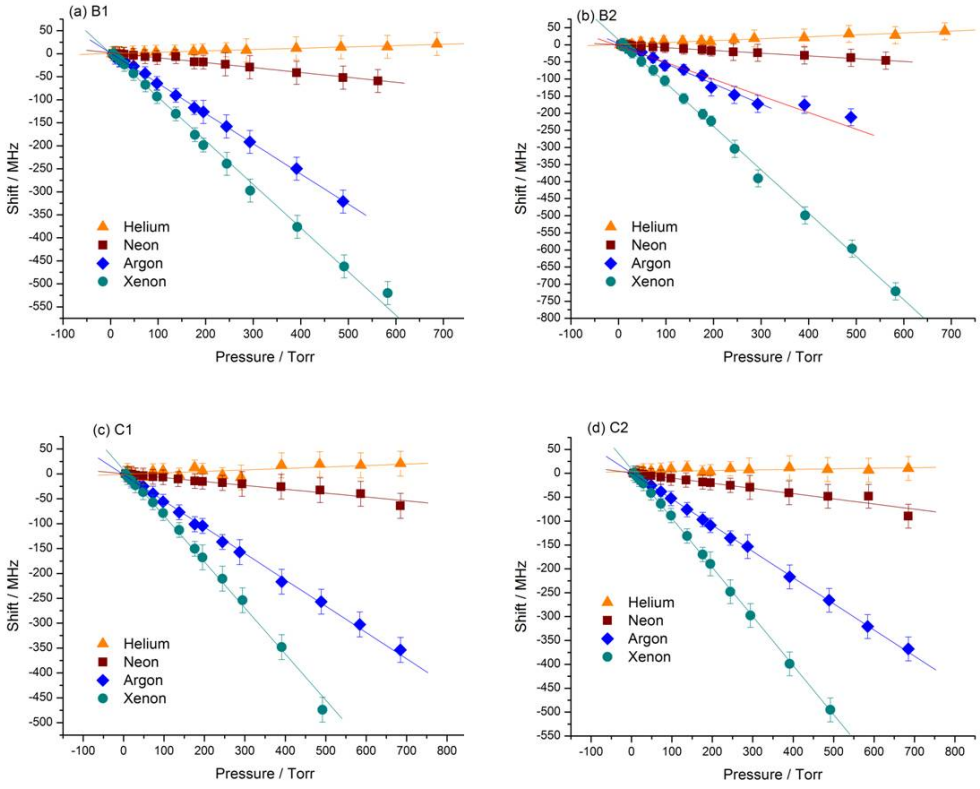


**Figure 2.10 Line centre shift versus pressure for the (a) B1, (b) B2, (c) C1 and (d) C2 lines of ammonia for the rare gases-He, Ne, Ar and Xe.**

**Table 2.7 Pressure shift coefficients for the four absorption lines with six collision partners. Errors were calculated as explained in the text.**

| | | Pressure shift coefficients / MHz Torr$^{-1}$ | | | | | |
|---|---|---|---|---|---|---|---|
| **Line** | Frequency / cm$^{-1}$ | δ-He | δ -Ne | δ -Ar | δ -Xe | δ -$O_2$ | δ - $N_2$ |
| **B1 $^{R}$Q(4,1)** | 6595.923 | 0.03±0.03 | -0.11±0.03 | -0.66±0.03 | -0.95±0.03 | -0.47±0.04 | -0.33±0.05 |
| **B2 $^{Q}$P(10,6)** | 6595.616 | 0.06±0.03 | -0.08±0.03 | -0.48±0.06 | -1.27±0.03 | -0.55±0.03 | -0.54±0.05 |
| **C1 $^{R}$Q(5,1)** | 6595.241 | 0.03±0.03 | -0.08±0.03 | -0.53±0.03 | -0.93±0.04 | -0.34±0.03 | -0.32±0.03 |
| **C2 $^{R}$Q(5,1)** | 6595.063 | 0.01±0.03 | -0.11±0.03 | -0.56±0.03 | -1.03±0.04 | -0.52±0.03 | -0.30±0.03 |

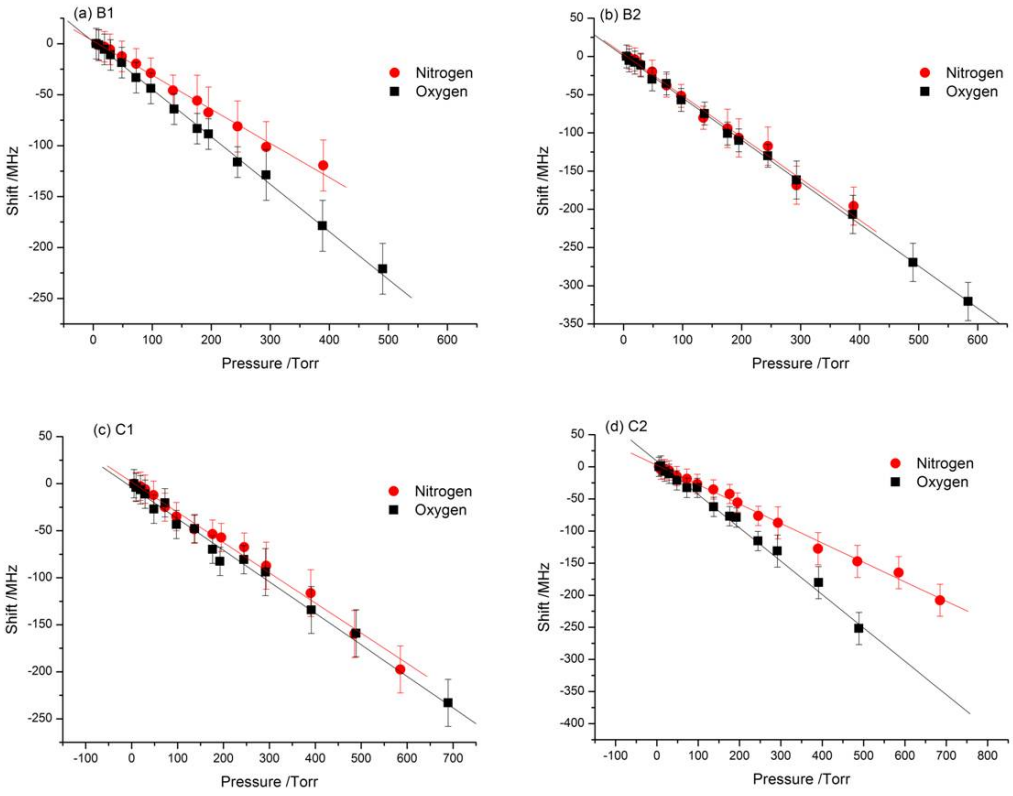


**Figure 2.11 Line centre shift versus pressure for the (a) B1, (b) B2, (c) C1 and (d) C2 lines of ammonia for the diatomic gases $O_2$ and $N_2$.**

It is noted that line shifts are (with the exception of collisions with He) all negative, which would be expected if the perturbed transition took place between levels which were lowered by attractive interactions to a larger extent in the excited state than in the ground state. Shifts in other vibrational bands have been observed to be positive for $\upsilon_2$ [34, 51] and $2\upsilon_2$ [52, 53] and negative for $\upsilon_4$ [52, 54, 55].

To describe the shift theoretically, the intermolecular potentials between ammonia and the collider for the both the upper and lower states of the transi-

tion must be considered. One major contributor to the intermolecular potential can be associated with the dipole moment of the ammonia molecule. This depends crucially upon vibrational quantum numbers [56], and has been measured to be higher in the ($\upsilon_1 + \upsilon_3$) level (1.5167 D) [56] than in the ground state (1.472 D). When there is a large change in dipole moment between the ground and excited states, the change in the intermolecular potentials will be dominated by this and we would expect the sign of the shift to follow the change. However, if the change in dipole moment is small then additional terms (e.g. the polarisability or other long range parameters) must be taken into account.

Pressure shifts occur due to interactions between the two colliding pairs, for example $NH_3$ and Ar, with dipole moments being important contributors to the intermolecular potentials. The change in intermolecular potentials is responsible for the shift. At large separation distances between the collider and the ammonia, there is no interaction and so the energy levels remain at the same distance apart, and there is no shift (as there is no change in the intermolecular potential. However, at closer distances, interaction occurs. The strength of this interaction depends on the dipole moment strength of the collider. Measurements have shown [56] that the temporary induced dipole (on the Argon collider due to its polorisability) will interact more strongly with

the upper state in ammonia than with the ground state, due to the dipole moment in the upper state (1.5167D) being greater than that of the ground state (1.472D). This increased interaction with the upper state causes a reduction in the energy level of that state, therefore the overall transition between ($\upsilon_1 + \upsilon_3$) and the ground state becomes smaller with increasing pressure, thus shifting the line centre to lower wavenumbers. If the dipole moment were larger in the ground state than upper state, then a positive shift would occur.

Table 2.8 shows that the largest difference in dipole moment is -0.2266 D [56] between the $\upsilon_2 = 1$ level and the ground state and this is observed to give rise to a positive shift [34].

**Table 2.8 Dipole moments for the ground state and the vibrationally excited states under consideration [37].**

| Band | Dipole moment (Debyes) | Change in dipole (Debyes) | Observed Shift sign |
|---|---|---|---|
| **ground state** | 1.4715 | - | - |
| $\upsilon_1 + \upsilon_3$ | 1.5167 | 0.0452 | negative |
| $\upsilon_2$ | 1.2449 | -0.2266 | positive |
| $\upsilon_4$ | 1.4554 | -0.0161 | negative |

It can be seen that the change in dipole moments for both the $\upsilon_4$ and the ($\upsilon_1 + \upsilon_3$) band are much smaller than for the $\upsilon_2$ band but similar in magnitude, although they have different signs. These are observed to give a negative shift,

suggesting that other long range parameters are indeed important and that they tentatively favour a negative shift since they overcome the positive shift we might expect from the change in dipole moment of the $\upsilon_4$ band.

Following on from the broadening calculations which were undertaken for $N_2$ and $O_2$, the Robert and Bonamy (RB) theory is also used to calculate the line shift for these colliders. This theory has been successfully used in the past to account for the magnitude and sign of the shifts in other bands [34, 51, 54, 55]. Central to the calculation of the line shift is the $S^{iso}_1$ term (given in ref [55]) which includes both a term arising from the change in dipole between the ground and exited states and an adjustable term accounting for other long range forces (polarisability in the case of $O_2$). The full line shift calculations involve the following three inputs: the molecular parameters found in Tables 2.3 and 2.4, the dipole moments found in Table 2.8 and an additional single adjustable term to account for intermolecular forces. The values for the adjustable term used, following the same terminology as Dhib *et al*. [52], are $\Delta\alpha$ = 0.08 Å$^3$ for the $NH_3$-$O_2$ system and $\Delta C_6/C_6$ = 0.02 for the $NH_3$-$N_2$ system. These values are similar (within a factor of 2) to values used to calculate the correct magnitude and sign of shift coefficients across a range of bands and colliders [29, 33, 34, 52, 54, 55].

The results of these calculations (performed by Dr Dhib) together with our experimental measurements are presented in Table 2.9. As can be seen these show good agreement, successfully accounting for both the magnitude and the sign of the shift for both colliders.

**Table 2.9 Experimental and theoretical values of the pressure shift coefficients for the diatomic gases.**

| **Line** | **Frequency** | **δ-$O_2$** | | **δ-$N_2$** | |
|---|---|---|---|---|---|
| | | Exp | Calc | Exp | Calc |
| **B1 $^{R}$Q(4,1)** | 6595.923 | -0.47 | -0.51 | -0.33 | -0.32 |
| **B2 $^{Q}$P(10,6)** | 6595.616 | -0.55 | -0.60 | -0.54 | -0.39 |
| **C1 $^{R}$Q(5,1)** | 6595.241 | -0.34 | -0.56 | -0.32 | -0.37 |
| **C2 $^{R}$Q(5,1)** | 6595.063 | -0.52 | -0.56 | -0.30 | -0.37 |

It is noted that the sign of the shift of all of the data for this work is the same and negative with the exception of He where a small positive shift is observed. This is consistent with the trend observed in measurements of the line shift for other bands, where the sign is the same for a variety of colliders, for example the $\upsilon_4$ band has been observed to have a negative shift for $H_2$, $CO_2$, $N_2$, Ar, and some He transitions [52, 54]. The He data for the $\upsilon_4$ was observed to be close to zero and also displayed a small positive shift for some transitions [53], again consistent with the trend observed. These trends are also seen in theoretical calculations using the RB theory for He and Ar, where one of the terms

in this RB theory for the line shift includes the effect of polarisability. Based on these, an increase in line shift with the polarisability trend though the rare gases is to be expected. The data for He, although small in value and close to the detection limit, appear to be slightly positive and presumably indicate the importance here of either the repulsive part of the potential or higher order terms.

## 2.5. Conclusion

In this chapter, CEAS around 1516 nm has been used to measure the pressure broadening and pressure shift coefficients for four transitions in the ($\upsilon_1 + \upsilon_3$) combination band of ammonia. Work in the ($\upsilon_1 + \upsilon_3$) combination band has important uses in atmospheric sensing and accurate knowledge of line broadening and shift coefficients is both useful and necessary. The relative ease with which a CEAS setup can be used to measure the accurate line parameters as shown here, with a sensitivity of $6 \times 10^{-8}$ $cm^{-1}$ $Hz^{-1/2}$, is encouraging for atmospheric monitoring due to the relative simplicity of the setup and ease of data acquisition. The sensitivity of this setup could easily be improved by employing higher reflectivity mirrors resulting in a higher finesse cavity.

To our knowledge, this is the first reported measurement of pressure shift coefficients in this band. Comparisons of the broadening coefficients with pre-

vious work in this region, where it exists, show good agreement. Calculations for the pressure broadening and shift coefficients of nitrogen and oxygen have been undertaken using the Robert and Bonamy theory and these are also in good agreement. Both the broadening and shift coefficients show a clear trend through the rare gases, which can be explained in terms of the varying magnitude of the long range attractive forces operating between the colliding partners. The measured pressure broadening coefficients are used to estimate the potential well depth of the ammonia dimer using the Parmenter-Seaver formalism. The obtained well depth agrees well with theoretical calculations.

The remainder of this thesis explores more complex but increasingly sensitive diode laser spectroscopic techniques, in order to improve the detection sensitivity from the $6 \times 10^{-8}$ $cm^{-1}$ $Hz^{-1/2}$ obtained here, to higher sensitivities, approaching the $10^{-12} - 10^{-11}$ $cm^{-1}$ necessary for atmospheric detection of $HO_2$ in real-world scenarios. The following Chapter 3 presents a more theoretical description of the basic optical cavity technique used here, followed by an expansion to more complicated CEAS based techniques, modulation spectroscopy and finally ultra-sensitive laser absorption spectroscopy, NICE-OHMS. Chapters 4 and 5 build on the theoretical basis of the experiments presented in Chapter 3, and present applications of various sensitive absorption techniques to atmospherically important species, such as $CH_4$, $N_2O$, $CO_2$ and $HO_2$.

## References


[1] M. Sutton, S. Reis, S.M.H. Baker (eds), *Atmospheric Ammonia*, Springer (2009)
[2] L.-H. Xu, Z.F. Liu, I. Yakovlev, M.Y.Tretyakov, R.M. Lees, *Infrared Physics*, **45,** 31-45 (2004)
[3] G. Berden, R. Peeters , G. Meijer, *Chemical Physics Letters*, **307,** 131-138 (1999)
[4] A.S. Pine, V.N. Markov, *Journal of Molecular Spectroscopy*, **228,** 121-142 (2004)
[5] M.E. Webber, D.S. Baer, R.K. Hanson, *Applied Optics*, **40**, 2031-2042 (2001)
[6] A. Lucchesini, S. Gozzini, *European Physical Journal D*, **22,** 209-215 (2003)
[7] A. Predoi-Cross, M. Brawley-Tremblay, L. R. Brown, V. M. Devi, D. C. Benner, *Journal of Molecular Spectroscopy*, **236,** 201-215 (2006)
[8] R. Engeln, G. Berden, R. Peeters, G. Meijer, *Review of Scientific Instruments*, **69,** 3763-3769 (1998)
[9] R. Peeters, G. Berden, A. Apituley, G. Meijer, *Applied Physics B – Lasers and Optics*, **71**, 231-236 (2000)
[10] J.B. Paul, L. Lapson, J.G. Anderson, *Applied Optics*, **40,** 4904-4910 (2001)
[11] R. Peeters, G. Berden, G. Meijer, *American Laboratory*, **33,** 60-68 (2001)
[12] M. Mazurenka, A.J. Orr-Ewing, R. Peverall, G.A.D. Ritchie, *Annual Reports on the Progress of Chemistry, Section C*, **101**, 100-142 (2005)
[13] J. Morville, S. Kassi, M. Chenevier, D. Romanini, *Applied Physics B – Lasers and Optics*, **80,** 1027-1038 (2005)
[14] L. Gianfrani, R.W.Fox, L. Hollberg, *Journal of the Optical Society of America B*, **16**, 2247-2254 (1999)
[15] S.E. Fiedler, A. Hese, A.A. Ruth, *Chemical Physics Letters*, **371**, 284-294 (2003)
[16] J. Altmann, R. Baumgart, C. Weitkamp, *Applied Optics*, **20**, 995–999 (1981)
[17] J. Ye, L.-S. Ma, and J.L. Hall, *Journal of the Optical Society of America B*, **15**, 6–15 (1998)
[18] L.S. Rothman,D. Jacquemart, A. Barbe, D.C. Benner, M. Birk, L.R. Brown, M.R. Carleer, C. Chackerian, Jr., K. Chance, L.H. Coudert, V. Dana, V.M. Devi, J.-M. Flaud, R.R. Gamache, A. Goldman, J.-M. Hartmann, K.W. Jucks, A.G. Maki, J.-Y. Mandin, S.T. Massie, J. Orphal, A. Perrin, C.P. Rinsland, M.A.H. Smith, J. Tennyson, R.N. Tolchenov, R.A. Toth, J. Vander Auwera, P. Varanasi, G. Wagner, *Journal of Quantitative Spectroscopy and Radiative Transfer*, **96,** 139-204 (2005)
[19] J.S. Gibb, G. Hancock, R. Peverall, G.A.D. Ritchie, L.J. Russell, *European Physical Journal D*, **28**, 59-66 (2004)
[20] M.A. Koshelev, M.Y.Tretyakov, R.M. Lees, L.-H. Xu, *Applied Physics B – Lasers and Optics*, **85**, 273-277 (2006)
[21] L. Lundsberg-Nielsen, F. Hegelund, F.M. Nicolaisen, *Journal of Molecular Spectroscopy*, **162**, 230-245 (1993)
[22] H.R. Barry, L. Corner, G. Hancock, R. Peverall, T.L. Ranson, G.A.D. Ritchie, *Physical Chemistry Chemical Physics*, **5**, 3106-3112 (2003)
[23] R.G. Gordon, *Journal of Chemical Physics*, **44**, 3083-3089 (1966)
[24] V. Nemtchinov, K. Sung, P. Varanasi, *Journal of Quantitative Spectroscopy and Radiative Transfer*, **83,** 243-265 (2004)
[25] H. Aroui, M. Broquier, A. Picard-Bersellini, J.-P. Bouanich, M. Chevalier, S. Gherissi, *Journal of Quantitative Spectroscopy and Radiative Transfer*, **60,** 1011-1023 (1998)

[26] S. Nouri, J. Orphal, H. Aroui, J.-M. Hartmann, *Journal of Molecular Spectroscopy*, **227,** 60-66 (2004)
[27] V.N. Markov, A.S. Pine, G. Buffa, O. Tarrini, *Journal of Quantitative Spectroscopy and Radiative Transfer*, **50**, 167-178 (1993)
[28] A.S. Pine, V.N. Markov, G. Buffa, O. Tarrini, *Journal of Quantitative Spectroscopy and Radiative Transfer*, **50**, 337-348 (1993)
[29] M. Dhib, J.-P. Bouanich, H. Aroui, M. Broquier, *Journal of Molecular Spectroscopy*, **202**, 83-88 (2000)
[30] D.M. O'Leary, J. Orphal, A.A. Ruth, U. Heitmann, P. Chelin, C.E. Fellows, *Journal of Quantitative Spectroscopy and Radiative Transfer*, **109**, 1004-1015 (2008)
[31] J.S. Gibb, G. Hancock, R. Peverall, G.A.D. Ritchie, *Applied Physics B – Lasers and Optics*, **76,** 97-105 (2003)
[32] S. Hadded, H. Aroui, J. Orphal, J.-P. Bouanich, J.-M. Hartmann, *Journal of Molecular Spectroscopy*, **210**, 275-283 (2001)
[33] M. Dhib, J.-P. Bouanich, H. Aroui, A. Picard-Bersellini, *Journal of Quantitative Spectroscopy and Radiative Transfer*, **68**, 163-178 (2001)
[34] M. Dhib, N.Ibrahim, P. Chelin, M.A. Echargui, H. Aroui, J. Orphal, *Journal of Molecular Spectroscopy*, **242,** 83-89 (2007)
[35] D. Robert, J. Bonamy, *Journal de Physique*, **40**, 923-943 (1979)
[36] C.L. Bell, M. Dhib, G. Hancock, G.A.D. Ritchie, J.H. van Helden, N.J. van Leeuwen, *Applied Physics B – Lasers and Optics*, **94**, 327-336 (2009)
[37] M. Dhib, J.-P. Bouanich, H. Aroui and M. Broquier, *Journal of Molecular Spectroscopy*, **202**, 83-88 (2000)
[38] M. Dhib, *Journal of Molecular Spectroscopy*, **259**, 80-85 (2010)
[39] C.G. Gray, K.E. Gubbins, *Theory of Molecular Fluids, Volume 1: Fundamentals*, Clarendon Press, Oxford (1984)
[40] S.V. Khiristenko, A.I. Maslov, V.P. Shevelko, *Molecules and their Spectroscopic Properties*, Springer, Berlin (1998)
[41] J.O. Hirschfelder, C.F. Curtiss, R.B. Bird, *Molecular Theory of Gases and Liquids*, Wiley, New York (1967)
[42] J.-P. Bouanich, G. Blanquet, J. Walrand, *Journal of Molecular Spectroscopy*, **161**, 416-426 (1993)
[43] J. Komasa, A.J. Thakkar, *Molecular Physics*, **78**, 1039-1046 (1993)
[44] S. Urban, V. Spirko, D. Papousek, J. Kauppinen, S.P. Belov, L.I. Gershtein, A.F. Krupnov, *Journal of Molecular Spectroscopy*, **88**, 274-292 (1981)
[45] L.-H. Xu, Z.F. Liu, I. Yakovlev, M.Y.Tretyakov, R.M. Lees, *Infrared Physics*, **45,** 31-45 (2004)
[46] T. Amano, E. Hirota, *Journal of Molecular Spectroscopy*, **53,** 346-363 (1974)
[47] D. Reuter, D.E. Jennings, J.W. Brault, *Journal of Molecular Spectroscopy*, **115**, 294-304 (1986)
[48] H.-M. Lin, M. Seaver, K.Y. Tang, A.E.W. Knight, C.S. Parmenter, *Journal of Chemical Physics*, **70**, 5442-5457 (1979)
[49] C. Diedrich, A. Lüchow, S. Grimme, *Journal of Chemical Physics*, **123**, 184106 (2005)
[50] J.S. Lee, S.Y. Park, *Journal of Chemical Physics*, **112,** 230-237 (2000)
[51] G. Baldacchini, F. D'Amato, G. Buffa, O. Tarrini, M. De Rosa, F. Pelagalli, *Journal of Quantitative Spectroscopy and Radiative Transfer*, **68**, 625-633 (2001)
[52] M. Dhib, M.A. Echargui, H. Aroui, J. Orphal, J.-M. Hartmann, *Journal of Molecular Spectroscopy*, **233**, 138-148 (2005)
[53] F. Raynaud, B. Lemoine, F. Rohart, *Journal of Molecular Spectroscopy*, **168**, 584-592 (1994)

[54] M. Dhib, M.A. Echargui, H, Aroui, J. Orphal, *Journal of Molecular Spectroscopy*, **238**, 168-177 (2006)

[55] M. Dhib, H, Aroui, J. Orphal, *Journal of Quantitative Spectroscopy and Radiative Transfer*, **107,** 372-384 (2007)

[56] M.D. Marshall, K.C. Izgi, J.S. Muenter, *Journal of Chemical Physics*, **107**, 1037-1044 (1997)

# Chapter 3
# Theoretical development of NICE-OHMS

## 3.1. Introduction

Previously in this thesis, the use of detection methods for trace gases has been introduced and discussed, noting that the development of these techniques was enhanced by the availability of high performance and economically viable diode lasers from the telecommunications industry. With their ease of use and ever increasing wavelength coverage, particularly in the near infra-red portion of the spectrum, they are an ideal choice for sensitive and selective spectroscopic gas detection. In the previous chapter, the technique of CEAS was introduced. This is a good technique to use when sensitivity does not have to be

of ultimate importance, but the ease of use and robustness of the technique is paramount. However, when the species under investigation are of much lower concentration, for example, for the detection of atmospherically important species, or the analysis of trace compounds in human breath, CEAS often does not provide the required detection sensitivity, and so other techniques to improve the sensitivity of laser absorption spectroscopy must be employed [1]. This can be achieved by a suite of methods including locked CEAS, whereby the laser is locked on resonance with the cavity, utilising the increase in path length **and** signal, and various modulation techniques whereby the detection regime is moved to higher frequencies in order to achieve a reduction in the noise. Noise Immune Cavity Enhanced Optical Heterodyne Molecular Spectroscopy (NICE-OHMS) is an ultra sensitive spectroscopic technique that combines frequency modulation spectroscopy with resonant cavity enhanced spectroscopy. It is one of the most sensitive spectroscopic techniques in existence due to the combination of signal enhancement by the use of the optical cavity, and noise reduction due to the modulation techniques, giving rise to sensitivities which are approaching the shot noise limit [2, 3].

This chapter outlines the theoretical description of modulation spectroscopy within a locked cavity with a view to providing a theoretical description of the NICE-OHMS experiment. A description of frequency modulation spectros-

copy (FMS) is provided first, followed by an application of this through the use of the Pound Drever Hall technique to lock the laser to a resonant cavity. Following this, a description of the application of FMS in a cavity is presented, and finally a description of wavelength modulation spectroscopy (WMS) as the final component of the full NICE-OHMS method, along with simulations of the full NICE-OHMS signals.

## 3.2. Frequency modulation spectroscopy (FMS)

The techniques described previously in this thesis have been primarily concerned with increases in signal size by the use of an optical cavity to enhance the path length. However, residual sources of noise still remain, arising from fluctuations in the laser's frequency stability and output intensity, along with background fluctuations and also frequency dependent 1/f noise. If this residual noise is reduced or effectively eliminated, detection sensitivities approaching that of the shot-noise limit may be attained [4]. A very effective technique for reducing residual noise is that of modulation spectroscopy, where the signal detection is shifted to higher frequencies thereby reducing the contribution of the noise to the measurements [5].

Two variations exist for modulation spectroscopy: frequency and wavelength modulation spectroscopy, which differ only in the regime under which they

operate. The theory of the two modulation spectroscopy methods can most easily be described by considering the specific regime for each case; this is highlighted pictorially in Figure 3.1. If the modulation frequency, $\omega_m$, is small compared to the linewidth, $\Gamma$, of the absorption feature, i.e., $\omega_m << \Gamma$, and the modulation index $\beta$ is large, i.e., $\beta >> 1$, measurements are said to be conducted in the Wavelength Modulation Spectroscopy (WMS) regime [6, 7, 8, 9, 10, 11]. However, if the modulation frequency is similar to or larger than the absorption linewidth, i.e., $\omega_m \geq \Gamma$, and the modulation index is kept small, i.e., $\beta \leq 1$, Frequency Modulation Spectroscopy (FMS) provides a better description. WMS and FMS are thus very closely related, effectively being limiting cases of the various modulations possible. For FMS, when $\beta < 1$, the modulated field consists of a triplet comprised of the carrier frequency, $\omega_0$, and one set of sidebands, with the sideband separation from the carrier frequency, $\omega_m$, being relatively large, so $\omega_{\pm 1} = \omega_0 \pm \omega_m$. In contrast, the corresponding separation for the sidebands in WMS is much smaller, with a progresion of $n$ sidebands on either side of the carrier frequency and so $\omega_{\pm n} = \omega_0 \pm n\omega_m$.

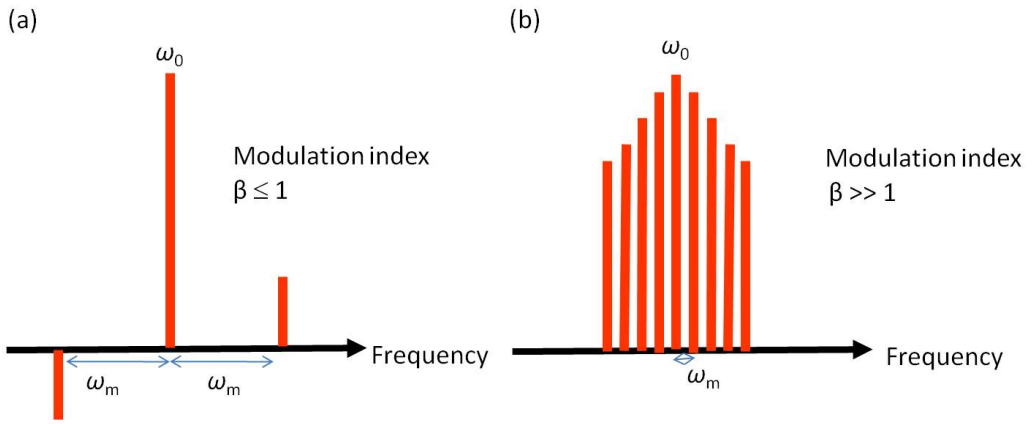


**Figure 3.1 Pictorial representation of FMS (a) and WMS (b) modulation regimes.**

The modulation of the signal therefore involves the imprinting of a sinusoidal variation of the frequency or phase onto a central carrier frequency either by applying the modulation directly to the injection current of a diode laser or externally by the use of an electro-optic modulator (EOM). In FMS, this is manifest as an FM triplet with sidebands at plus and minus the modulation frequency, $\omega_m$, on either side of the central carrier frequency (Fig 3.1(a)). If the modulated light is then passed through an absorbing sample, then the absorption converts some of the frequency modulation (FM) into an amplitude modulation (AM). This can then be detected with a square-law detector and phase sensitive detection techniques, such as a lock-in amplifier or a radio frequency mixer, at the modulation frequency to retrieve the resulting FMS signal in the absorption or dispersion phase. This FMS signal is caused by the combination of the two beat signals from the "beating" of the sidebands

against the central carrier frequency with a beat frequency $\omega_m$. Figure 3.2 shows schematically the effect upon a phase modulated radiation field interacting with an absorption feature and shows the resulting FM absorption signal. When the modulated light frequencies are off resonance, the beat signals from each of the sidebands against the carrier frequency are equal but of opposite sign, and so they cancel out and there is no net signal.

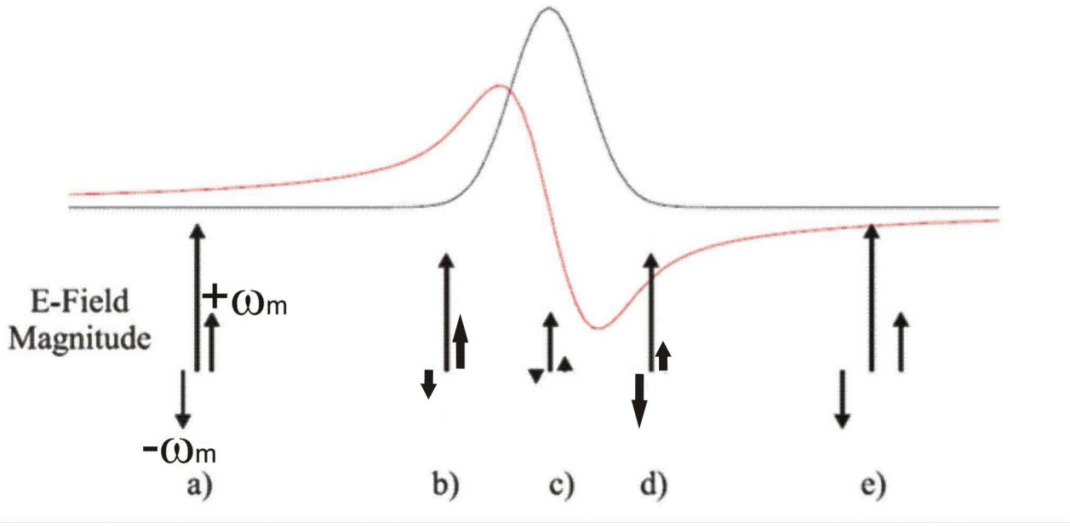


**Figure 3.2 The direct absorption (black) and the corresponding FM absorption signal (red) profiles. The effects upon a phase modulated radiation field are schematically illustrated for the magnitude and phase of the radiation as the carrier frequency is scanned across the resonance. a) Off-resonance the magnitudes of both sidebands are equal. b) +$\omega_m$ sideband magnitude attenuated. c) At line centre, maximum attenuation for the carrier and both sidebands attenuated to same extent. d) –$\omega_m$ sideband magnitude attenuated. e) Off resonance again. Picture modified from [12].**

However, as the carrier frequency passes through the absorption feature, each sideband is attenuated to a different extent, and this causes an imbalance in the beat signals as the carrier frequency is scanned over an absorption feature,

resulting in a non-zero signal. The detected beat signal also cancels out to zero at the transition centre, where the beat signals are equal, as shown in Figure 3.2 (c).

The laser source used in this thesis is an external cavity diode laser (ECDL), with diode lasers providing good light sources to perform FMS as they can be modulated directly by the addition of a radio frequency (rf) signal to their injection current, via the bias-tee. However, although this is economically more desirable, direct rf modulation of the current leads to a phase change in the output signal, and also additional noise which appears as residual amplitude modulation (RAM) on the signal. The RAM interferes with and can mask the required modulated carrier frequency signal, and so is undesirable for ultra sensitive detection techniques. Although more expensive, the use of an EOM placed into the laser beam path to phase modulate the light is much better, greatly reducing the RAM effects when aligned carefully in the experimental system. An EOM provides the modulation for the work presented in the remainder of this thesis.

### 3.2.1. Theoretical description of FMS

Frequency modulation spectroscopy has been described in detail previously by a number of workers [13, 14, 15, 16, 17, 18, 19, 20, 21], and here only a brief

description is given. The unmodulated time-varying electric field of the laser radiation is given by:

$$E(t) = E_0 \exp(i\omega_0 t) \qquad \textbf{Equation 3.1}$$

where $E_0$ is the amplitude and $\omega_0$ is the angular frequency, which is related to the frequency by $\nu = \omega/2\pi$. Modulation of the radiation at a frequency, $\omega_m$, results in modulation of both phase and amplitude:

$$E(t) = E_0[1 + M\sin(\omega_m t + \phi)]\exp[i(\omega_0 t + \beta\sin(\omega_m t))] \qquad \textbf{Equation 3.2}$$

where $\beta$ is the modulation index and $\phi$ is the phase difference between the amplitude and frequency modulation. $M$ is the residual amplitude modulation (RAM) and in pure modulation spectroscopy it is zero. In reality most experiments do have some degree of RAM, though this theoretical description presented here assumes perfect alignment of the EOM and no RAM.

The modulated electric field can therefore be written as:

$$E(t) = E_0 \exp[i(\omega_0 t + \beta\sin\omega_m t)] \qquad \textbf{Equation 3.3}$$

Equation 3.2 can be re-written as a Fourier sum of frequency components:

$$E(t) = E_0 \exp(i\omega_0 t)\sum_{n=-\infty}^{+\infty} J_n(\beta)\exp(in\omega_m t) \qquad \textbf{Equation 3.4}$$

where the modulated field has a progression of $n$ sidebands on either side of the carrier frequency separated by integer multiples of $\omega_m$. The amplitude of

the n$^{th}$ sideband is determined by the n$^{th}$ order Bessel function, $J_n(\beta)$. The symmetry of the Bessel functions vary with $n$ as $J_{-n}(\beta) = (-1)^n J_n(\beta)$, which therefore dictates that even and odd sidebands are in and out of phase with the carrier frequency, respectively. In the limit where $\beta \ll 1$, Equation 3.4 simplifies to the electric field with only three frequency components, the FM triplet:

$$E(t) = E_0\{-J_1(\beta)\exp[i(\omega_0 - \omega_m)t] + J_0(\beta)\exp[i\omega_0 t] + J_1(\beta)\exp[i(\omega_0 + \omega_m)t]\} \quad \textbf{Equation 3.5}$$

When monitoring the light from a frequency modulated laser beam in the current setup on a spectrum analyser, the sidebands can clearly be seen on either side of the carrier frequency, as shown by the data in Figure 3.3. Fitting the amplitude of the three frequency components by the resulting function following Fourier transformation of Equation 3.5 in frequency space provides the modulation index, $\beta$. The modulation index allows suitable modulation amplitudes to be selected for a given absorption profile. In order to obtain the value of $\beta$, the fitting routine approximated each of the three frequency components of the FM triplet to a Lorentzian profile; for the applied modulation frequency of 219 MHz $\beta$ was found to be 0.55.

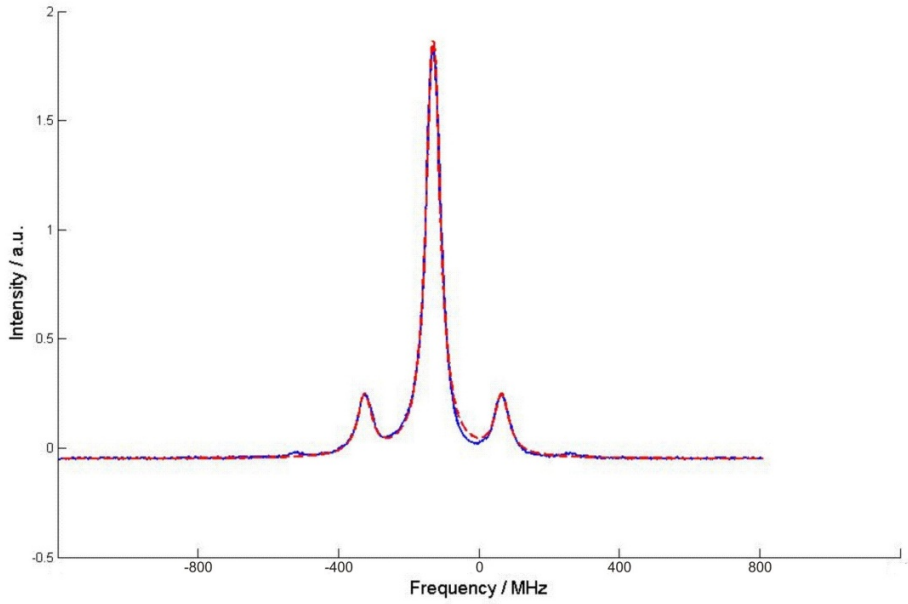


**Figure 3.3 Example of the FM triplet from the spectrum analyser and corresponding fit to return the $\beta$ parameter.**

The transmitted electric field as a result of the interaction of matter with an electric field can be described as:

$$E_T(t) = E(t)T(\omega) \qquad \textbf{Equation 3.6}$$

where $T(\omega)$ is the transmission function. The transmission through an absorbing medium with an absorption coefficient, $\alpha(\omega)$, and a refractive index, $n(\omega)$ is given by the frequency dependent complex transmission function:

$$T(\omega) = \exp\left[(-\delta(\omega)\text{-}i\phi(\omega)\right] \qquad \textbf{Equation 3.7}$$

The frequency dependent amplitude attenuation, $\delta(\omega)$, and associated phase shift, $\phi(\omega)$, describe the absorption and dispersion profiles respectively, reflecting the physical properties of the absorbing medium. In general, the line-

shape profile for the absorption signal is given by the frequency dependence of $\delta$:

$$\delta(\omega) = \frac{\alpha(\omega)L}{2} \qquad \textbf{Equation 3.8}$$

where the absorption coefficient of the sample of length $L$ is $\alpha(\omega)$. Correspondingly the dispersion signal is given by the frequency dependence of $\phi$:

$$\phi(\omega) = \frac{n(\omega)L\omega}{c} \qquad \textbf{Equation 3.9}$$

where $n(\omega)$ is the sample refractive index. Thus, after passing through the sample, the electric field of the FM triplet is:

$$\begin{aligned} E_T(t) = E_0\{&-J_1(\beta)\exp[i(\omega_0-\omega_m)t]\exp[-\delta_{-1}-i\phi_{-1}] \\ &+ J_0(\beta)\exp[i\omega_0 t]\exp[-\delta_0-i\phi_0]+ \\ &+ J_1(\beta)\exp[i(\omega_0+\omega_m)t]\exp[-\delta_1-i\phi_1]\} \end{aligned} \qquad \textbf{Equation 3.10}$$

where the subscripts -1, 0, 1 on $\delta$ and $\phi$ correspond to the frequencies $\omega_0$-$\omega_m$, $\omega_0$, $\omega_0$+$\omega_m$.

The light intensity of the transmitted electric field is proportional to the square of the electric field ($I \alpha |E(t)|^2$) and in the limit of low absorption, where $\alpha L \ll 1$, the absorption leads to an amplitude modulation on the transmitted light given by:

$$\begin{aligned} I(t) = I_0\{&1 + 2J_0(\beta)J_1(\beta)[-\delta_{-1}-\delta_1]\cos(\omega_m t) \\ &+ 2J_0(\beta)J_1(\beta)[\phi_{-1}-2\phi_0-\phi_1]\sin(\omega_m t)\} \end{aligned} \qquad \textbf{Equation 3.11}$$

where $I_0$ is the intensity of the light in the absence of absorbers. For a single absorption feature, the lineshape profiles can be re-written as:

$$\delta(\omega) = \frac{\alpha_p L}{2} \bar{\chi}^{abs}(\omega) \qquad \textbf{Equation 3.12}$$

and

$$\phi(\omega) = \frac{\alpha_p L}{2} \bar{\chi}^{disp}(\omega) \qquad \textbf{Equation 3.13}$$

where $\alpha_p$ is the peak absorption coefficient of the line, $\bar{\chi}^{abs}(\omega)$ is the peak-normalised absorption lineshape function and $\bar{\chi}^{disp}(\omega)$ is the dispersion lineshape function related to $\bar{\chi}^{abs}(\omega)$ through the Kramers-Kronig relations [22, 23]. Note that this does not imply that $\bar{\chi}^{disp}(\omega)$ is peak normalised.

From Equation 3.11, it is clear that the detected FM signal output from the photodetector is a linear combination of both absorption or dispersion signals. In order to extract the pure absorption or dispersion signal, the measured current from the photodetector must first be processed through an I/Q demodulator. The signal from a local oscillator (a reference signal at the specified modulation frequency) is mixed with the photodetector signal and then two separate demodulated signals are output from the double balance mixer and phase shifter (in the I/Q demodulator) with a fixed phase difference of 90° between

them. These two signals are referred to as the In-phase and Quadrature (I and Q) signals and are related to the absorption and dispersion signals through the phase angle $\theta$. This phase difference arises from differences in the path length taken by the local oscillator signal and the detector signal which contains the required modulated absorption information (in this case referring to both an optical path and an electrical path relating to cable lengths etc). At an arbitrary phase, $\theta$, the final output from the double balance mixer and phase shifter will be a sine and cosine weighted sum of the absorption and dispersion contributions:

$$I^{fm}(\omega) = A_{FM}(\omega)\cos\theta + D_{FM}(\omega)\sin\theta \qquad \textbf{Equation 3.14}$$

where $A_{FM}(\omega)$ and $D_{FM}(\omega)$ are the absorption and dispersion components respectively of the signal in FM space. In general, the resulting FM signal after demodulation at an FM detection phase $\theta$ is then given by:

$$\begin{aligned} S^{fm}(\omega_0,\omega_m,\theta) = {} & \eta_{fm} J_0(\beta) J_1(\beta) P_0 \alpha_p L \\ & \times \left\{ \left[ \bar{\chi}^{abs}(\omega_0 - \omega_m) - \bar{\chi}^{abs}(\omega_0 + \omega_m) \right] \cos\theta \right. \\ & \left. + \left[ \bar{\chi}^{disp}(\omega_0 - \omega_m) - 2\bar{\chi}^{disp}(\omega_0) + \bar{\chi}^{disp}(\omega_0 + \omega_m) \right] \sin\theta \right\} \end{aligned} \qquad \textbf{Equation 3.15}$$

where $\eta_{fm}$ is an instrumentation factor that includes the detector responsivity and the gain within the FM detection system and $P_0$ is the incident power.

### 3.2.2. FMS Lineshape analysis

As shown in Equation 3.15, five different lineshapes constitute the FM signals. In order to detect a pure FM absorption signal, the phase $\theta$ is chosen to be 0. The cosine term of the FM signal then gives the resulting absorption signal consisting of the combination of the lineshapes resulting from the leading or trailing sideband resonant with the transition, shown in Figure 3.4.

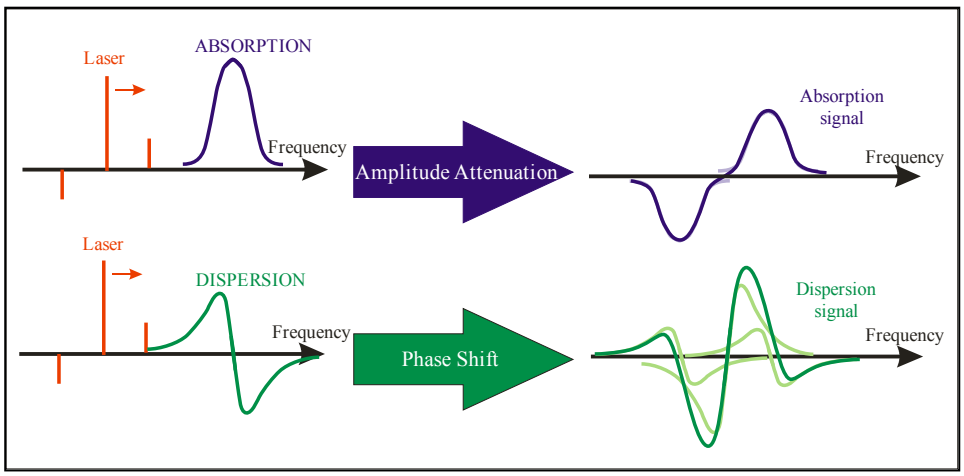


**Figure 3.4 – The resulting absorption and dispersion signals and the 5 different lineshapes from which they are comprised [from 14].**

In order to detect a pure FM dispersion signal, the phase difference is chosen to be $\theta = \pi/2$. The dispersion signal, given by the sine term consist of the combination of three lineshapes, arising from each of the FM triplet components (the carrier plus two sidebands) being resonant with the transition. These are shown in Figure 3.4 where the lineshapes comprising the signals can be seen.

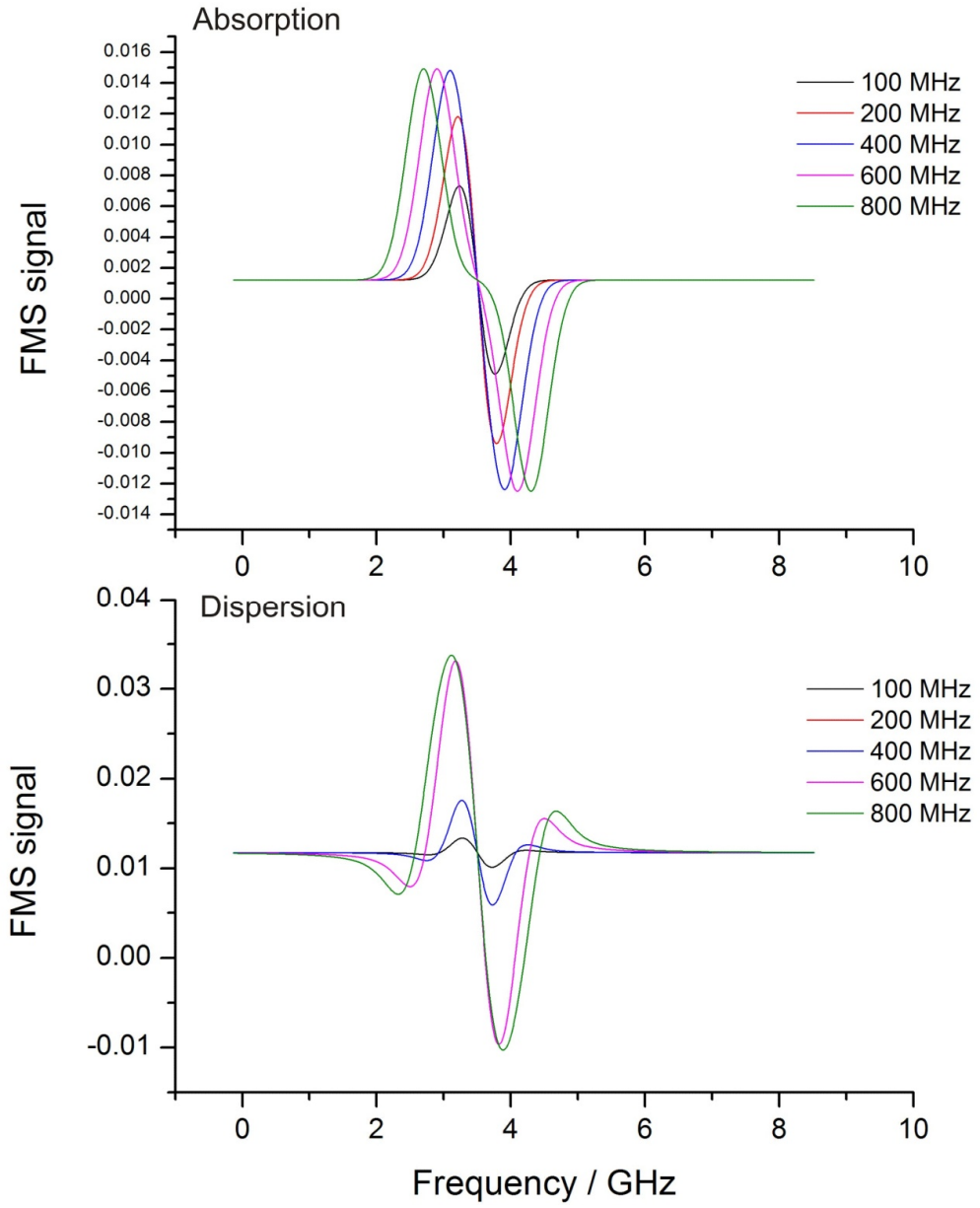


**Figure 3.5 FMS Lineshape variation as a function of the modulation frequency for absorption (with θ=0) upper, and dispersion (with θ=π/2) lower. The dispersion FMS signal is scaled for clarity.**

The results of a simulation of pure absorption and dispersion FM signals varying the modulation frequency can be seen in Figure 3.5. The simulation is for a $CH_4$ transition at low pressure which has a Gaussian width of 611 MHz and

no pressure broadening. The absorption and dispersion lineshape profiles used for this will be discussed later.

## 3.3. Applications of FMS in the NICE-OHMS system

Having outlined the theoretical description of FMS, two applications of FMS in the NICE-OHMS setup are now presented. The first is the active locking of the laser frequency to a resonant cavity mode using the Pound Drever Hall technique, with the second being the application of FMS in an optical cavity to reduce the noise and achieve an increased sensitivity.

### 3.3.1. Pound Drever Hall Locking

In a CEAS experiment, the high reflectivity mirrors provide a greatly enhanced path length within the optical cavity. Coupled with this, if the light injected to the cavity is on resonance with the cavity (i.e. an integer number of wavelengths of the light fit exactly within the cavity), signal enhancement occurs at these points, called cavity modes. In CEAS, the cavity mode structure is purposefully disrupted to excite as many higher order cavity modes as possible as the laser is scanned. This leads to a congested mode structure as a function of frequency resulting in a smooth average transmission. In CEAS, the average transmission of the cavity is very small (< 10 μW generally reaches

the detector). Improvements in the light levels, and therefore the signal to noise ratio, are required for more sensitive gas phase measurements to be undertaken. However, in order to make use of the signal enhancement occurring at a cavity mode, it is necessary to inject light of the correct frequency so that only that single mode is excited. Locked CEAS is a technique which accomplishes this, by locking the laser to the cavity and consequently improving the sensitivity of the detection technique. This provides the first stage of development from a basic CEAS setup towards the NICE-OHMS setup described in this thesis.

With high finesse cavities, because the free running linewidth of the laser is generally an order of magnitude larger than the cavity modes, locking the laser to a single mode of the cavity becomes technically challenging. With varying temperature drifts and mechanical disturbances within the setup and within the laser, the laser needs to be actively controlled and locked to a cavity mode to prevent the drift, and to maximise the transmission through the cavity. The initial lock of the laser to the optical cavity used in the NICE-OHMS technique is effected by use of an electronically controlled feedback technique, called the Pound-Drever-Hall (PDH) technique, a specific application of FMS [24, 25, 26, 27].

In the PDH technique, light which is resonant with the cavity is monitored by measuring the reflected signal from the cavity with a photodiode. It is not possible to use the reflection of a single frequency from the cavity in order to generate the required error signal as, from the intensity change for a single reflection, it is not possible to ascertain whether an increase or decrease in laser frequency is required in order to keep the laser and cavity in resonance. Hence, in order to monitor the light resonant with the cavity, and to produce the necessary error signal to correctly move the laser in the correct frequency direction, frequency modulation (FM) techniques can be used as the signal is 0 on resonance, and + or – on either side.

In order to employ the PDH technique, an Electro-Optic Modulator (EOM) is used to phase modulate the laser light at a frequency $\upsilon_{pdh}$ resulting in sidebands being added to the central carrier frequency at $\pm \upsilon_{pdh}$. The modulation frequency chosen for $\upsilon_{pdh}$ must be smaller than the free spectral range of the cavity, but larger than the linewidth of the laser. In the NICE-OHMS system, $\upsilon_{pdh}$ is chosen to be 25 MHz, with the cavity free spectral range being 109.5 MHz. The modulation frequency is larger than the width of the cavity modes (~50 kHz) so that only the central carrier frequency is transmitted through the cavity, with the sidebands being reflected and monitored. This creates an FM

triplet, of the central carrier frequency of the laser and two sidebands, as shown in Figure 3.6 (a).

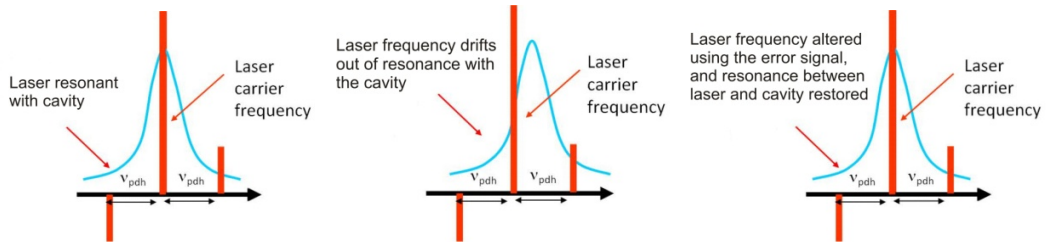


**Figure 3.6 Schematic of the Pound-Drever-Hall locking showing how the technique is used to maintain resonance between the laser and the optical cavity.**

Rather than monitoring the single reflection of the central carrier frequency from the cavity, the beat signal between each sideband and the central carrier is monitored. When the laser is on resonance with the cavity, as shown in Figure 3.6 (a), the beat signals are equal as the sideband phases are equal (but opposite) and so they cancel to zero. However, as can be seen in Figure 3.6 (b), if the laser drifts off resonance with the cavity, the combined beat signal from the sidebands and the carrier is disrupted and is no longer zero, due to the differing absorption effects for each sideband, causing a signal to be recorded on the photodiode. This signal is monitored, and from it, an error signal is generated, such as that shown in Figure 3.7, with the corresponding cavity modes. Following reflection from the cavity, the light is directed on to a fast photodetector.

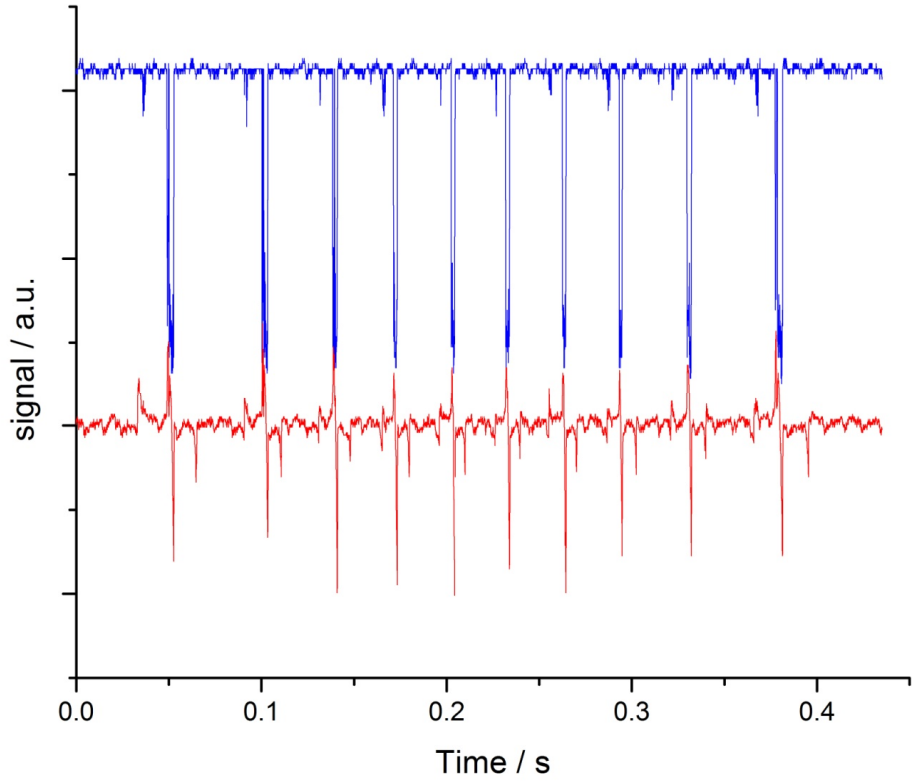


**Figure 3.7 Cavity transmission for an unlocked cavity, drifting in and out of resonance over time (blue), and PDH error signal (red) for locking the laser to the cavity modes. When the laser drifts into resonance with the cavity, this is reflected in the large peaks seen.**

In order to determine whether the reflected cavity signal is on or off resonance with the cavity, the signal received at the photodiode is demodulated using a double balance mixer (DBM) and low pass filtered so that the PDH error signal can be retrieved, and then used in a servo control loop which feeds back to the laser to alter its frequency and bring it back into resonance with the cavity. When the bandwidth of the laser and the gain are optimised for the setup, a narrowing of the laser linewidth occurs thereby increasing the power in the mode to which the laser is locked, maximising the cavity transmission.

Once the laser is locked, it is able to follow a change of frequency induced by a change in the cavity length, which is required to scan across an absorption feature. This is achieved by mounting one or more of the cavity mirrors on a piezo electric transducer (PZT) and applying a voltage ramp to this. This enables the laser to remain locked to the optimal cavity mode whilst scanned across a transition. A discussion of the servo locking system is beyond the scope of this thesis, however it is similar to that described by Fox *et al* [28]. A schematic of the locked CEAS setup is shown in Figure 3.8.

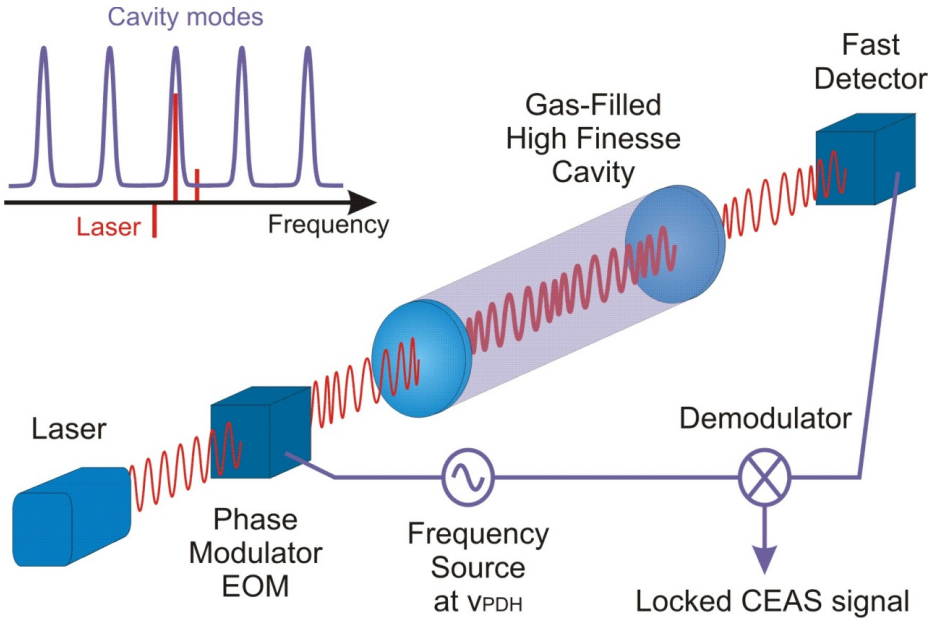


**Figure 3.8 Schematic of the locked CEAS setup with PDH locking.**

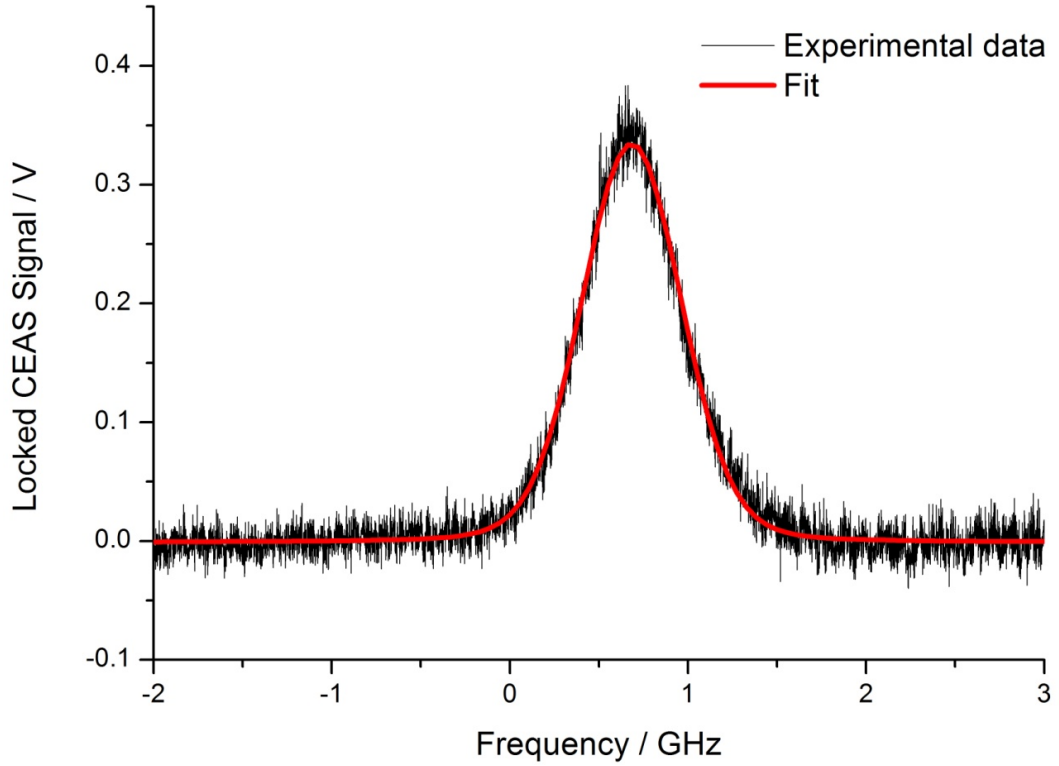


**Figure 3.9 Typical Locked-CEAS spectrum of 25 Torr of $CH_4$ at 6595.90 $cm^{-1}$.**

Figure 3.9 shows a typical locked CEAS trace for 8.59 Torr of $CH_4$ for an unassigned transition at 6595.90 $cm^{-1}$, along with a Voigt fit with the Gaussian width fixed to the calculated Doppler width of 611 MHz for a sample at 298 K. The returned Lorentzian component of the fit was 91 ± 3 MHz which agrees reasonably well with the calculated value for self broadening of 85 MHz [29]. This locked CEAS signal was acquired by scanning over 5 GHz at a scan rate of 1 Hz. The signal was acquired with 20 averages over an acquisition time of 20 seconds. The sensitivity calculated for this spectrum was 2.13 x $10^{-8}$ $cm^{-1}$, for a cavity finesse of 2600. That the sensitivity is not an order of magnitude

better than in Chapter 2, is due to the fact that in locked CEAS part of the frequency modulation is converted into residual amplitude modulation which increases the noise on the signal. Having demonstrated the application of FM to lock the laser to the cavity and then conducted locked CEAS, the next section details a further use of FM to perform frequency modulation spectroscopy on the locked CEAS signal to reduce the noise and further increase the sensitivity.

### 3.3.2. FMS in a Cavity – *fm*-NICE-OHMS

In *fm*-NICE-OHMS, a specific case of frequency modulation spectroscopy is performed with an optical cavity in which the modulation frequency is carefully selected so as to exactly match that of the cavity free spectral range, or multiples thereof. By selecting the FMS modulation frequency, $\omega_{m'}$ to match the free spectral range of the cavity, the "noise-immunity" feature of NICE-OHMS is obtained. As the frequency components of the FM triplet (carrier frequency and sidebands) are all separated by the free spectral range, each is transmitted through the cavity in the same way (i.e. maintaining the resonance with a cavity mode), with each component being affected identically by the cavity. As the *fm*-NICE-OHMS signal arises from the beating between the carrier and the sidebands, the signal is noise-immune to jitters in the laser fre-

quency, which is responsible for most of the sensitivity limiting noise in the signal.

Figure 3.10 shows schematically how the selection of the modulation frequency can be undertaken so as to match exactly the free spectral range of the cavity, thereby coinciding with the cavity modes.

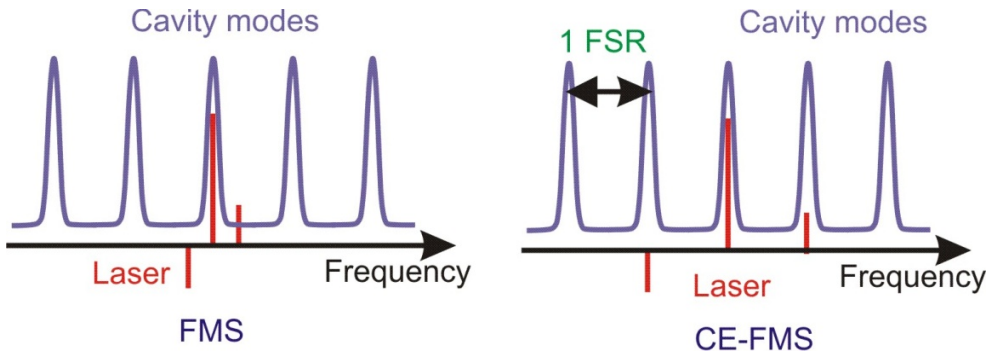


**Figure 3.10 Modulation frequency differences between FMS used for PDH locking and *fm*-NICE-OHMS.**

In NICE-OHMS, the FMS signal is cavity enhanced by a factor of $2F/\pi$ where F is the cavity finesse and so the full *fm*-NICE-OHMS signal can be described by extending the equations in Equation 3.15 with the addition of the cavity enhancement factor and an instrumentation factor, $\eta_{fm}$ to give [18, 30, 31, 32]:

$$S^{fm-no}(\omega_0,\omega_m,\theta)=\eta_{fm}\frac{2F}{\pi}J_0(\beta)J_1(\beta)P_0\alpha_p L \times\left\{\left[\bar{\chi}^{abs}(\omega_0-\omega_m)-\bar{\chi}^{abs}(\omega_0+\omega_m)\right]\cos\theta +\left[\bar{\chi}^{disp}(\omega_0-\omega_m)-2\bar{\chi}^{disp}(\omega_0)+\bar{\chi}^{disp}(\omega_0+\omega_m)\right]\sin\theta\right\} \quad \textbf{Equation 3.16}$$

For purely Doppler-broadened signals, the absorption profile is given by the peak-normalised Gaussian lineshape function [19]:

$$\overline{\chi}^{abs}(\nu) = \exp\left[-4\ln 2(\nu-\nu_0)^2/\delta\nu_G^2\right] \qquad \textbf{Equation 3.17}$$

where $\nu_0$ is the centre frequency of the absorption profile and $\delta\nu_G$ is the full width at half maximum (FWHM) of the Doppler broadened absorption profile, given by:

$$\delta\nu_G = \frac{2\nu_0}{c}\sqrt{\frac{2kT\ln 2}{m}} \qquad \textbf{Equation 3.18}$$

where $T$ is the temperature, and $m$ and is the mass of the analyte (in grams per mole).

The corresponding dispersion lineshape for a Gaussian-shaped absorption profile is given by [19]:

$$\overline{\chi}_G^{disp} = -\frac{2}{\sqrt{\pi}}\exp[-\gamma^2]\int_0^{\gamma}\exp[\gamma'^2]\,d\gamma' \qquad \textbf{Equation 3.19}$$

where $\gamma = 2\sqrt{\ln 2}(\nu-\nu_0)/\delta\nu_G$.

Figure 3.11 shows the experimental schematic of the setup to record the fm-NICE-OHMS signals, however its full experimental operating details will be described in the following chapter.

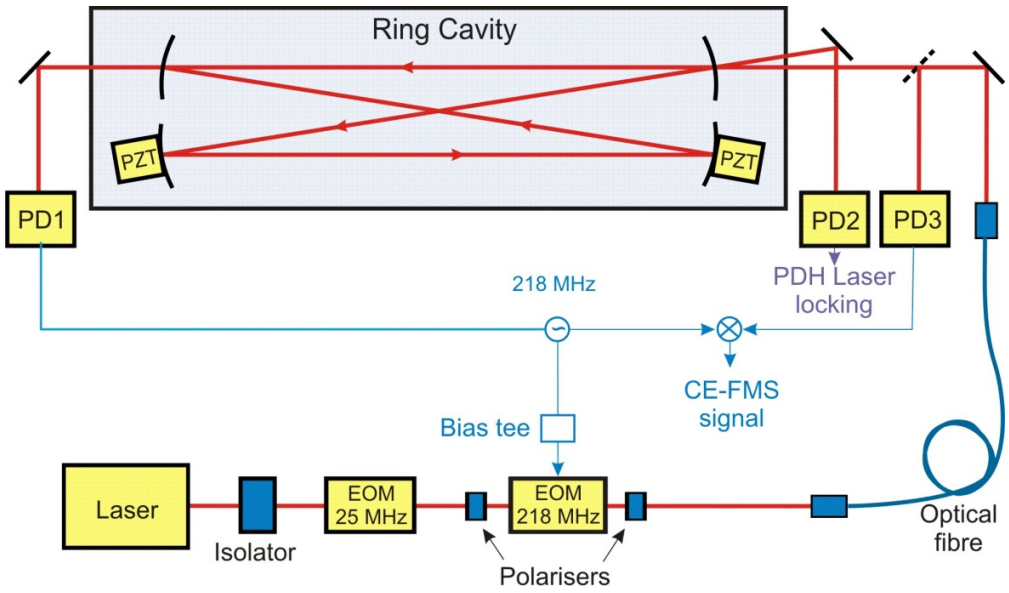


**Figure 3.11 Experimental schematic of the CE-FMS setup. EOM – Electro Optic Modulator, PD – Photo diode and PZT – Piezo Electric Transducer.**

Experimentally, the laser light is modulated at the cavity free spectral range $\omega_m$, with the use of a second EOM. The modulated light interacts with the gas sample within the cavity, and is then detected by a fast photodiode (PD1). The ac signal is then demodulated at $\omega_m$ to produce the *fm*-NICE-OHMS signal. However, there is noise associated with the changes in phase as the frequency modulation is applied to the laser light.

Figure 3.12 shows a typical *fm*-NICE-OHMS spectrum for 1.83 Torr of an un-assigned $CH_4$ transition at 6595.90 $cm^{-1}$, and the associated fit. The returned Gaussian width of the fit was 612 ± 5 MHz which agrees very well with the calculated Doppler width for this transition of 611 MHz. This *fm*-NICE-OHMS signal was acquired by scanning over 5 GHz at a scan rate of 1 Hz.

The signal was acquired with 10 averages over an acquisition time of 10 seconds. The sensitivity calculated for this data $\alpha_{min}$ is 9.6 x $10^{-10}$ $cm^{-1}$, showing an order of magnitude improvement from that reported for the locked-CEAS signal previously. To enable a fair comparison across different absorption techniques, to assess their respective performance and to qualify performance gains from averaging alone, the bandwidth reduced sensitivity ($\alpha_{min}$ *(BW eff)*) can be employed. This is defined as $\alpha_{min}\ (BW\ eff) = \alpha_{min} * \sqrt{\frac{n}{B}}$ where $B$ is the detection bandwidth given by $B = (1 / 2\pi\tau)$, where $\tau$ is the demodulation time constant and $n$ is the number of averages. The corresponding $\alpha_{min}$ *(BW eff)* for *fm*-NICE-OHMS is thus 7.7 x $10^{-10}$ $cm^{-1}$ $Hz^{-1/2}$.

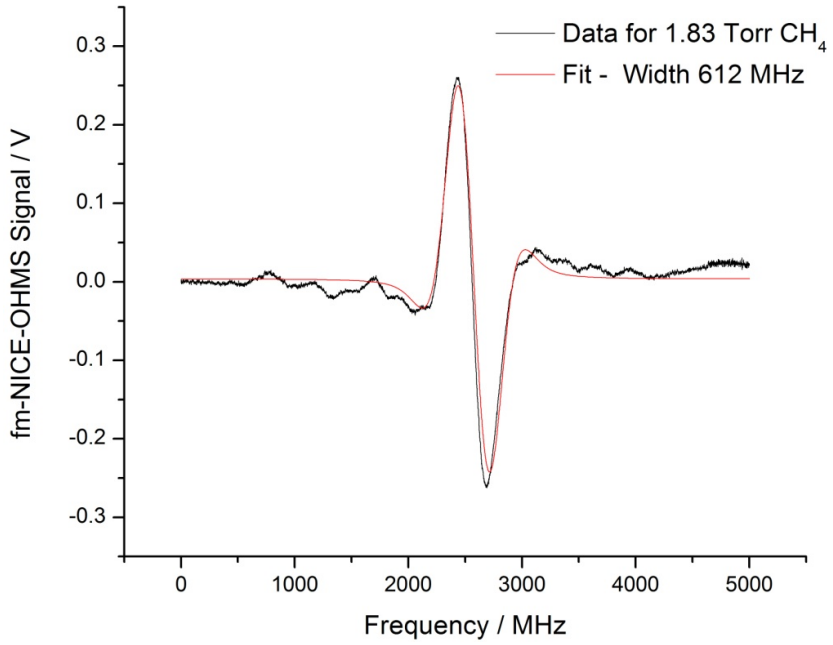


**Figure 3.12 Typical *fm*-NICE-OHMS signal for 1.83 Torr of $CH_4$.**

## 3.4. Wavelength modulation spectroscopy (WMS)

Having presented the theoretical description for *fm*-NICE-OHMS, in order to produce the full NICE-OHMS signal, a further layer of low frequency wavelength modulation is applied to the *fm*-NICE-OHMS signal which aims to effectively remove any residual amplitude noise in the system still present after the FM stage of the experiment. Similar to FMS, WMS reduces background noise sources from a detected signal by modulating the laser radiation with a specific frequency *f*, then demodulating the detected signal at that same applied frequency with the use of a lock-in amplifier. Only signals at the same frequency and phase as that applied to the laser radiation are passed by the lock-in amplifier and output for signal averaging, making an effective filter removing all signals not at the desired modulation/detection frequency.

Detection of the WMS signals can be performed at a multiple of harmonic frequencies *nf*, where *n* is a positive integer. *n* is chosen depending on the requirements of the output signal; 1*f* harmonic detection results in a lineshape which is zero at the transition centre whereas *2f* harmonic detection leads to a symmetric lineshape and is smaller in signal but often a flatter baseline. Both signal intensities are related to the absorption strength of the feature.

### 3.4.1. Theory of WMS

As previously stated, WMS is characterised by a modulation frequency that is smaller than the half-width of the absorption feature. This leads to many side-bands which interact with the absorbing medium. The resulting transmitted electric field is given by:

$$E_T(t) = E_0 \exp(i\omega_0 t) \sum_{n=-\infty}^{+\infty} T(\omega_m) J_n(\beta) \exp(in\omega_m t) \qquad \textbf{Equation 3.20}$$

Assuming a weak absorption, Equation 3.20 give rise to the wavelength modulated signal:

$$\begin{aligned} \left|E_{\omega m}(t)\right|^2 = {} & E_0{}^2 \exp(-2\delta_0) \\ & \times \left[ 1 + 2\cos(\omega_m t) \sum_{n=0}^{\infty} J_n J_{n+1} (\delta_{-n-1} - \delta_{n+1} + \delta_{-n} - \delta_n) \right. \\ & \left. + 2\sin(\omega_m t) \sum_{n=0}^{\infty} J_n J_{n+1} (\phi_{-n-1} - \phi_{-n} + \phi_{n+1} - \phi_n) \right] \end{aligned} \qquad \textbf{Equation 3.21}$$

where the two cos and sin terms relate to the absorption and dispersion terms respectively and where the modulated field has a progression of $n$ sidebands on either side of the carrier frequency separated by integer multiples of $\omega_m$.

At the low modulation frequencies used for WMS the dispersion component will be negligible (as the small sideband separation leads to $\phi_{n+1} - \phi_n \approx 0$) and

the WMS intensity is therefore given solely by the $\cos(\omega_m t)$ absorption component:

$$I_{wm} = 2\sum_{n=0}^{\infty} J_n J_{n+1}(\delta_{-n-1} - \delta_{n+1} + \delta_{-n} - \delta_n) \qquad \textbf{Equation 3.22}$$

This summation converges [14], and assuming a constant absorption difference ($\Delta\delta(\omega_0)$) between the sidebands at frequencies near $\omega_m$ the intensity can be expressed as:

$$I_{wm}(\omega_0) = -2\Delta\delta(\omega_0)\beta = -2\left.\frac{d\delta}{d\omega}\right|_{\omega_0} \beta\omega_m \qquad \textbf{Equation 3.23}$$

The WMS signal is therefore the first derivative of the maximum frequency deviation ($M\omega_m$) from the carrier frequency. However, often the measurements are not performed in the derivative limit resulting in modulation broadening of the WMS signal.

In the theory describing NICE-OHMS it is common to use the Fourier formalism for describing the laser modulation and subsequent demodulation by the lock-in amplifier as any periodic frequency-dependent signal, $S(\omega)$, can be expressed as a Fourier series; this theory is therefore also presented here. Kluczynski *et al* [31] have published an extensive review of the work regarding the Fourier formalism for treating WMS, which is followed here.

When the laser is sinusoidally modulated at a frequency, $\omega_m$, around its central laser frequency, $\omega_L$, the overall instantaneous frequency, $\omega$, of the electric field of the laser is described by:

$$\omega = \omega_L + \omega_a \cos(\omega_m t) \qquad \textbf{Equation 3.24}$$

where $\omega_a$ is the modulation amplitude. Thus Equation 3.24 can be rewritten as:

$$S(\omega) = S^{wm}(\omega_L, \omega_a, t) = \sum_{n=0}^{\infty} S_n^{even}(\omega_L, \omega_a)\cos(\omega_m t) + \sum_{n=1}^{\infty} S_n^{odd}(\omega_L, \omega_a)\sin(\omega_m t) \qquad \textbf{Equation 3.25}$$

where $S_n^{even}(\omega_L, \omega_a)$ and $S_n^{odd}(\omega_L, \omega_a)$ are the $n^{\text{th}}$ even and odd Fourier coefficients of the periodic signal $S^{wm}(\omega_L, \omega_a, t)$. This signal is typically demodulated using a lock-in amplifier, where the $n^{\text{th}}$ harmonic output can be written in terms of the $n^{\text{th}}$ Fourier coefficients of the input signal according to:

$$S^{wm}(\omega_L, \omega_a) = \eta_{wm}\left[ S_n^{even}(\omega_L, \omega_a)\cos(\theta_{\omega_m}) + S_n^{odd}(\omega_L, \omega_a)\sin(\theta_{\omega_m}) \right] \qquad \textbf{Equation 3.26}$$

where $\theta_{wm}$ is the detection phase of the WM detection and $\eta_{wm}$ is the instrumentation factor for WM detection that includes the gain of the lock-in amplifier. When a pure cosine modulation is applied, fulfilling the condition that any out-of-phase residual amplitude modulation is small, the modulated sig-

nal is carried mainly by the even components. Therefore, for close to in-phase detection, for which $|\sin(\theta_{wm})| << |\cos(\theta_{wm})|$, the $n^{th}$ harmonic output from the lock-in amplifier can be described by:

$$S_n^{wm}(\omega_L, \omega_a) = \eta_{wm} S_n^{even}(\omega_L, \omega_a)\cos(\theta_{\omega_m}) \qquad \textbf{Equation 3.27}$$

### 3.4.2. *wm*-NICE-OHMS

Equation 3.16 describes the case where FMS is performed at the free spectral range of the cavity, i.e. the *fm*-NICE-OHMS signal. In order to obtain the full *wm*-NICE-OHMS signal description, the low frequency WMS modulation needs to be included. In *wm*-NICE-OHMS, the resulting demodulated *fm*-NICE-OHMS signal is then fed into a lock-in amplifier for demodulation. The resulting $n^{th}$ harmonic *wm*-NICE-OHMS signal $S_n^{wm-no}$ can then, in line with Equation 3.27, be described by:

$$S_n^{wm-no}(\omega_0, \omega_m, \omega_a, \theta) = \eta_{wm} S_n^{fm-no,even}(\omega_0, \omega_m, \omega_a, \theta) \qquad \textbf{Equation 3.28}$$

where $S_n^{fm-no,even}(\omega_0, \omega_m, \omega_a, \theta)$ is the $n^{th}$ Fourier coefficient of the *fm*-NICE-OHMS signal, given by Equation 3.16. In *wm*-NICE-OHMS, usually the 1*f*-WMS signal is detected and therefore the resulting signal can be described by:

$$
\begin{aligned}
S_1^{wm-no}(\omega_0,\omega_m,\omega_m,\theta) = \eta_{wm}\eta_{fm}\frac{2F}{\pi}J_0(\beta)J_1(\beta)P_0\alpha_p L \\
\times\Big\{\Big[\overline{\chi}_1^{\,abs,even}(\omega_0-\omega_m,\omega_a) \\
-\overline{\chi}_1^{\,abs,even}(\omega_0+\omega_m,\omega_a)\Big]\cos\theta \\
+\Big[\overline{\chi}_1^{\,disp,even}(\omega_0-\omega_m,\omega_a)-2\overline{\chi}_1^{\,disp,even}(\omega_0,\omega_a) \\
+\overline{\chi}_1^{\,disp,even}(\omega_0+\omega_m,\omega_a)\Big]\sin\theta\Big\}
\end{aligned}
\qquad \textbf{Equation 3.29}
$$

where $\overline{\chi}_1^{abs,even}(\omega_0 \pm \omega_m,\omega_a)$, $\overline{\chi}_1^{disp,even}(\omega_0 \pm \omega_m,\omega_a)$ and $\overline{\chi}_1^{disp,even}(\omega_0,\omega_a)$ are the even components of the first-order Fourier coefficients of the peak-normalised absorption line-shape function for the sidebands and the corresponding dispersion line-shape function for the sidebands as well as the carrier, respectively. By setting the FM phase to $\theta = 0$ or $\pi/2$, a pure *wm*-NICE-OHMS absorption signal consisting of the square bracket of the cosine term or a pure *wm*-NICE-OHMS dispersion signal consisting of the square bracket of the sine term can be detected. A schematic diagram showing the experimental setup for the full *wm*-NICE-OHMS technique is shown in Figure 3.13. This setup will be more fully explained in the following chapter.

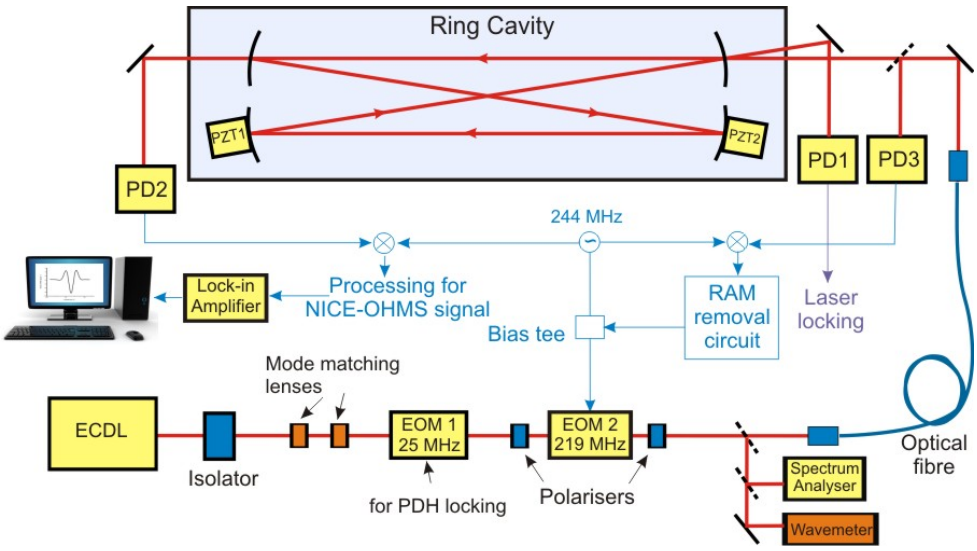


**Figure 3.13 Schematic of the *wm*-NICE-OHMS setup showing the modulating electronics. ECDL – External Cavity Diode Laser, EOM – Electro Optic Modulator, PD – Photo diode and PZT – Piezo Electric Transducer.**

The low frequency modulation provided by the lock-in amplifier is chosen to be 60 Hz, and applied to effect the change to the cavity length via PZT2 and thus the laser via the locking circuit. A typical *wm*-NICE-OHMS trace is shown in Figure 3.14 with the additional layer of modulation improving the sensitivity of the technique to 4.3 x $10^{-10}$ $cm^{-1}$. The corresponding $\alpha_{min}$ *(BW eff)* for *wm*-NICE-OHMS is thus 5.9 x $10^{-10}$ $cm^{-1}$ $Hz^{-1/2}$. This NICE-OHMS signal was acquired by scanning over 4 GHz at a scan rate of 0.3 Hz. The signal was acquired with 6 averages over an acquisition time of 10 seconds.

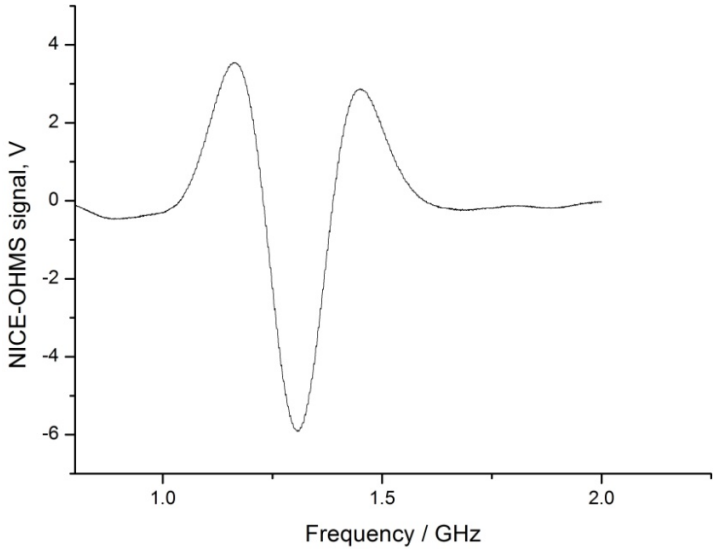


**Figure 3.14 Typical *wm*-NICE-OHMS spectrum of 1.83 Torr $CH_4$ at 6595.90 $cm^{-1}$.**

## 3.5. *wm*-NICE-OHMS Lineshape Simulation

The following description of the theory and simulation relates to the specific experimental conditions for which the experimental data presented later in this thesis was taken. As described in section 3.4.1, the simplest way of obtaining a simulation for a given *wm*-NICE-OHMS signal is to take the first derivative of an *fm*-NICE-OHMS signal. The *fm*-NICE-OHMS absorption signal has been simulated for an unassigned weak overtone transition of methane at 6610.06 $cm^{-1}$ using the equations given in section 3.3.2 for a purely Doppler-broadened absorption profile as shown in Figure 3.15. The modulation frequency was chosen to be 219 MHz (twice the free spectral range of the cavity), with the Gaussian width set at 611 MHz. The result of the first derivative of

this *fm*-NICE-OHMS absorption signal is shown on the green trace of Fig 3.16.

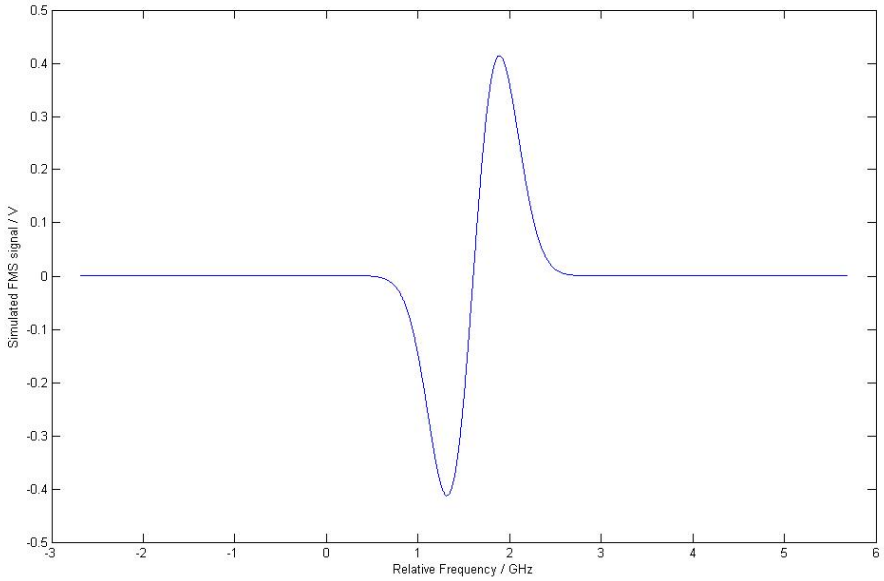


**Figure 3.15 Simulation of an FM spectrum of a methane transition at 6610.063 cm$^{-1}$.**

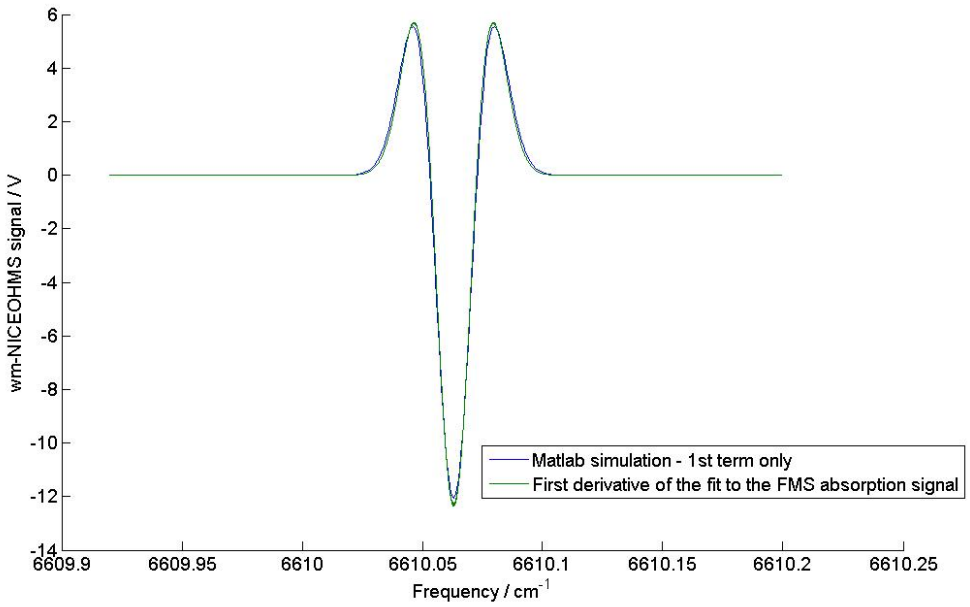


**Figure 3.16 Comparison of a simulation (blue) based on the theoretical wm-NICE-OHMS lineshape, and the first derivative of fm-NICE-OHMS data (Green).**

In order to provide a more comprehensive investigation, simulations of the *wm*-NICE-OHMS signal were undertaken for a phase angle of zero, corresponding to a pure absorption signal. This greatly simplifies Equation 3.29 to involve only the absorption term:

$$S_1^{wm-no}(\omega_0,\omega_m,\omega_m,\theta) = \eta_{wm}\eta_{fm}\frac{2F}{\pi}J_0(M)J_1(M)P_0\alpha_p L \times\left[\bar{\chi}_1^{abs,even}(\omega_0-\omega_m,\omega_a)-\bar{\chi}_1^{abs,even}(\omega_0+\omega_m,\omega_a)\right] \quad \textbf{Equation 3.30}$$

The *wm*-NICE-OHMS signals recorded in this work can be described by a Gaussian lineshape function. The even components of the first-order Fourier coefficient of a wavelength modulated Gaussian lineshape function have been outlined in the analytical work of Kluczynski *et al* [31]. In the case where the normalised modulation amplitude of the wavelength modulation, $\bar{\omega}_a = \omega_a/(\delta\nu_G/2) \ll 1$, only the 1st term of the analytical expression for the even components of the first-order Fourier coefficients of the Gaussian peak-normalised absorption line-shape function is needed and is given by:

$$\bar{\chi}_1^{abs,even}(\bar{\omega}_d,\bar{\omega}_a) = -\bar{\omega}_a\bar{\omega}_d\ln(2)\left[e^{-(\bar{\omega}_d^2)\ln(2)}\right] \quad \textbf{Equation 3.31}$$

where $\bar{\omega}_d = (\omega_0-\omega_L)/(\delta\nu_G/2)$ with $\omega_L$ the centre frequency of the absorption line. The result of the *wm*-NICE-OHMS signal simulated for the same transition is shown in Figure 3.16 as the blue trace. It can be seen that both the first

derivative of the *fm*-NICE-OHMS signal and the first term only solution for the *wm*-NICE-OHMS signal show very good agreement. Further comparison of simulated *wm*-NICE-OHMS signals with experimental data will be discussed in Chapter 4.

## 3.6. Concluding Remarks

In this chapter, the theory has been laid out for the constituent components which, when combined together, enable the generation of full *wm*-NICE-OHMS signals. Although the technique can achieve highly sensitive measurements (see next chapter), it is experimentally complex and demanding. Achieving the initial lock of the laser to the high finesse optical cavity is difficult, due to the necessarily narrow linewidths involved for the cavity. Performing the frequency modulation, whilst maintaining the initial cavity lock is challenging, as is matching and tracking a changing cavity free spectral range with the appropriate modulation frequency.

The following Chapters use the basic theoretical information described here and expand them through the implementation of the NICE-OHMS setup, detailing the experimental setup for characterisation of a range of stable species. The ultra-sensitive nature of the technique is demonstrated with measurements on a range of species in various spectral regions.

## References

[1] M. Mazurenka, A.J. Orr-Ewing, R. Peverall, G.A.D. Ritchie., *Annu. Rep. Prog. Chem., Sect. C*, **101**, 100-142 (2005)
[2] L.S. Ma, J. Ye, P. Dube, J.L. Hall, *Journal of the Optical Society of America B - Optical Physics*, **16**, 2255-2268 (1999)
[3] L. Gianfrani, R. W. Fox, L. Hollberg, *Journal of the Optical Society of America B - Optical Physics*, **16**, 2247–2254 (1999)
[4] J. Ye, L.S. Ma, J.L. Hall, *Journal of the Optical Society of America B - Optical Physics*, **15**, 6–15 (1998)
[5] W. Demtroder, *Laser spectroscopy: Basic concepts and instrumentation, 3rd edition*, Springer-Verlag (2003)
[6] E.I. Moses, C.L. Tang, *Optics Letters*, **1**, 115–117 (1977)
[7] J. Reid, D. Labrie, *Applied Physics B – Photophysics and Laser Chemistry*, **26**, 203–210 (1981)
[8] S. Schilt, L. Thevenaz, P. Robert, *Applied Optics*, **42**, 6728-6738 (2003)
[9] K. Duffin, A.J. McGettrick, W. Johnstone, G. Stewart, D.G. Moodie, *Journal of Lightwave Technology*, 25, 3114-3125 (2007)
[10] A. Karpf, G.N.Rao, *Applied Optics*, **48**, 408-413 (2009)
[11] A. Karpf, G.N.Rao, *Applied Optics*, **49**, 1406-1413 (2010)
[12] A. Hutchinson, *DPhil Thesis*, University of Oxford (2007)
[13] D.S. Bomse, A.C. Stanton, J. A. Silver, *Applied Optics*, **31**, 718-731 (1992)
[14] J.M. Supplee, E. A. Whittaker, W. Lenth, *Applied Optics*, **33**, 6294-6302 (1994)
[15] G.C. Bjorklund, *Optics Letters*, **5**, 15–17 (1980)
[16] N.C. Wong, J.L. Hall, *Journal of the Optical Society of America B - Optical Physics*, **2**, 1527–1533 (1985)
[17] G. Janik, C.B. Carlisle, T.F. Gallagher, *Journal of the Optical Society of America B - Optical Physics*, **3**, 1070–1074 (1986)
[18] J.A. Silver, *Applied Optics*, **31**, 707-717 (1992)
[19] S.W. North, X.S. Zheng, R. Fei, G.E. Hall, *Journal of Chemical Physics*, **104**, 2129-2135 (1996)
[20] G.E. Hall, S.W. North, *Annual Review of Physical Chemistry*, **51**, 243-274 (2000)
[21] G. Friedrichs, *Zeitschrift für Physikalische Chemie-International Journal of Research in Physical Chemistry & Chemical physics*, **222**, 1-30 (2008)
[22] H.A. Kramers, *Nature*, **117**, 775-778 (1926)
[23] R.L. Kronig, *Journal of the Optical Society of America B - Optical Physics*, **12**, 547-556 (1926)
[24] R.V. Pound, *Review of Scientific Instruments*, **17**, 490-505 (1946)
[25] R.W.P. Drever, J.L. Hall, F.V. Kowalski, J. Hough, G.M. Ford, A.J. Munley, H. Ward, *Applied Physics B - Lasers and Optics*, **31**, 97-105 (1983)
[26] J.L. Hall, T.W. Hänsch, *Optics Letters*, **9**, 502-504 (1984)
[27] E.D. Black, *American Journal of Physics*, **69**, 79-87 (2001)
[28] R.W. Fox, C. Oates, L. Hollberg, *Cavity-enhanced Spectroscopies: Experimental Methods in the Physical Sciences*, Vol. 40, Eds. R.D. van Zee and J.P. Looney, Academic Press (2002)
[29] L.S. Rothman D. Jacquemart, A. Barbe, D.C. Benner, M. Birk, L.R. Brown, M.R. Carleer, C. Chackerian Jr., K. Chance, L.H. Coudert, V. Dana, V.M. Devi, J.M. Flaud, R.R. Gamache, A. Goldman, J.M. Hartmann, K.W. Jucks, A.G. Maki, J.Y. Mandin, S.T. Massie, J. Orphal, A. Perrin, C.P. Rinsland, M.A.H. Smith, J. Tennyson, R.N. Tolchenov, R.A. Toth, J. Vander Auwera,

P. Varanasi, and G. Wagner, *Journal of Quantitative Spectroscopy and Radiative Transfer*, **96**, 139–204 (2005)
[30] F.M. Schmidt, A. Foltynowicz, W. Ma, O. Axner, *Journal of the Optical Society of America B - Optical Physics*, **24**,1392-1405 (2007)
[31] P. Kluczynski, J. Gustafsson, A.M. Lindberg, O. Axner, *Spectrochimica Acta Part B - Atomic Spectroscopy*, **56**, 1277–1354 (2001).
[32] A. Foltynowicz, W. Ma, F.M. Schmidt, O. Axner, *Journal of the Optical Society of America B - Optical Physics*, **26**, 1384-1394 (2009)

# Chapter 4
# Characterisation of a diode laser based ring cavity NICE-OHMS spectrometer

## 4.1. Introduction

Following on from the theoretical discussion presented in the previous chapter, this chapter describes the experimental setup in more detail, and then presents the results obtained with the NICE-OHMS spectrometer for a selection of stable species used to characterise and optimise the setup. Relatively few

NICE-OHMS setups are in operation in the world, due to the experimental and technical complexities associated with the technique. A sensitivity of $1x10^{-14}$ $cm^{-1}$ close to the shot noise limit has been demonstrated [1], which involved the use a highly frequency and amplitude stabilised YAG laser source. However, this initial demonstration of the outstanding sensitivity which can be reached with the technique was used to investigate only saturated line shapes. For more practical applications, including molecular spectroscopy and the detection of transient atmospheric species such as $HO_2$ presented here, the particular setup described by [1], would be unfeasible as the source is not tunable over a useful spectral range. Subsequently NICE-OHMS has been used to study both Doppler and pressure broadened lineshapes [2, 3, 4, 5, 6, 7, 8] as well as sub-Doppler spectroscopy, [9, 10, 11, 12] resulting in sensitivities in the $10^{-10}$-$10^{-11}$ $cm^{-1}$ $Hz^{-1/2}$ range. The application of NICE-OHMS to both Doppler and pressure broadened samples, where wavelength scans are performed over 100s of MHz , is limited by fluctuations in the level of residual amplitude modulation (RAM) and the fringes associated with etalons formed between or within optical components [4, 7]. Reflections between the optical cavity mirrors and other optics, such as detectors, fiber surfaces and turning mirrors, and reflections within single optical components, such as electro-optic modulators, fibers, and cavity mirrors, can be difficult to minimise.

In this chapter, the characterisation of an external cavity diode laser based NICE-OMHS spectrometer with the first application of a ring cavity and a residual amplitude modulation (RAM) reduction circuit to improve the sensitivity is presented [13]. An initial demonstration of a method of using a pre-cavity FMS signal to improve the sensitivity of the NICE-OHMS apparatus by the use of a RAM reduction circuit on the pre-cavity laser radiation in conjunction with the modulating EOM is presented. Furthermore, a demonstration of the application of the NICE-OHMS spectrometer for the extraction of spectroscopic information, such as pressure broadening parameters, is presented.

## 4.2. Experimental Details

### 4.2.1. Laser sources and optical cavity configuration

The laser source used in this setup is an External Cavity Diode Laser (ECDL). Only a few NICE-OHMS setups have used an external cavity diode laser (ECDL) [5, 6, 7, 9], primarily because they are more difficult to lock than the very low noise solid state and fiber lasers used in other NICE-OHMS experiments. The ease of locking a typical fiber laser, such as an Erbium Doped Fiber Laser (EDFL), can be offset by the limited scan range of 0.7 nm offered by the system, drastically reducing the number of species and transitions which can

be investigated. In contrast, ECDLs have the advantage that they are relatively cheap, compact, easily tunable and controllable devices, and available over a wide wavelength range (375-420 and 630-1700 nm) allowing the observation of a wide range of molecular species desirable for atmospheric sensing. Development of ECDLs for the telecommunications industry means that their established technology and commercial importance brings the price down and widens the selection of laser sources available, along with the added benefit of being able to scan over 80 nm, compared with a similar EDFL which has a corresponding scan range of typically < 1 nm.

So far in this thesis, the optical cavity mirrors have been arranged in a linear configuration, increasing the ease of alignment. However, the setup outlined here utilises a ring cavity, in a bow-tie configuration. With linear cavities, issues can arise from reflections from cavity mirrors propagating directly back down the beam path and causing etalon effects. Using ring or bow-tie configurations reduces this problem. The initial development of the NICE-OHMS technique was a proof of principle, rather than trace gas sensing, and as such, moving away from linear cavities was not of great importance. In most NICE-OHMS experiments, the spectrometer is used for Doppler-free spectroscopy in which counter propagating beams within a linear cavity are required. This is mainly due to scanning limitations of the laser sources being insufficient to

traverse a broadened transition. In addition, issues can also arise when using some piezo electric transducers at pressures greater than 1 Torr [3], thereby limiting the experiments to sub-Doppler investigations.

### 4.2.2. Experimental setup

Photographs showing the setup in its entirety are shown in Figure 4.1 and Figure 4.2, with a schematic of the experimental setup shown in Figure 4.3. The light source was an external cavity diode laser (ECDL) (Sacher Lasertechnik LION, linewidth < 2 MHz) tunable in the range 1480 – 1540 nm with a maximum output power of 3.2 mW providing a mode-hop free tuning range of 56 GHz using current coupling. The laser light was first directed through an optical isolator to prevent optical feedback.

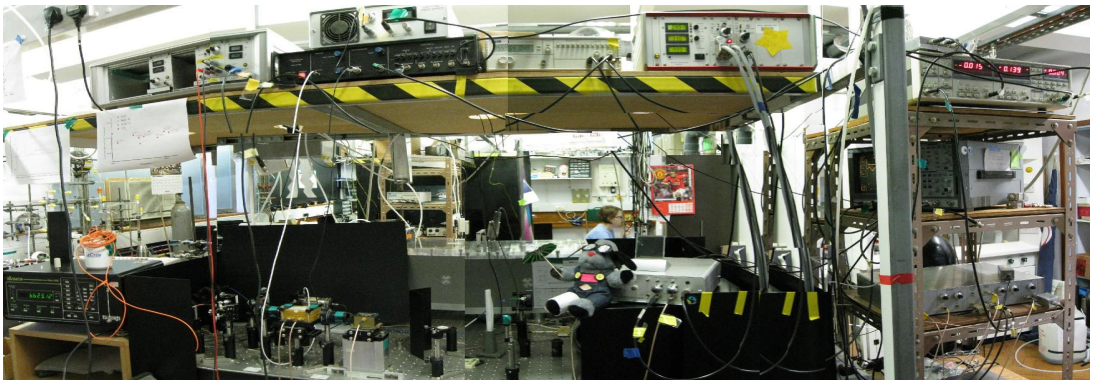

**Figure 4.1 Photograph of the NICE-OHMS experimental setup showing the optical table in the centre, the electronics boxes, lock-in amplifier and oscilloscope on the right and wavemeter on the left.**

Two beam shaping lenses were employed to reshape the elliptical beam output from the laser to a predominantly Gaussian shaped beam, mimicking the

$TEM_{00}$ mode of the cavity. This decoupling enabled modifications to be made to alignments before the cavity without altering the alignment into the cavity. Two electro-optic modulators (EOMs) were situated after the lenses: EOM1 (Nova Phase Electro-Optic Phase Modulator (EO-PM-NR-C3)) to modulate the light for locking of the laser frequency to a $TEM_{00}$ mode of the cavity, and EOM2 (Quantum Technologies (TWAP 10-1350-1650 nm)) for the modulation at the cavity free spectral range and hence post cavity FM detection.

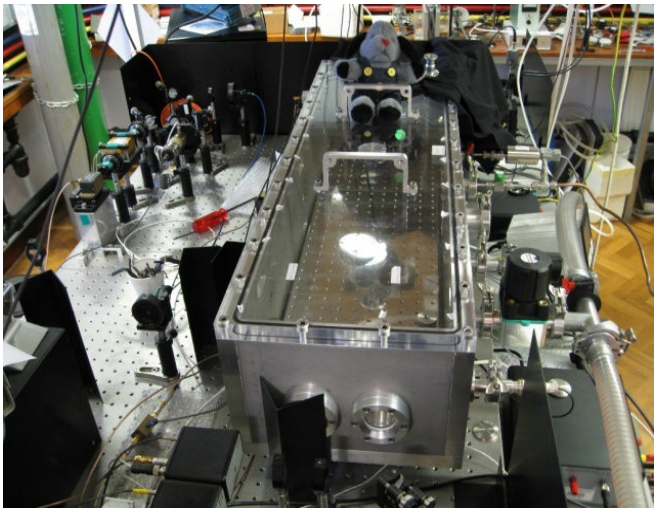

**Figure 4.2 – Photograph showing the metal and Perspex assembly housing the bow-tie optical cavity on the optical table. The gas handling apparatus can be seen on the right of the cavity with the EOMs shown on the far left.**

As well as isolating the alignment of the cavity from adjustments to the laser and EOMs, the light was fed through a single mode polarization preserving fiber (OZ Optics) and to also provide a clean, predominantly Gaussian shaped beam.

The resulting power incident on the cavity was 1 mW. The wavelength of the laser was monitored with a wavemeter (Burleigh WA-1000) and a frequency scale for the data was defined by monitoring the laser output with a spectrum analyser (10 GHz Melles Griot 1300-1500 nm, adjusted for 0.81 GHz).

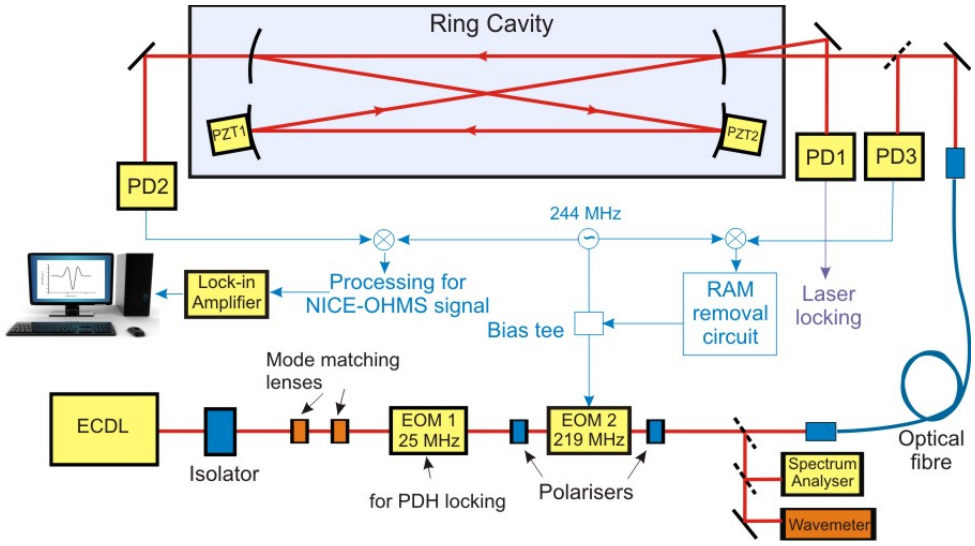


**Figure 4.3 Experimental setup for the NICE-OHMS experiments detailing the ring cavity and a schematic diagram of the RAM circuit and electronics. (ECDL – External Cavity Diode Laser; EOM – Electro-Optical Modulator; PD1, PD2 and PD3 - photodiodes 1, 2 and 3 respectively; PZT1 and PZT2 - piezoelectric transducers).**

The ring cavity was formed by four high reflectivity mirrors (1 inch diameter, radius of curvature of $r$ = -1 m) in a bow tie configuration with a half-round trip, $L$, of 137 cm and a cavity FSR of 109.5 MHz. $L$ is defined as shown in Figure 4.4 below, by the green line.

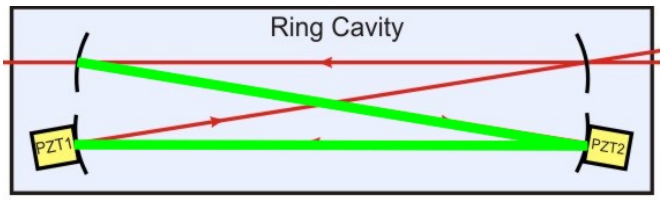


**Figure 4.4 - Schematic diagram showing the definition of *L*, the half round trip length of a bow-tie configuration optical cavity.**

The specified reflectivity of the input and output coupling mirrors was 0.9994 (Newport 10CV00SR.70T), and that of the other two mirrors was 0.9997 (10CV00SR.70F). The two highest reflectivity mirrors were mounted on piezoelectric transducers (PZTs): PZT1 (PiezoMechanik HPSt 150/20-15/55) was used for scanning the cavity length and PZT2 (Physik Instrumente GmbH P-622.10L) was used for the faster modulation of the cavity length for wavelength modulation spectroscopy (WMS). The vacuum chamber housing the ring cavity was evacuated to $10^{-4}$ Torr before it was filled with a given pressure of gas, monitored with a capacitance manometer (MKS instruments 722A11TBA2FA, 0-10 Torr). To avoid etalons, wedged windows (antireflection coated for 1050 to 1600 nm) were used.

The electronics components are numerous and finely tuned to the power and frequency of the laser source and are now discussed. For the locking of the laser frequency to a cavity $TEM_{00}$ mode and the FM frequency to twice the cavity FSR, three linked frequencies were generated by two voltage controlled os-

cillators (VCOs, Mini-Circuits JTOS-300). Signals were generated at 219 (twice the cavity FSR and used for the FSR locking) and 244 MHz and mixed and filtered to produce the 25 MHz difference frequency (used for locking the laser to the cavity). The laser frequency was locked to a $TEM_{00}$ mode of the cavity using the Pound-Drever-Hall (PDH) method [14], with EOM1 used to produce sidebands at ± 25 MHz on the laser frequency. The laser light reflected from the cavity was directed onto a fast photodetector (PD1) (New Focus 1611) and amplified (Mini-Circuits ZFL-500LN), and demodulated at 25 MHz using a double balance mixer (Mini-Circuits ZAD-1) to generate the PDH error signal. This was processed by a fast (MHz) locking circuit with a bandwidth of ~2 MHz, and fed back to the laser injection current for primary locking of the laser frequency to the cavity. With the laser locked to the cavity, the cavity length was changed such that the laser frequency was scanned up to 12 GHz by applying a sinusoidal voltage ramp, at a frequency of 1 Hz, to PZT1. A slow locking circuit followed the change in cavity length and generated a signal which was fed back to the laser PZT input for the ECDL, to maintain the lock of the laser to the cavity whilst scanning the cavity length. The bandwidth of the laser when locked was necessarily better than ~50 kHz. A feed forward loop was implemented in the locking scheme to reduce the load

placed on the locking electronics and increase the scan rate for which mode-hop free tuning of the laser was maintained.

The transmission of the cavity was monitored by a fast photodetector (PD2) (New Focus 1611) with a bandwidth of 1 GHz. The dc output of the detector was recorded in a locked cavity enhanced absorption spectroscopy (CEAS) experiment with a digital oscilloscope (Lecroy 9304) and stored on a computer to determine the cavity finesse, as outlined in Chapter 3. For the determination of the cavity finesse, 8.1 Torr of methane was introduced into the cavity and the methane spectrum for an unassigned $CH_4$ transition at 6595.90 $cm^{-1}$, with a integrated absorption cross section $S$ of 1.115 x $10^{-25}$ $cm^2$ $cm^{-1}$, was recorded with 20 averages. A mean mirror reflectivity $R$ of 0.9988 ± 0.0001, and thus a finesse of 2600 ± 200, was calculated from the integrated area, $A$ of the locked CEAS data using $1\text{-}R = ScL/A$, where $c$ is the concentration in $cm^{-3}$ and $L$ is the half round trip length of the cavity. Repeated measurements of finesse were undertaken to record any mirror degradation over time.

To perform *fm*-NICE-OHMS, EOM2 frequency modulated the laser light at $f_{FM}$ ~219 MHz in order to generate sidebands which are ± 2 FSRs of the cavity for FM detection. However, the FSR of the cavity changes slightly during a frequency scan over an absorption as the length of the cavity changes. The noise-

immune aspect of NICE-OHMS requires a good match between the modulation frequency and FSR of the cavity. To lock the modulation frequency to the FSR the DeVoe and Brewer method [15] was implemented. A fraction of the amplified signal from PD1 was split off (Mini-Circuits ZFSC-2-1-S) and demodulated with a double balance mixer (Mini-Circuits ZAD-1) at 244 MHz (the sum of the cavity FSR and the PDH locking frequency) to produce an error signal for locking the FM frequency to the cavity FSR. This error signal was fed into a proportional-integral locking circuit to adjust the tuning voltage on the VCO and thus the modulation frequency of EOM2 to match twice the free spectral range.

To produce the *fm*-NICE-OHMS signal, the ac output of PD2 was amplified (Mini-Circuits ZKl-1R5 and ZFL500HLN) and high-pass filtered (Mini-Circuits SHP-175), before being demodulated at ~219 MHz with a double balance mixer (Mini-Circuits ZDM-1W-S). This signal was passed through a 100 Hz low-pass filter and recorded using the same oscilloscope and data acquisition system. Changing the demodulation phase allowed either the absorption or dispersion FMS signal to be acquired. In order to select either the absorption or dispersion phases, a network analyser was used. This enabled the phase angle between two signals passed to it to be returned. By selecting the absorption phase as the maximum signal size, the dispersion phase was selected by

selecting a phase 90$^{O}$ away from this, using the network analyser, and fitting both of the acquired signals to verify that $\theta$=0.

Following the generation of the *fm*-NICE-OHMS signal, the detection sensitivity was further improved by applying an additional modulation to the cavity in the form of WMS. The cavity length and, via the locking circuit, the laser frequency, was dithered using PZT2 at a low frequency of 60 Hz with a frequency excursion of 0.1 GHz. To produce this *wm*-NICE-OHMS signal, the *fm*-NICE-OHMS signal was demodulated at 60 Hz using a lock-in amplifier (EG&G 7265 DSP). Demodulation of the signal occurred with a time constant of 50 ms, corresponding to a bandwidth of 3.2 Hz. Again, the processed signals were recorded with the oscilloscope and passed to a computer for analysis.

### 4.2.3. Residual Amplitude Modulation

The maximum sensitivity that could be achieved was limited by residual amplitude modulation (RAM) that results from imperfections in the EOMs and etalons before the cavity, whereby some of the rf applied by the EOM induces amplitude modulation leading to undesirable noise on the detected signal. Etalon effects were minimised with the use of wedged windows, careful alignment of the optical components, and using optical fibers with angled

ends. Assuming that the majority of the cavity etalons have been reduced with the ring cavity arrangement, the remaining etalons are likely to be caused by the optical components before the optical cavity. A simple method of removing a background variation would be to implement a background subtraction technique, whereby the signals are taken both with and without the absorber present in the cavity and then subtracted from one another to remove the background variation. However this is not possible with this NICE-OHMS setup, given the drift in the laser, and the necessity to maintain the laser lock to the cavity over the entire data acquisition period. Taking a background would extend this time to that greater than the time that the laser background variation remained constant and as such would be ineffectual.

In order to remove the RAM, an electronic circuit on the FMS dispersion signal was implemented based on the method described by Wong *et al*. [16]. The RAM on the laser radiation before the cavity was monitored by using a beam splitter to direct 8% of the laser radiation onto the fast photodetector PD3. The ac output of PD3 was amplified (Mini-Circuits ZKl-1R5 and ZFL1000LN), and high-pass filtered (Mini-Circuits SHP-175), before being demodulated at $f_{FM}$ with a double balance mixer (Mini-Circuits ZDM-1W-S). The RAM detected in this way provided an error signal to stabilize the level of RAM prior to the cavity, by using EOM2 to create amplitude modulation (AM) with the oppo-

site sign. For this, two polarisers, with their angle set at 10 degrees from vertical, were positioned at either side of EOM2. The polariser before and the polariser after EOM2 are aligned such that their polarization angles $\beta$ and $\gamma$ relative to the EOM crystal *z* axis (extraordinary axis) are between 10-20° (the angles are not critical as long as they are non zero). They can be used to control the gain of the optical signal and with the associated half wave plate, be used to generate the correct sign for the error signal used for the RAM removal. A bias voltage applied to the EOM produced AM at the same phase as the FMS dispersion signal, and feedback of the processed error signal controlled the RAM level at this phase. By stabilizing the RAM observed before the cavity, a flatter, less noisy baseline on the *fm*-NICE-OHMS dispersion signal can be achieved, thus increasing the sensitivity.

## 4.3. Results and Discussion

In the next sections, observations of a selection of weak transitions of methane, carbon dioxide, and nitrous oxide across 52 $cm^{-1}$ (6595 to 6647 $cm^{-1}$) are presented, demonstrating the broad range of the tunability of the ECDL. Table 4.1 shows the line positions and relative intensities of the transitions in the spectral region of interest, and lists their assignments. Although the methane lines are unassigned, they are very well characterised in terms of intensity and

spectral positions in both HITRAN [17] and the work by Deng *et al* [18]. The transitions will be referred to with reference to their identifier in the table. The spectral region used does have a large concentration of water lines, and so careful consideration was taken to ensure that transitions were selected in narrow water free regions. Initially, measurements have been undertaken for both *fm*-NICE-OHMS and *wm*-NICE-OHMS for a number of transitions, with sensitivity data being recorded for each, in order that the system could be characterised. Following this, a series of more specific measurements were taken in order to obtain spectroscopic information, such as pressure broadening parameters. Further to this, the effect of the implementation of a RAM removal circuit on the reduction/minimisation of any remaining residual amplitude modulation (RAM) noise and the additional increase in the sensitivity of the system is also discussed. In Chapter 3, simulations of the *wm*-NICE-OHMS data were undertaken, in order to test the validity of the theoretical description presented; here the comparisons of these with the actual data obtained are discussed. Finally, a brief discussion on the optimal signal acquisition time of the wm-NICE-OHMS data is presented, followed by a discussion of some limitations to the technique and some general conclusions.

**Table 4.1 Line positions, line strengths and assignments for the species under investigation.**

| Identifier | Species | Position ($cm^{-1}$) | Line strength ($cm^2\ cm^{-1}$) | Assignment |
|---|---|---|---|---|
| **A** | $CH_4$ | 6595.90 | $1.12 \times 10^{-25}$ | Unassigned |
| **B** | $CH_4$ | 6596.10 | $1.45 \times 10^{-25}$ | Unassigned |
| **C** | $CH_4$ | 6610.063 | $7.56 \times 10^{-25}$ | Unassigned |
| **D** | $CO_2$ | 6646.58 | $5.19 \times 10^{-27}$ | P34(e) ($\upsilon_1+\upsilon_2+2\upsilon_3$) |
| **E** | $N_2O$ | 6596.11 | $1.34 \times 10^{-23}$ | R28(e) |

### 4.3.1. Methane results – ultimate sensitivity and noise reduction

Three different transitions of methane, labelled A, B and C are investigated in this section and described in Table 4.1. Figure 4.5 shows typical *fm*- and *wm*-NICE-OHMS spectra for the three transitions, without the RAM removal circuit in operation. As outlined in Chapter 3, the expected line shapes of the WMS signal are the same as those for the first derivative of the FM signal. Figure 4.5 shows the *fm* and *wm*–NICE-OHMS signals obtained from the three transitions, with their respective sensitivities obtained reported in Table 4.2. Also shown on Figure 4.5 (a) is the fit to the *fm*-NICE-OHMS signal where the width returned is 612±11 MHz from a Gaussian fit, whilst the calculated width

for this transition is 611 MHz. This shows good agreement with the theoretical value.

**Table 4.2 Summary of sensitivities obtained for transitions A, B and C**

| Transition of $CH_4$ | Pressure / Torr | *fm*-NICE-OHMS sensitivity / $cm^{-1}$ | *wm*-NICE-OHMS sensitivity / $cm^{-1}$ |
|---|---|---|---|
| A | 1.83 | $9.6 \times 10^{-10}$ | $4.3 \times 10^{-10}$ |
| B | 0.3 | $1.2 \times 10^{-10}$ | $8.2 \times 10^{-11}$ |
| C | 0.5 | $5.2 \times 10^{-9}$ | $2.7 \times 10^{-10}$ |

Although each of these measurements shown in Figure 4.5 demonstrates a good sensitivity, there are still significant background fluctuations and noises evident in the baseline on all of the traces, resulting in the observed variation in sensitivities. In order to try to eliminate these and achieve the best sensitivity possible with the setup, it was necessary to implement the RAM locking circuit, described previously, to reduce unwanted etalon effects and residual noise.

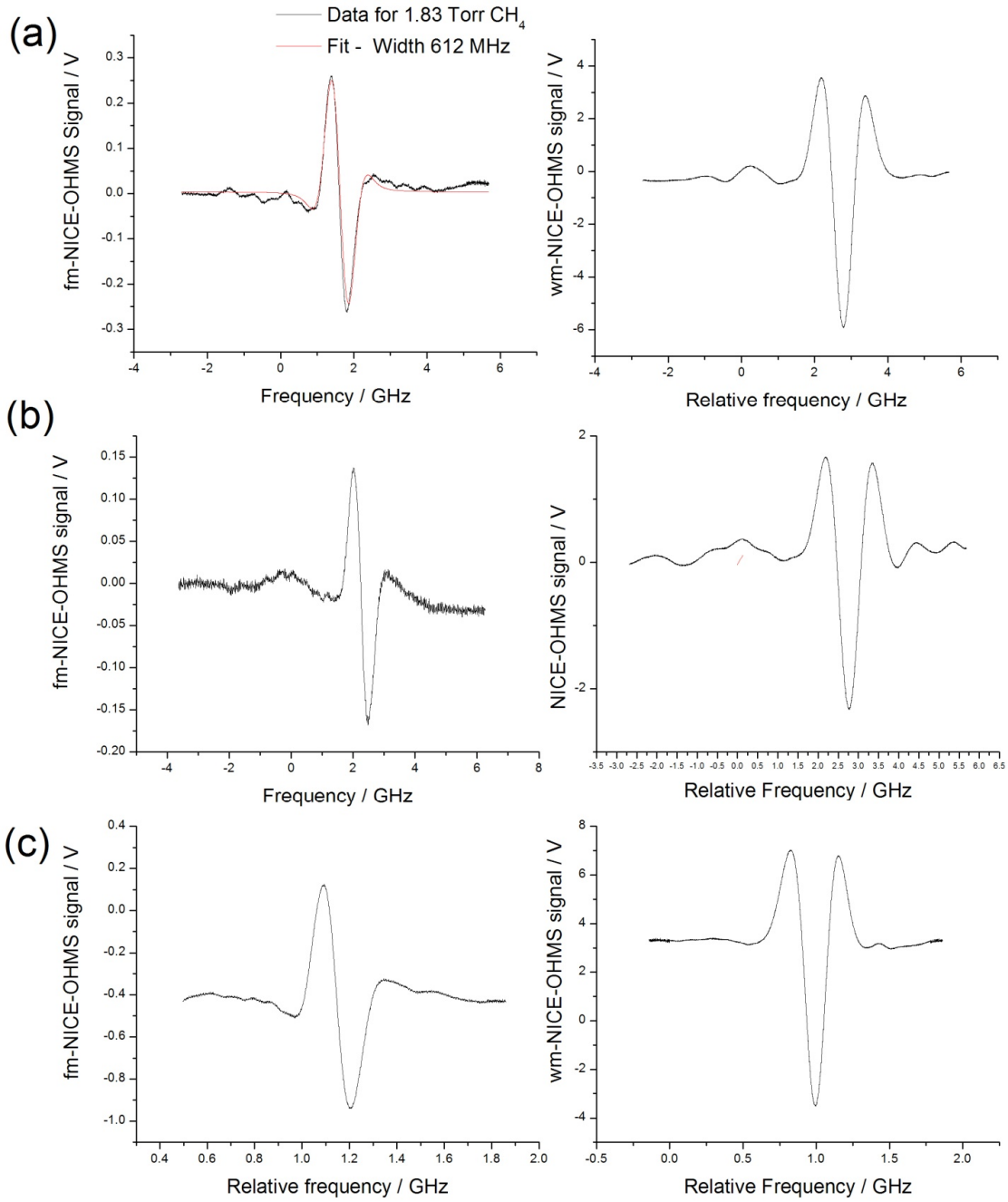


**Figure 4.5 *fm* and *wm*-NICE-OHMS signals for $CH_4$ transitions A, B and C.**

### 4.3.2. RAM Removal circuit

To illustrate the effect of the RAM reduction circuit on the *fm*-NICE-OHMS dispersion signal, a spectrum of 0.2 Torr of $CH_4$, probing transition C [17, 18] was recorded. The RAM reduction circuit works only the dispersion phase of *fm* and *wm* NICE-OHMS signals as it is necessary to match the phases of both the signal and the reference phase. The resulting dispersion signals with the RAM reduction circuit on or off are presented in Figure 4.6. The data have not been offset in the y-direction, the offset of 0.58 V is that induced by the implementation of the RAM removal circuit. The signal-to-noise (S/N) ratio with the RAM circuit off is 85 (where the noise is defined as the standard deviation of the noise on the baseline). When the RAM reduction circuit is in operation, a noticeable reduction in noise on the dispersion signal can be observed and the S/N ratio improves to 177. This demonstrates the usefulness and benefits of the RAM reduction circuit as noise which is present on the *fm*-NICE-OHMS signal would be carried forward in the *wm*-NICE-OHMS signal. The effect of the RAM circuit improves the S/N ratio to an even greater extent when operating the ECDL at different wavelengths where etalons and noise sources are more significant, thus varying its efficacy.

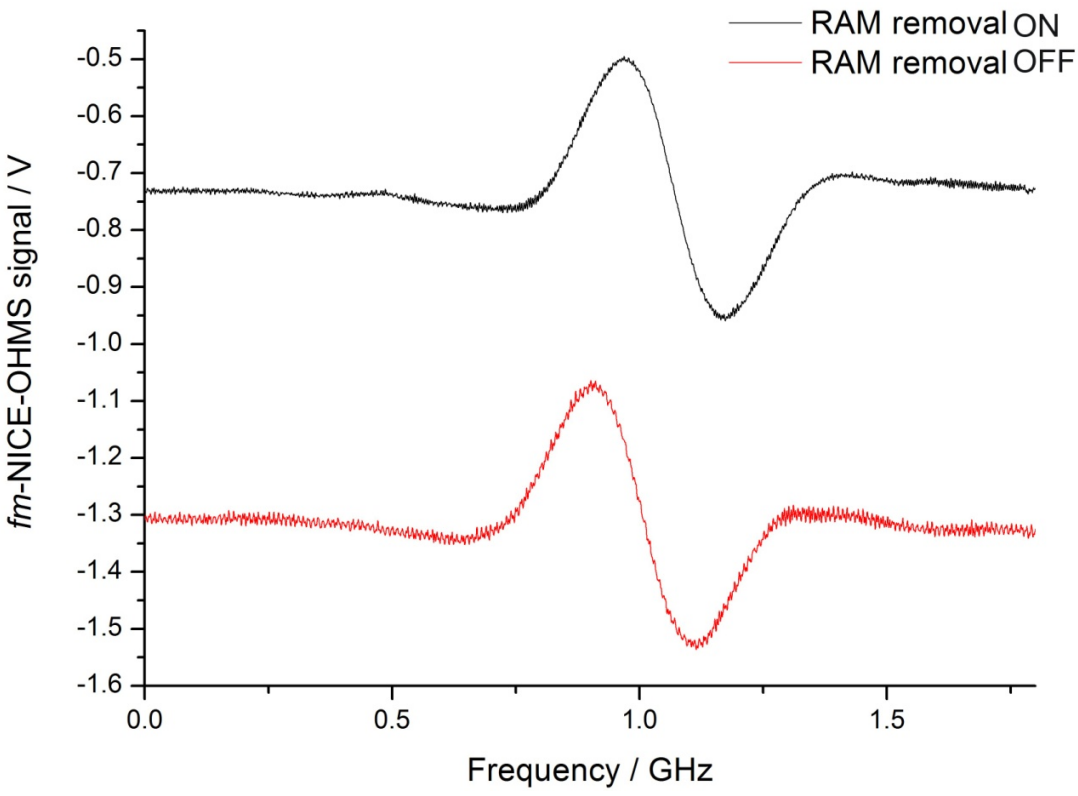


**Figure 4.6 Demonstration of fm-NICE-OHMS signals on transition C with RAM removal circuit off and on.**

From the measurements, it was concluded that the RAM locking circuit was more effective where the noise level was larger.

It is noted that despite the RAM reduction circuit an offset in the baseline signal is observed. This offset is relatively stable during the measuring period, evident in the 0.5 V offset shown in Figure 4.6 and is a result of an equipment based limitation in the range of our feedback to the EOM. To overcome this, an offset voltage is added to the error signal to stabilize the RAM to a non-zero

value; any further persistent offset may arise from changes in laser characteristics across a scan.

### 4.3.3. Ultimate sensitivity measurements

Having demonstrated the benefits of the RAM reduction circuit in operation, the first results of the technique using full *wm*-NICE-OHMS with both a ring cavity and a RAM reduction circuit are presented. Figure 4.7 shows the *wm*-NICE-OHMS signal for 0.04 Torr of $CH_4$ recorded for the transition C. This NICE-OHMS signal was acquired by scanning over 4.5 GHz at a scan rate of 0.26 Hz. The signal was acquired with 6 averages over an acquisition time of 10 seconds. As will be discussed in a later section, this was the optimal acquisition time to improve the S/N ratio without being limited by longer term laser drift problems. The S/N ratio of the signal is ~ 1600 which gives a minimum detectable absorption (under optimal conditions) of $4 \times 10^{-11}$ $cm^{-1}$ $Hz^{-1/2}$, highlighting significant improvements over the typical *fm*-NICE-OHMS sensitivities obtained with this instrument of ~ $2 \times 10^{-10}$ $cm^{-1}$ $Hz^{-1/2}$.

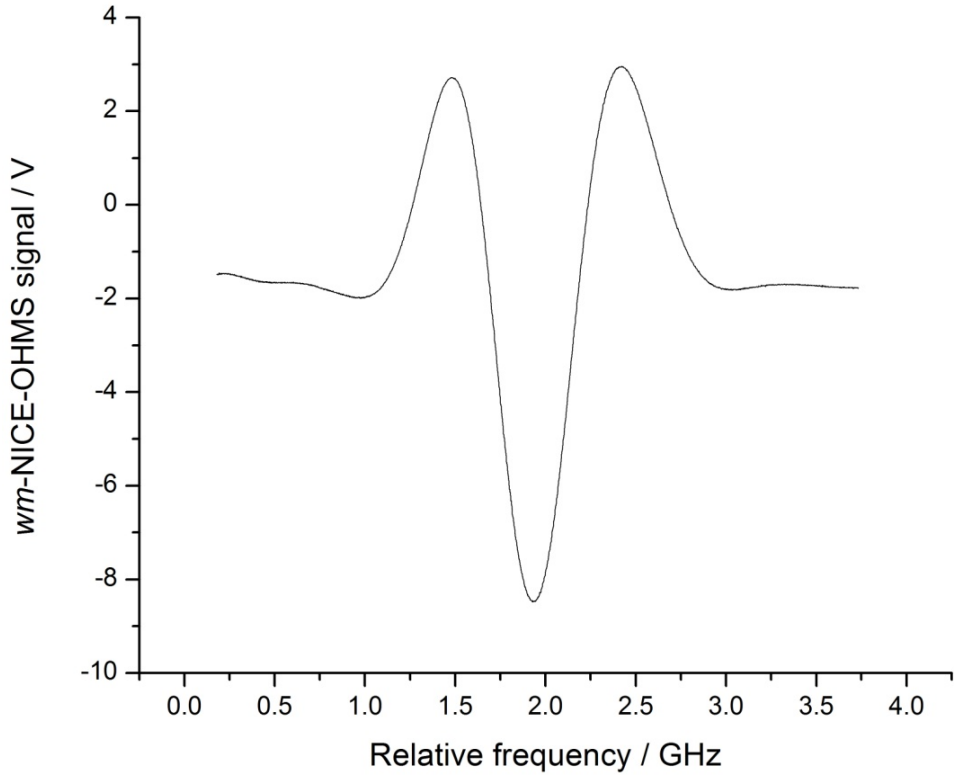


**Figure 4.7 *wm*-NICE-OHMS signal on 0.04 Torr of $CH_4$ for transition C.**

The theoretical minimum detectable absorption [19] (i.e. the shot-noise limit) of the *wm*-NICE-OHMS setup is given by

$$(\alpha L)_{\min} = \frac{\pi}{2F}\left(\frac{2eB}{\eta P_0}\right)^{1/2} \frac{\sqrt{2}}{J_0(\beta)J_1(\beta)}, \qquad \textbf{Equation 4.1}$$

where $F$ is the cavity finesse, $L$ is the cavity length $e$ is the electron charge, $B$ is the detection bandwidth, $\eta$ is the responsivity of the photodetector in A/W, and $P_0$ is the power incident on the photodetector in the absence of absorbing media, $J_n(\beta)$ are the n$^{th}$-order Bessel functions and $\beta$ is the modulation index. Here, $B$ = 3.2 Hz, $\eta$ = 1 A/W, $F$ = 2600, $P_0$ ~ 0.3 mW, $\beta$ = 0.55, which for a cavity

of length 137cm, gives a minimum detectable absorption corresponding to $\alpha_{min}$ = 1.6 x $10^{-12}$ $cm^{-1}$ $Hz^{-1/2}$. Thus the sensitivity reported here is a factor 25 above the shot-noise limit. The remaining residual signals are composed of random background fluctuations which vary on a day to day basis, so they are onerous to eliminate entirely.

### 4.3.4. Simulations

As described earlier in this thesis and shown in Chapter 3, theoretical descriptions of the signals expected from the NICE-OHMS experiment can be used to generate simulations of the expected lineshapes.

Figure 4.8 shows the results of the simulations of the first term only from the analytical work outlined by Kluczynski *et al* [20], along with experimental *wm*-NICE-OHMS data collected on transition C of $CH_4$, shown in Figure 4.7. As the data were taken in the regime where the modulation amplitude, $\omega_a$, was <<1, only the first term was included. As can be seen from the figure, the experimental data agrees reasonably well with the simulated data, with the width of the feature showing particularly good agreement.

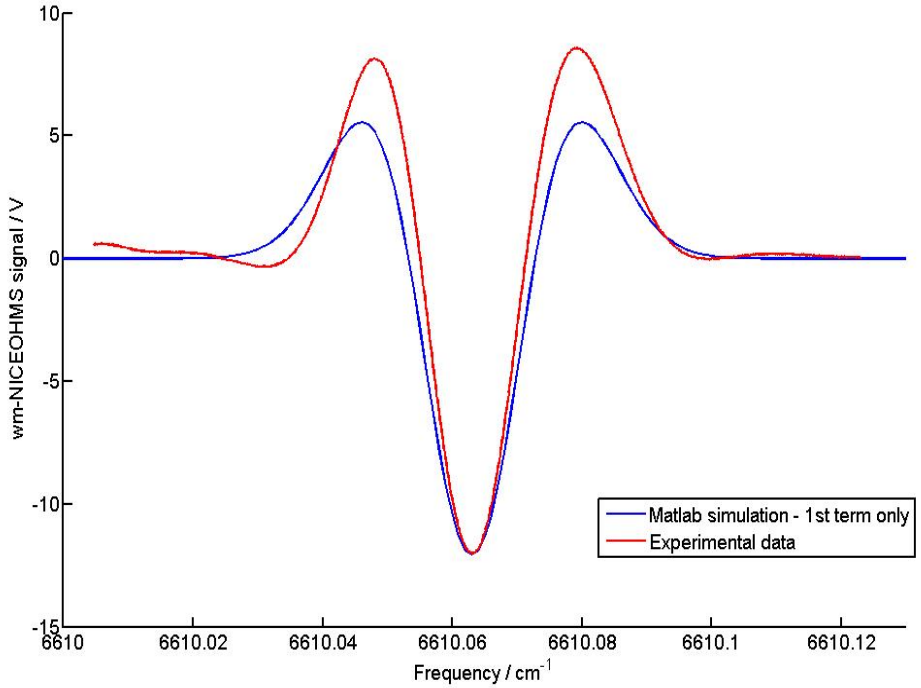


**Figure 4.8 Comparison of simulation of wm-NICE-OHMS data with experimental data, from Figure 4.4.**

Although the width of the absorption feature is reasonably well represented by the simulation, the amplitude of the signal is not as well represented. As described in the previous section, although the NICE-OHMS technique implements complex and extensive measures to eliminate noise sources, there still remain residual noise sources arising from the complex modulation. This may manifest itself as varying amplifications, non-zero offsets and asymmetries in the recorded data, thus explaining why the height of the signal does not quantitatively match the simulations.

### 4.3.5. Investigation into optimal averaging for data acquisition

In order to obtain the optimal number of averages to use when collecting NICE-OHMS data, an analysis of variation in the signal to noise level of the data with varying averaging time was undertaken. Considering the nature of the data acquisition procedure, a more quantitative analysis, such as that provided by an Allan Variance is not especially pertinent. An analysis of how the signal to noise ratio varies as the number of averages for data acquisition is increased was undertaken, with the results shown in Figure 4.9.

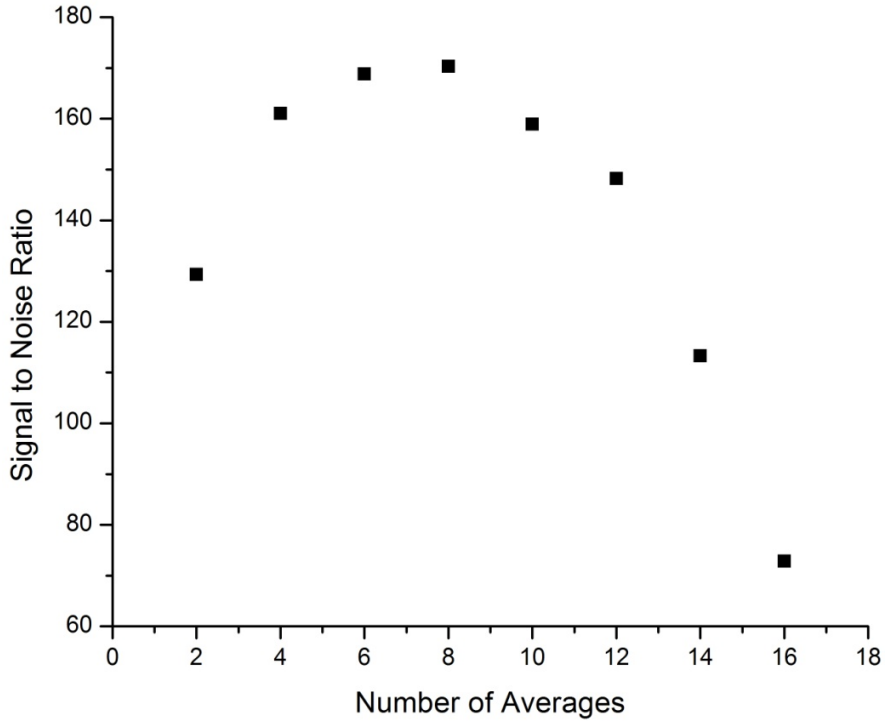


**Figure 4.9 Signal to noise versus number of averages variance plot for *wm*-NICE-OHMS data.**

As can be seen Figure 4.9, initially the signal to noise ratio roughly the expected trend ($N^{1/2}$ where N is number of averages), with the S/N ratio improving as the number of averages is increased. However, following a maximum at 8 averages, the S/N ratio decreases, due to the failure of the cavity locking as the time increases. This provides useful information to guide the data acquisition procedure for the *wm*-NICE-OHMS setup. In order to best represent a measure of both the high and low frequency noise on the baseline, a large section of the baseline was fit to a $2^{nd}$ order polynomial, with one standard deviation of the noise taken to be used in the signal to noise ratio. A typical example is shown in Figure 4.10, where data was taken for 0.07 Torr of $CH_4$, transition B, with 14 averages. From Figure 4.9, it can be seen that the signal to noise ratio reaches already a maximum between 6 and 8 averages. Owing to the difficulty in maintaining the lock over a long period of time, and meeting the requirement that all of the data points were acquired during the same locking period of the laser to the cavity, the maximum number of averages possible was 16.

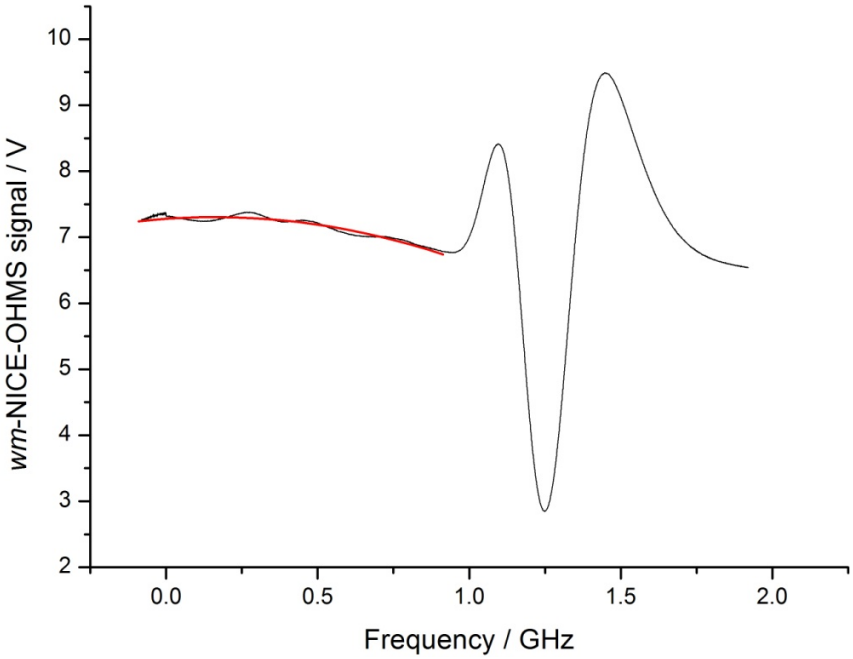


**Figure 4.10 Typical trace shown for 14 averages of transition B of $CH_4$ used in the analysis, the red line shows the fit.**

However, the data indicate that any further large increase in the acquisition time period and the number of averages does not result in an increase in the sensitivity of the data retrieved. Thus, to maximise the sensitivity achieved when averaging, 6 averages was decided upon as the optimal length of time. This relatively short averaging period, restricted by the stability of the lock, is seen in other similar NICE-OHMS setups, such as Axner *et al*, [21] where 10 averages are taken over an acquisition time of around 12 seconds.

## 4.4. Comparison with other work

Table 4.3 shows a brief comparison of the properties of the few other NICE-OHMS setups around the world. The highest sensitivity ever achieved using the NICE-OHMS technique, was obtained by Ye *et al* [19] with the use of a powerful YAG laser with low intrinsic noise. The use of a highly stabilised EDFL, as demonstrated by the work of the Axner group, optimises the ease of locking the laser to the cavity, and having a powerful stable source is also beneficial when attempting to maximise the sensitivity obtained.

**Table 4.3 Comparison of various NICE-OHMS setups highlighting finesse, laser source and sensitivity. (* indicates the power level incident on the photodetector *after* the cavity)**

| Detection Sensitivity $\alpha_{min}$ (cm$^{-1}$) | Laser Type | Finesse | Species | Power (mW) (incident on the cavity) | Group |
|---|---|---|---|---|---|
| **1 x 10$^{-14}$** | Nd:YAG | 100 000 | $C_2HD$ | 75 | Hall, Ye and Ma *et al.* [1] |
| **2 x 10$^{-11}$** | Ti:sapphire | 16 400 | $^{13}C_2H_2$ | - | Silva [22] |
| **4 x 10$^{-11}$** | ECDL | 2600 | $CH_4$ | 1 | This thesis |
| **9.7 x 10$^{-11}$** | QCL | 2415 | $N_2O$ | 0.10* | Taubman *et al* [10] |
| **8 x 10$^{-11}$** | EDFL | 4800 | $C_2H_2$ | 0.64 | Axner *et al* [12] |
| **9.5 x 10$^{-11}$** | ECDL | 300 | $CH_4$ | 1 | Ishibashi *et al* [9] |
| **8 x 10$^{-10}$** | ECDL | 11 000 | $O_2$ | 0.12* | van Leeuwen *et al* [7] |
| **2 x 10$^{-10}$** | DFB | 460 | $C_2H_2$ | 0.96 | Axner *et al* [23] |

However, when using very highly stabilised sources such as YAG lasers or EDFLs, the tuning range they are able to work over is very restricted, limiting their use to the study of just one or two transitions. It can be seen that the sensitivity reported for the Oxford NICE-OHMS setup compares very favourably with other setups, especially in view of the low finesse of the cavity, and the type of laser source used in the experiment proving to be the most sensitive detection instrument of its type (ECDL – External Cavity Diode Laser). Further comparisons of the current setup with other setups operating with different laser sources also compare favourably, especially considering the improvements gained by utilising a clean $TEM_{00}$ mode output through the use of commercial Ti:sapphire laser or an erbium-doped fiber laser (EDFL). The setup presented in this work has demonstrated, using a relatively cheap, widely available telecommunications diode laser (with a much greater tuning range), an impressive sensitivity of $4 \times 10^{-11}$ $cm^{-1}$ $Hz^{-1/2}$, whilst opening up the potential for investigations across a broader range of spectral regions.

## 4.5. Applications of the NICE-OHMS technique

To analyse the performance of the spectrometer over a broad wavelength range, and to demonstrate that the technique is capable of measuring spectral

parameters, the following section details observations on $CO_2$ measurements and the measurement of pressure broadening parameters.

### 4.5.1. Broad wavelength tunability – $CO_2$ detection

Figure 4.11 shows *fm*- and *wm*-NICE-OHMS signals for transition D of $CO_2$ (in Table 4.1) with the highest sensitivity achieved with this measurement being 2 x $10^{-10}$ $cm^{-1}$, taken without the RAM removal circuit being in operation. Additionally, it should be emphasised that the position of the $CO_2$ transition is 40 $cm^{-1}$ away from the spectral position where the $CH_4$ data were taken, and the response of the laser is not the same across the broad spectral region, so the different locking response of the laser, or the varying amplitude modulation associated with the particular region, displays a different level of noise response, manifesting itself in the signal as increased noise. It was noted that the highest sensitivities achieved with the system occurs in the spectral region around 6596 $cm^{-1}$, for which the system was initially designed and optimised.

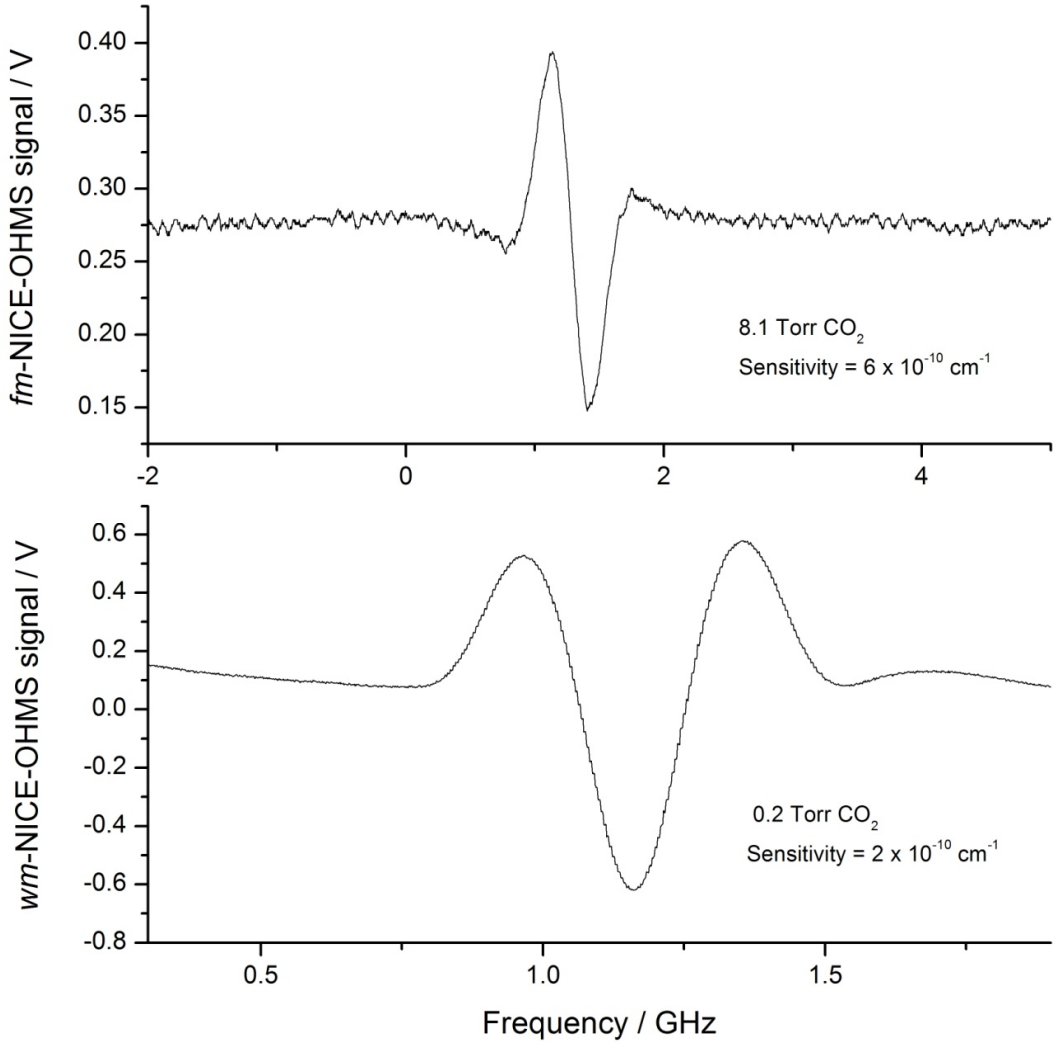


**Figure 4.11 *fm*- and *wm*-NICE-OHMS signals for $CO_2$ transition D.**

From measurements across the tuning range of the laser, it is clear that optimising the electronics at each spectral region is particularly important and can markedly improve the sensitivity attained, yet this is time consuming and often not possible when designing a field instrument for practical application. However, despite this variation in sensitivity across wavelength regions, we note that the ability to apply NICE-OHMS to various transitions across differ-

ent portions of the spectrum whilst still achieving sensitivities of around $10^{-10}$ $cm^{-1}$, is of great benefit when designing a spectrometer which can meet a wide range of detection requirements.

In order to verify the linearity of the technique with increasing pressure, the relationship between the height of the absorption feature and the pressure of added gas was recorded, for both the *fm*-NICE-OHMS signals and *wm*-NICE-OHMS signals, with increasing pressures of $CO_2$. The signal amplitudes for transition D (a typical case being shown in Figure 4.11) were plotted against pressure. In both cases this increased linearly with increasing pressure of gas, with the results being shown in Figure 4.12. The non zero origin intercept gives an indication of the noise inherent in the measurements.

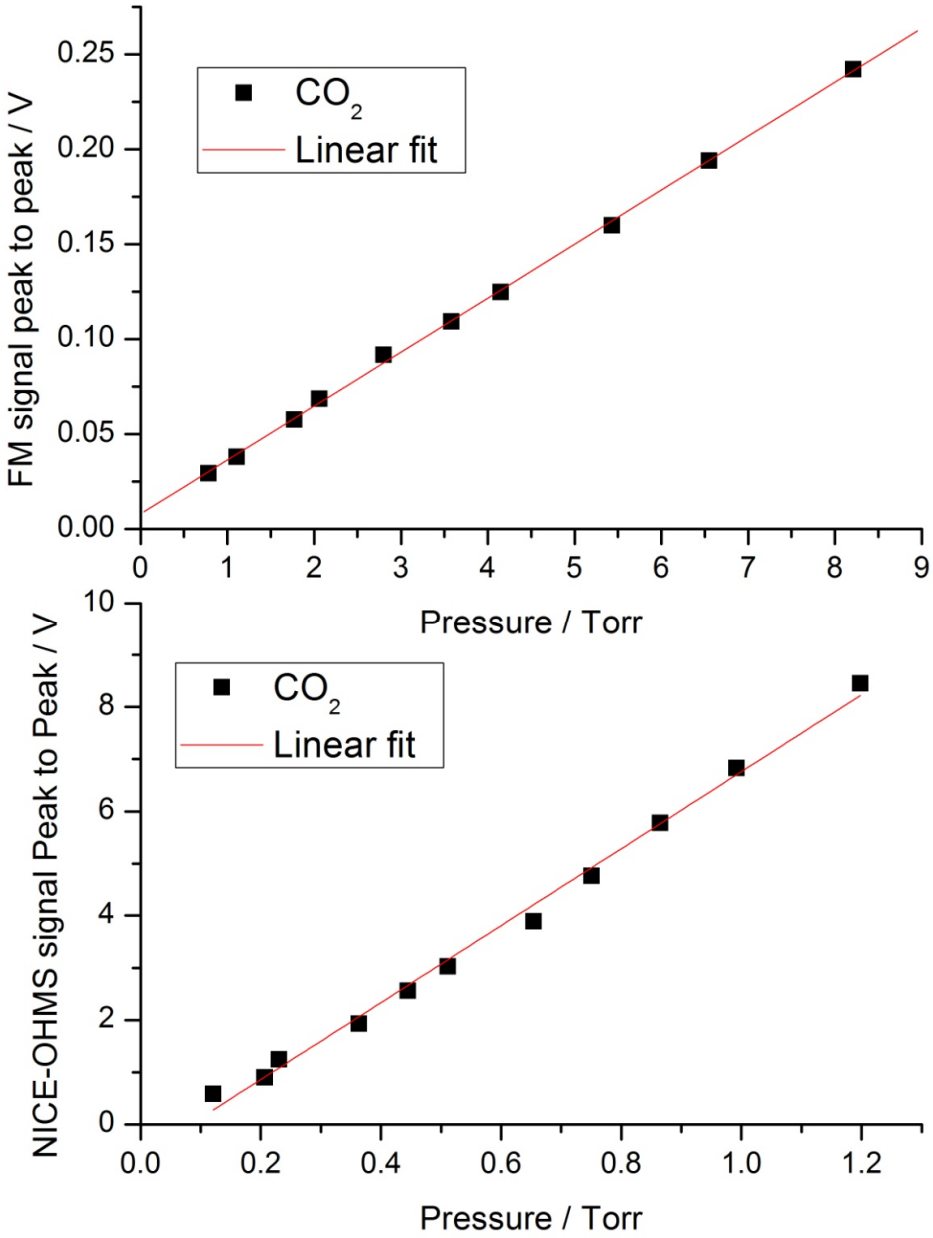


**Figure 4.12 Plots of signal height against pressure of added $CO_2$ gas for *fm*-NICE-OHMS (upper) and wm-NICE-OHMS (lower).**

### 4.5.2. Pressure Broadening

Following the verification of the linearity of both the *fm* and *wm* techniques, *fm*-NICE-OHMS was used to determine pressure broadening coefficients for transition C of $CH_4$ broadened by helium to demonstrate the effectiveness of retrieving transition specific information using the NICE-OHMS technique. 25 Torr of methane was added to the evacuated cavity, following which, increasing amounts of helium gas were added, from 2 to 300 Torr. At each pressure, *fm*-NICE-OHMS data were taken at both the absorption and dispersion phases.

The FM data were fitted using a Voigt profile (a convolution of a Gaussian and Lorentzian component), fixing the FWHM of the Gaussian component of the fit to the theoretical value of 611 MHz and allowing the FWHM of the Lorentzian component of the fit to vary. From this fitting routine, the Lorentzian width of each absorption profile and the central frequency were obtained. As demonstrated by the typical trace showing the data (black line) and fit (red line) shown on Figure 4.13, fitting for the absorption (upper) and dispersion phase (lower) for 25 Torr of $CH_4$ broadened by 150 Torr of helium were well represented by the Voigt profiles transformed into FM space. During the data acquisition routine, only one phase of the data (absorption or dispersion) can

be acquired per scan, with the operator selecting the phase by varying the phase angle, $\theta$. Hence, for the data taken here, at each pressure, both the absorption and dispersion signals were acquired separately, but during the same lock. The time delay between each pair of measurements was around 20 seconds.

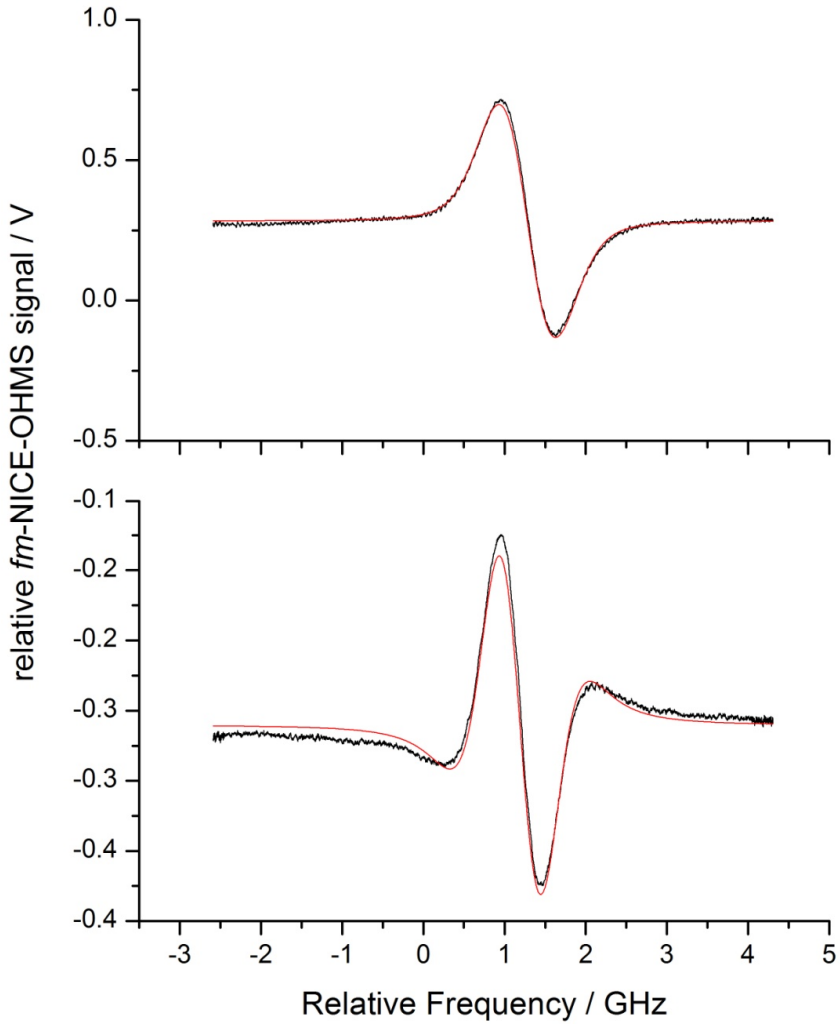


**Figure 4.13 Simultaneous fitting for the absorption (upper) and dispersion phase (lower) for 25 Torr of $CH_4$ broadened by 150 Torr of helium.**

Figure 4.14 shows the plot of the Lorentzian component of each fit against pressure, with a straight line fitted to the points. From the graph, a pressure broadening coefficient of 1.5 ± 0.1 MHz Torr$^{-1}$ (HWHM) is obtained, which corresponds well with the literature values of 1.3-1.7 MHz Torr$^{-1}$ [24] for variation with the $2\nu_3$ band of methane at 1.65 μm.

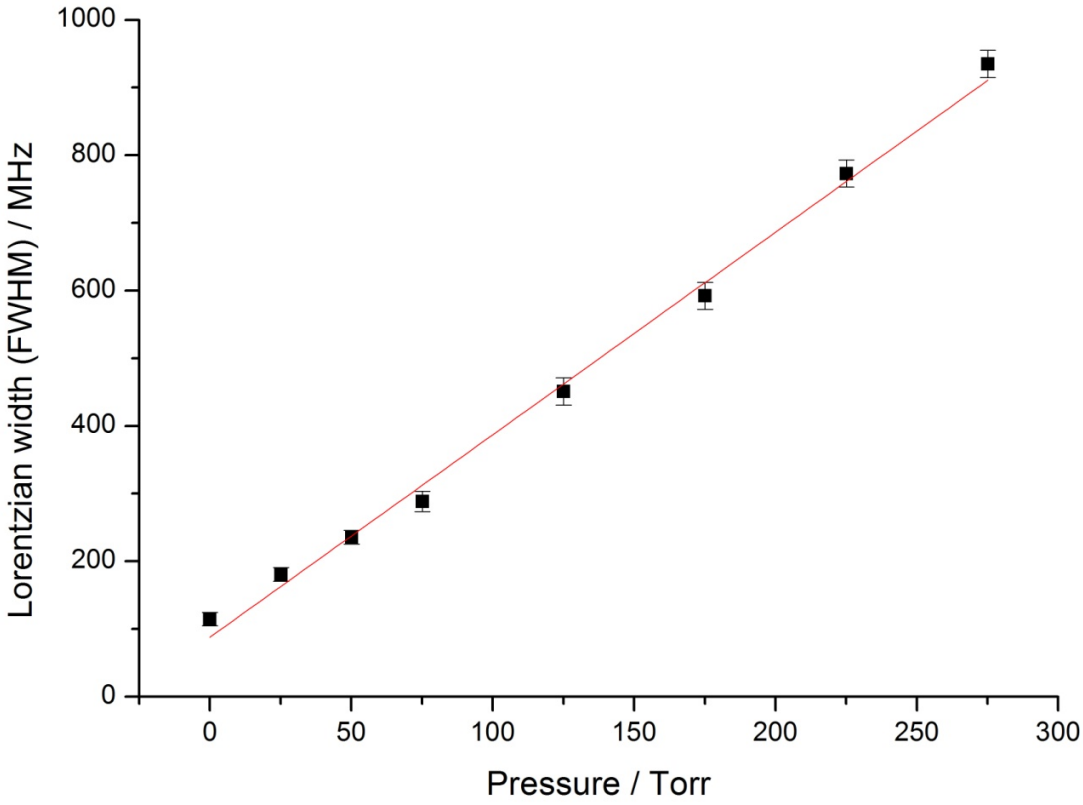


**Figure 4.14 The Lorentzian FWHM as a function of pressure for 25 Torr of $CH_4$ broadened by He.**

Figure 4.14 shows an offset on the y-axis of 87 ± 10 MHz which corresponds to the expected self broadened contribution of $CH_4$ of 85 MHz [17, 18].

A similar procedure was undertaken to retrieve pressure broadening coefficients of $N_2O$ broadened by the addition of helium.

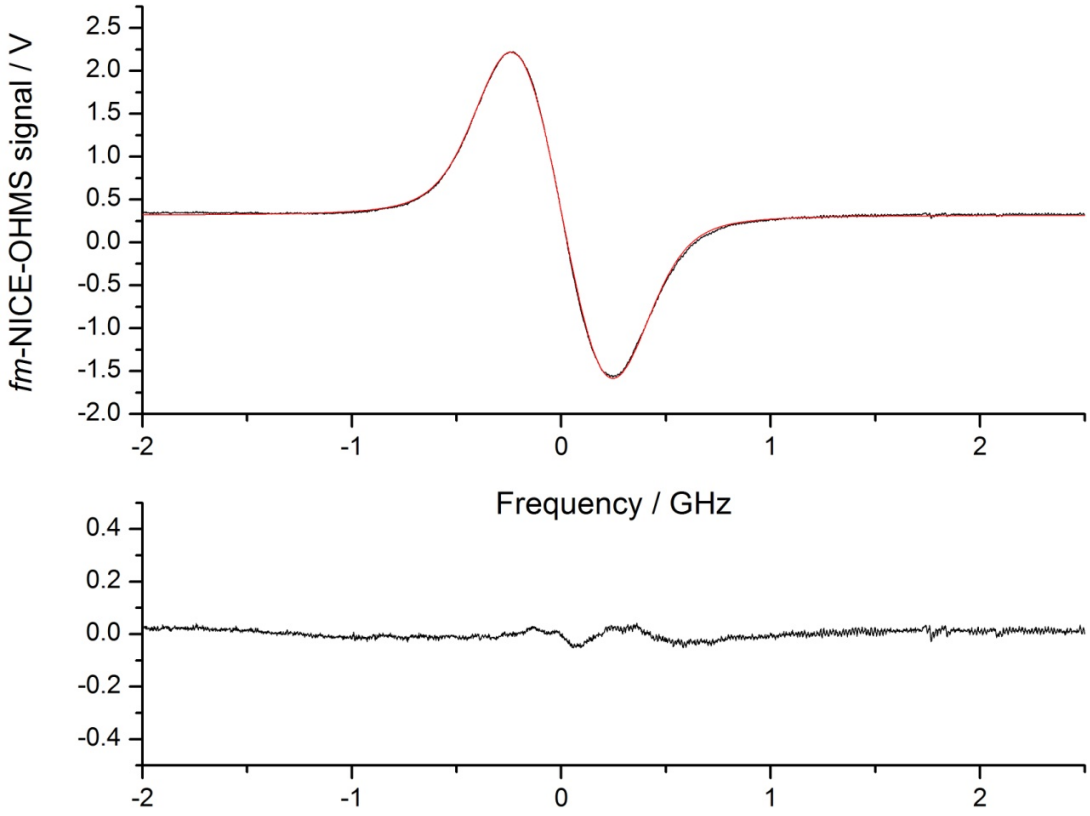


**Figure 4.15 Typical absorption *fm*-NICE-OHMS signal of 0.42 Torr of $N_2O$, with a fit to the data returning a Doppler width of 370 MHz and associated residuals plot.**

Figure 4.15 shows the *fm*-NICE-OHMS absorption signal (black) with the corresponding fit (red) for 0.42 Torr of $N_2O$ centred on transition E. Again, each absorption based *fm*-NICE-OHMS trace was fitted with the Gaussian width fixed to the calculated value of 366 MHz with the Lorentzian component of the Voigt profile being allowed to vary. Figure 4.16 shows the plot of the Lorentzian component of each fit against pressure, with a straight line fitted to the

points. From the graph, a pressure broadening coefficient of 4.4 ± 0.2 MHz $Torr^{-1}$ is obtained, which is in reasonable agreement with the literature values, where Nakayama *et al* [25] reported broadening coefficients of 5.5 MHz $Torr^{-1}$ for work carried out on transitions in the same $\upsilon_3$ band.

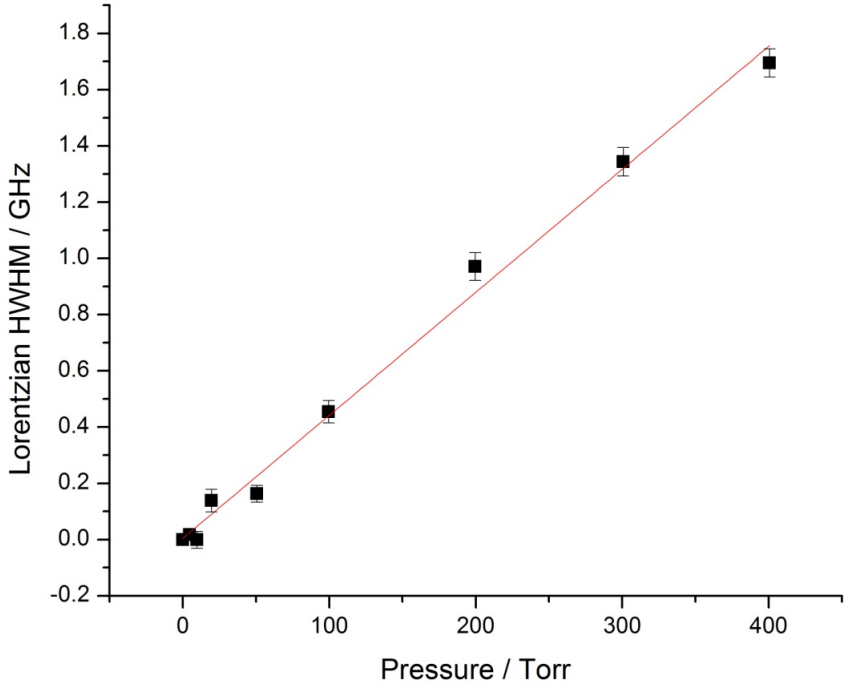


**Figure 4.16 The Lorentzian HWHM as a function of pressure for 0.42 Torr of $N_2O$ broadened by He.**

The work of Nakayama *et al* investigated transitions around 6578 $cm^{-1}$ in the P branch (up to 10(e)), whereas the current transition under investigation in this work is located at 6596 $cm^{-1}$, in the R branch (28(e)). However, it is often the case that the pressure broadening coefficient decreases with increasing values of J (see for example Chapter 2). Furthermore, the significant differences re-

ported in the HITRAN database in the air broadening coefficients between these two transitions could indicate that the branches vary quite significantly, contributing to the difference we note between the pressure broadening coefficients obtained and those reported in literature.

## 4.6. Limitations and Improvements

The sensitivities achieved with the NICE-OHMS setup demonstrated in this chapter show that the technique, for certain species, is capable of meeting the stringent detection requirements for atmospheric detection. However, within the technique, there remain intrinsic noise sources which are very difficult to eliminate entirely. The main limitation to the performance of the instrument is the varying RAM at different laser frequencies, manifesting itself as a varying background signal and non-zero vertical offset. The drift of the laser was such that subtraction of an empty cavity background signal (which would assist in the removal of the stable but present background signal) was not possible. Maintaining the lock of the laser to the cavity over the time scale needed to evacuate the cell after an absorption measurement was impossible due to disturbances it causes to the stability of the system and particularly limiting was the change in background or baseline levels with each and every lock of the laser to the cavity.

Maintaining the polarisation of the light through the EOM during the modulation process is difficult, with additional effects from temperature dependencies and laser fluctuations. The use of polarisation preserving fibers require very particular alignment to avoid inducing a phase change on the light passing through. Changing the wavelength of the laser source throughout the scan and over the course of tuning to investigate difference transitions may be sufficient to induce this change, without careful realignment at very regular intervals. Active feedback to correct the phase by a DC correction directly onto the EOM, as suggested by Wong *et al* [16] and used in the RAM removal circuit described earlier, is the best method to deal with this variation, however as has been noted, its effect was not uniform across the wavelength range investigated. The wavelength modulation portion of the setup should remove this noise, however, the bandwidth of the locking circuit was insufficient to deal with all of the fluctuations. Imbalances or disruptions to the fm triplet matching exactly the FSR of the cavity led to the noise immunity condition being broken, and amplitude modulation dominating the required signal.

Although the sensitivities presented in this chapter for this system are impressive, there are a number of improvements that could be made to further the performance of the instrument and increase its ease of use. Improvements could be made to the signal, by the use of a more powerful, highly stabilised

laser, such as an EDFL [21]. This would have the added benefit of having a much narrower laser linewidth, which would make the locking of the laser to the cavity much more simple and stable. One of the more technically challenging aspects of the NICE-OHMS setup is the locking of the laser to the cavity when it has a linewidth broader than that of the cavity modes. The locking response of the laser to the feedback is difficult to manage and so would be much easier with a narrow band fiber laser. Although problems with fiber lasers include the relatively restrictive operational wavelength range they occupy, developmental improvements mean that narrow linewidth fiber lasers exist in several wavelength ranges, corresponding to the emission windows of Yb, Er, and Tm doped fibers, i.e., from 1030 to 1121 nm, from 1525 to 1585 nm, and from 1710 to 2100 nm, respectively. These frequencies open up opportunities to study species such as $N_2O$, $CH_4$, $NH_3$, $H_2S$, $CH_2O$, and $HO_2$, although a laser is needed per species.

The optical cavity used in this NICE-OHMS setup had a relatively low finesse, compared with that of other NICE-OHMS setups. Increasing the finesse would enable higher powers to circulate within the cavity, however, the locking response of the cavity would be adversely affected and both of these factors must be considered.

## 4.7. Conclusions

In this chapter, measurements have been presented detailing the performance of an external cavity diode laser based noise immune cavity enhanced optical heterodyne molecular spectrometer (NICE-OHMS) employing a ring cavity through measurements on weak Doppler-broadened transitions of various species: $CH_4$ in the range 6595 to 6610 $cm^{-1}$, $CO_2$ around 6646 $cm^{-1}$ and $N_2O$ at 6596 $cm^{-1}$. Residual background noises have been reduced by the addition of a circuit to remove residual amplitude modulation on the pre-cavity laser radiation, resulting in improvements to the sensitivity of *fm*-NICE-OHMS in the dispersion phase by a factor of 2. The highest sensitivity achieved was $4 \times 10^{-11}$ $cm^{-1}\ Hz^{-1/2}$ being obtained for *wm*-NICE-OHMS on an unassigned $CH_4$ transition, an impressive sensitivity when considering the laser source and low finesse of the cavity. The use of the technique in order to retrieve spectroscopic information has been shown, first by the linearity of the signal strength with increasing concentration of gas, followed by the fitting of *fm*-NICE-OHMS signals at various pressures to retrieve broadening parameters for $N_2O$ and $CH_4$.

The following chapter moves on to the application of the NICE-OHMS technique to detection of $HO_2$ radicals, with a long term view to using the instrument for real time in-situ measurements.

## References


[1] L.S. Ma, J. Ye, P. Dube, J.L. Hall, *Journal of the Optical Society of America B - Optical Physics*, **16**, 2255-2268 (1999).

[2] J. Bood, A. McIlroy, and D. L. Osborn, *Journal of Chemical Physics*, **124**, 084311 (2006).

[3] F.M. Schmidt, A. Foltynowicz, W. Ma, O. Axner, *Journal of the Optical Society of America B - Optical Physics*, **24**,1392-1405 (2007)

[4] F. Schmidt, A. Foltynowicz, W. Ma, T. Lock, O. Axner, *Optics Express*, **15** (17) 10822–10831 (2007).

[5] L. Gianfrani, R. W. Fox, L. Hollberg, *Journal of the Optical Society of America B - Optical Physics*, **16**, 2247–2254 (1999)

[6] N.J. van Leeuwen, H. G. Kjaergaard, D. L. Howard, A. C. Wilson, *Journal of Molecular Spectroscopy*, **228** 83-91 (2004).

[7] N. J. van Leeuwen and A. C. Wilson, *Journal of the Optical Society of America B - Optical Physics* **21**, 1713-1721 (2004).

[8] A. Foltynowicz, W. Ma, F.M. Schmidt, O. Axner, *Journal of the Optical Society of America B* **25** 1156-1165 (2008).

[9] C. Ishibashi and H. Sasada, *Japanese Journal of Applied Physics*, Part 1 **38**, 920-922 (1999).

[10] M. S. Taubman, T. L. Myers, B. D. Cannon, and R. M. Williams, *Spectrochimica. Acta*, Part A **60**, 3457-3468 (2004)

[11] O. Axner, W. Ma, and A. Foltynowicz, *Journal of the Optical Society of America B - Optical Physics* **25**, 1166–1177 (2008).

[12] A. Foltynowicz, W. Ma, O. Axner, ,*Optics Express* **16** , 14689-14702 (2008).

[13] C.L. Bell, G. Hancock, R. Peverall, G.A.D. Ritchie, J.H. van Helden, N.J. van Leeuwen, *Optics Express* **17 (**12) 9834-9839 (2009).

[14] R. W. P. Drever, J. L. H. Hall, F. V. Kowalski, J. Hough, G.M. Ford, A. J. Munley, and H. Ward, *Applied Physics B* **31**, 97–105 (1983).

[15] R. G. DeVoe and R. G. Brewer, *Physical Review A: Atomic. Molecular and Optical Physics*. **30**, 2827-2829 (1984).

[16] N. C. Wong and J. L. Hall *Journal of the Optical Society of America B* **2**, 1527-1533 (1985)

[17] L.S. Rothman D. Jacquemart, A. Barbe, D.C. Benner, M. Birk, L.R. Brown, M.R. Carleer, C. Chackerian Jr., K. Chance, L.H. Coudert, V. Dana, V.M. Devi, J.M. Flaud, R.R. Gamache, A. Goldman, J.M. Hartmann, K.W. Jucks, A.G. Maki, J.Y. Mandin, S.T. Massie, J. Orphal, A. Perrin, C.P. Rinsland, M.A.H. Smith, J. Tennyson, R.N. Tolchenov, R.A. Toth, J. Vander Auwera, P. Varanasi, and G. Wagner, *Journal of Quantitative Spectroscopy and Radiative Transfer*, **96**, 139–204 (2005).

[18] L.-H. Deng, X.-M. Gao, Z.-S. Cao, W.-D. Chen,W.-J. Zhang, Z.-B. Gong. *Journal of Quantitative Spectroscopy and Radiative Transfer* **103** 402-410 (2007).

[19] J.Ye, L-S. Ma and J.L. Hall, *Journal of the Optical Society of America B - Optical Physics* **15** 6-15 (1998).

[20] P. Kluczynski, J. Gustafsson, A. M. Lindberg, O. Axner, *Spectrochimica. Acta B* **56** (8) 1277-1354 (2001)

[21] F.M. Schmidt, W. Ma, A. Foltynowicz, O. Axner, Applied Physics. B DOI 10.1007/s00340-010-4120-9 (2010).

[22] M.L. Silva, Ph.D. Thesis Massachusetts Institute of Technology (2002).

[23] A. Foltynowicz, J. Wang, P. Ehlers, O. Axner, *Optics Express* **18** (18) 18580-18591 (2010).

[24] V. Zeninari, B. Parvitte, D. Courtois, V.A. Kapitanov, Yu.N. Ponomarev, *Applied Physics B* **72**, 953–959 (2001) .

[25] T. Nakayama, H Fukuda, A Sugita, S Hashimoto, M Kawasaki, S Aloisio, I Morino ,G Inoue, *Chemical Physics* **334** 96–203 (2007).

# Chapter 5

# Ultra sensitive detection of $HO_2$

In addtion to presenting ultra-sensitive measurements of a NICE-OHMS system using a ring cavity, this thesis presents the first application of NICE-OHMS as an accurate and direct technique for measuring the concentration of the hydroperoxyl radical $HO_2$. In the atmosphere, $HO_2$ has a critical role in controlling the chemistry of many trace gases such as ozone, and other potentially harmful pollutants, as described in Chapter 1. Experimentally challenging measurements of short lived (of the order of <0.1 s in urban air increasing to around 1-10 s in very clean atmospheres [1]) and low concentration species are important in order to enhance atmospheric models. In this chapter, the generation scheme is presented in which $HO_2$ was formed in the cavity, by the continuous photolysis of $Cl_2$ in the presence of methanol

and oxygen. Consideration and further investigation is given to other reaction products which could potentially interfere with the desired detection of $HO_2$, followed by a discussion of the spectroscopy of $HO_2$ in the region of interest. Following spectroscopic investigation of these potentially interfering species, such as formaldehyde, a number of $HO_2$ transitions were measured with the *fm*-NICE-OHMS setup, as previously described in this thesis. Finally the minimum detection sensitivity of $HO_2$ will be discussed.

## 5.1. $HO_2$ generation

Before beginning the experimental work, the method for the generation of $HO_2$ in the optical cavity and any associated interfering species in its detection needed to be considered. This involved the kinetic modelling of the $HO_2$ generation process. $HO_2$ can be generated via a number of mechanisms, including photolysis of $Cl_2$ followed by reaction with hydrogen and oxygen [2] photolysis of $Cl_2$ followed by reaction with methanol and oxygen [2, 3], irradiation of benzene in the presence of oxygen [4], or by passing $F_2$ through a microwave discharge in the presence of $H_2O_2$ [5].

The reaction scheme for generation of $HO_2$ via photolysis of chlorine in the presence of hydrogen and oxygen results in the generation of $HO_2$ without any interfering species being also generated, with the final stage of the reaction being $H + O_2 + M \rightarrow HO_2 + M$. Although this is beneficial for detection, the $H_2 + O_2$ mixture is potentially explosive, and so the alternative method of $HO_2$ generation via chlorine atom reactions with methanol and oxygen was used. The principal reaction scheme is shown in Equations 5.1-5.3:

$$Cl_2 \xrightarrow{h\nu} Cl + Cl \qquad \textbf{Equation 5.1}$$

$$Cl + CH_3OH \rightarrow CH_2OH + HCl \qquad \textbf{Equation 5.2}$$

$$CH_2OH + O_2 \rightarrow HO_2 + CH_2O \qquad \textbf{Equation 5.3}$$

A more complete reaction scheme including all the major reactions occurring in the process of $HO_2$ formation with their rate constants is shown in Table 5.1. Detailed modelling of the $HO_2$ production and reaction scheme was undertaken in order to understand better the residence times and concentrations of the products, particularly the $HO_2$ generated, and potentially problematic species which absorb around 1.5 μm, such as formaldehyde ($CH_2O$). For the modelling, an estimate of the rate constant of the chlorine photolysis (reaction R1) is needed. Although values for the rate constant using other UV lamp

powers and configurations were available in the literature, it was necessary to determine the dissociation rate for $Cl_2$ for this particular setup and configuration.

**Table 5.1 Reactions occurring in the $HO_2$ generation with their corresponding rate constants.**

| | Reaction | Rate constant and references |
|---|---|---|
| R1 | $Cl_2 \rightarrow Cl + Cl$ | $7 \times 10^{-3}$ $s^{-1}$ [this work] |
| R2 | $Cl + CH_3OH \rightarrow CH_2OH + HCl$ | $5.5 \times 10^{-11}$ $cm^3$ $molecule^{-1}$ $s^{-1}$ [3, 6] |
| R3 | $CH_2OH + O_2 \rightarrow HO_2 + CH_2O$ | $9.1 \times 10^{-12}$ $cm^3$ $molecule^{-1}$ $s^{-1}$ [7] |
| R4 | $HO_2 + Cl \rightarrow HCl + O_2$ | $1.8 \times 10^{-11}$ $cm^3$ $molecule^{-1}$ $s^{-1}$ [8] |
| R5 | $HO_2 + Cl \rightarrow OH + ClO$ | $4.05 \times 10^{-11}$ $cm^3$ $molecule^{-1}$ $s^{-1}$ [9] |
| R6 | $HO_2 + CH_3OH \rightarrow CH_2OH + H_2O_2$ | $1.34 \times 10^{-13}$ $cm^3$ $molecule^{-1}$ $s^{-1}$ [10] |
| R7 | $HO_2 + CH_2OH \rightarrow CH_2O + H_2O_2$ | $2.01 \times 10^{-11}$ $cm^3$ $molecule^{-1}$ $s^{-1}$ [10] |
| R8 | $HO_2 + HO_2 \rightarrow H_2O_2 + O_2$ | $1.7 \times 10^{-12}$ $cm^3$ $molecule^{-1}$ $s^{-1}$ [11] |
| R9 | $Cl + CH_2OH \rightarrow CH_2O + HCl$ | $6.6 \times 10^{-10}$ $cm^3$ $molecule^{-1}$ $s^{-1}$ [12] |
| R10 | $H_2O_2 + Cl \rightarrow HCl + HO_2$ | $4.0 \times 10^{-12}$ $cm^3$ $molecule^{-1}$ $s^{-1}$ [14, 7] |
| R11 | $OH + H_2O_2 \rightarrow HO_2 + H_2O$ | $1.8 \times 10^{-12}$ $cm^3$ $molecule^{-1}$ $s^{-1}$ [6, 13] |
| R12 | $CH_2O + Cl \rightarrow HCO + HCl$ | $7.4 \times 10^{-11}$ $cm^3$ $molecule^{-1}$ $s^{-1}$ [7, 8] |

In order to photolyse molecular chlorine, 5 UV lamps were fitted in the top of the vacuum chamber, just above the bow-tie cavity, 2 cm above the beam path, beneath the Perspex lid. The spectrum of one of the lamps **(**Philips Sylvania TLD F18W black light blue tubes) was recorded using a Jobin Yvon spectrometer (CP200), with a grating groove density of 360 grooves/mm and a spectral coverage of 190 to 455 nm, dispersed over 19 mm. Knowing the power of one lamp (18 W), from this spectrum the number of photons emitted (per nm per second) was calculated. Considering the 5 lamp configuration inside the vacuum housing, the assumption was made that ¼ of the radiation from each lamp was incident on the sample. The flux of photons, $I_0(\lambda)$ ($cm^{-2}$ $s^{-1}$), was thus estimated at 2 cm below the lamps, i.e. at the beam path in the cavity. In the case of weak absorptions, as here, the Beer-Lambert law can be applied to calculate the number of photons absorbed in 1 $cm^{-3}$ in 1 s:

$$I_{ABS}(\lambda) = I_0(\lambda)\varepsilon(\lambda)cl \qquad \textbf{Equation 5.4}$$

where $\varepsilon(\lambda)$ is the wavelength dependent absorption cross section of chlorine (~ 2 x $10^{-19}$ $cm^2$), $c$ is the concentration of $Cl_2$ and $l$ is the interaction length, taken to be 1 cm. Integrating this over the wavelength of interest results in the number of photons absorbed per $cm^3$ $s^{-1}$ which corresponds to the rate of $Cl_2$ dissociated (assuming the quantum yield for photodissociation is unity). The

rate constant of chlorine atom production *k*, is defined as $\frac{d[\mathrm{Cl}]}{dt} = k[\mathrm{Cl}_2]$, and is therefore equal to $2\int_0^\infty I_0(\lambda)\varepsilon(\lambda)\, d\lambda$; this gives a rate constant for these experimental conditions of 7 x $10^{-3}$ $s^{-1}$. For a similar experiment, the rate constant for chlorine atom production has been measured as 1.35 x $10^{-3}$ $s^{-1}$ for 1 lamp [14], corresponding to a value of 6.7 x $10^{-3}$ $s^{-1}$, if 5 lamps were used. The value determined here, which uses the assumption that a geometrical factor of ¼ of the photons emitted interact with $Cl_2$, does not control the $HO_2$ concentration; modelling with this value increased by a factor of 4 led to the $HO_2$ concentration increasing by 1%, presumably because both production and loss rates of $HO_2$ are dependent upon the photon flux, and as such, it was deemed unnecessary to undertake any more technically demanding tools, such as actinometry. Figure 5.1 shows the $HO_2$ transitions in the region of interest. The $HO_2$ peak absorption cross sections in this region are typically around $\sigma = 1$ x $10^{-19}$ $cm^2$ [15], and in order to ensure that detection of $HO_2$ was successful and well within the capabilities of the NICE-OHMS spectrometer, an initial $\alpha_{min}$ of $10^{-7}$ $cm^{-1}$ was decided upon. The required concentration of $HO_2$ molecules was thus ~8 x $10^{11}$ molecules $cm^{-3}$.

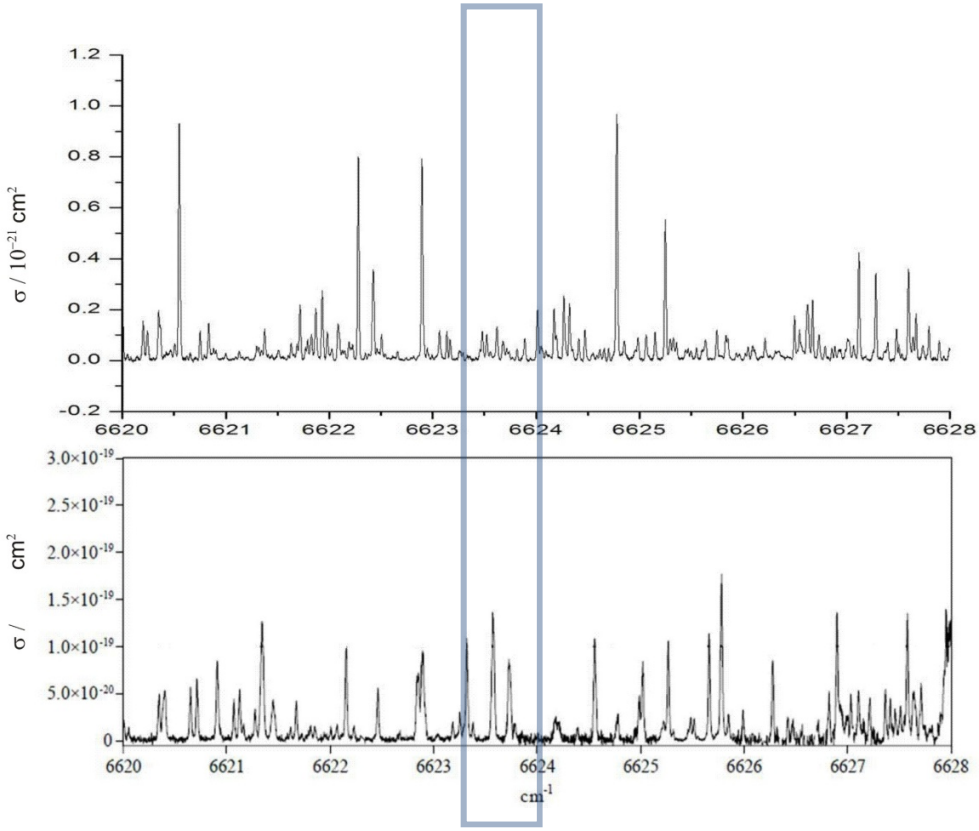


**Figure 5.1 Comparison of $H_2CO$ (top) [24] and $HO_2$ (bottom) [15] spectra in the region of interest (highlighted by blue box).**

Kinetic modelling was undertaken using simulations within Matlab, utilising the implicit ODE15s routine, to solve the differential rate equations. Initial concentrations of reactants were chosen to generate $HO_2$ at a concentration of around 8 x $10^{11}$ molecules $cm^{-3}$. The initial simulation results are shown in Figure 5.2. The simulation models continuously flowing products and reactants with the entire gas volume in the cavity being replaced every 120 seconds. The volume of the cavity was 36800 $cm^3$, with the flow rates for the reactants as follows: 18.2 sccm $Cl_2$/Ar mixture, 1.83 sccm of $CH_3OH$, 3.7 sccm of $O_2$ with the buffer gas of Ar flowing at 1719 sccm, to maintain the total pres-

sure in the cavity at ~40 Torr. From the simulation data shown in Figure 5.2, it can be seen that the concentration of formaldehyde generated is around 2 x $10^{14}$ molecules $cm^{-3}$. Given the absorption cross section of formaldehyde, this is noted as the main interfering species, and will be investigated in more detail later in the chapter.

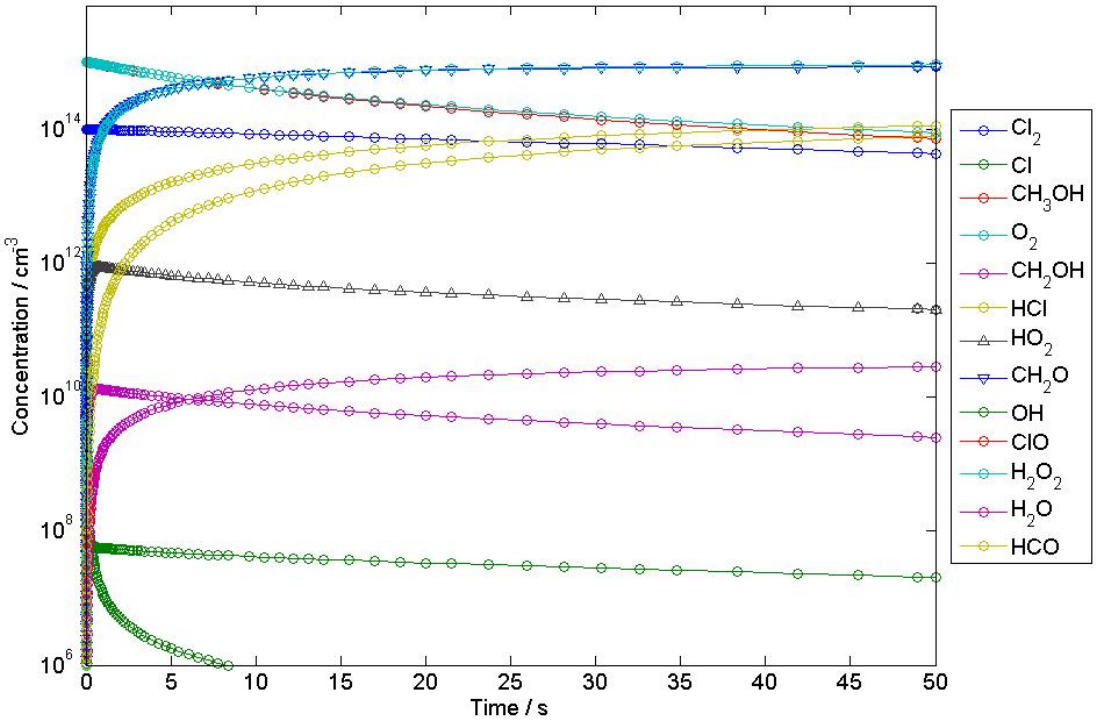


**Figure 5.2 initial simulation for $HO_2$ generation.**

## 5.2. Spectroscopy of $HO_2$

The spectroscopy of $HO_2$ has been extensively studied and reported, formerly in the UV region where the transitions are broad and overlapping [3, 16, 17, 18, 19, 20]. The commercial development of diode lasers in the near infrared

opened up the opportunity to study overtone transitions and subsequently investigations into these narrower and better resolved absorption features have been published [2, 21]. The $HO_2$ absorption bands in the near infrared regions are a vibronic progression in the low lying $^2A' \leftarrow {}^2A''$ electronic transition (for $HO_2$ at ~7017.5 $cm^{-1}$) along with the first vibrational overtone in the OH stretch (centred at 6648.9 $cm^{-1}$ for $HO_2$) [15]. It is this $2\nu_1$ band with which the work in this thesis is concerned, as, although the spectral region offers weaker line strengths than the mid-infrared region (~ 3 μm), it does however offer advantages including being less congested than in the UV, and the availability of cheap, commercially available laser sources and associated experimental optics, such as the ECDL (1480 – 1540 nm) used in this work. Previous work has reported a variety of diode laser based measurements made with diode laser experiments in the near infrared region, including DeSain *et al* [24] using WMS, Christensen *et al* for kinetic studies [22], Kanno *et al* in order to study pressure broadening coefficients [23], and Thiebaud *et al* for detailed high resolution measurement of absorption cross sections of $HO_2$ [15]. The two absorption features selected for investigation in this work are highlighted in Figure 5.1 by the blue box. The lines have been assigned by DeSain *et al* [24] with the absorption feature at 6623.32 $cm^{-1}$ arising from the $^qP_1(12)$ transition and the feature at 6623.57 $cm^{-1}$, arising from the $^qP_2(8)$ + $^qP_2(9)$ transitions; the tran-

sitions are labelled according to $^{\Delta Ka}\Delta J_{Ka''}(N'')$ where N is the rotational angular momentum quantum number, J is the sum of the rotational and spin angular momentum quantum numbers given by N ± ½, and $K_a$ is the quantum number for rotation about the a axis of the molecule as defined in reference [24]. The lines chosen, as can be seen in Figure 5.1, show minimal (but non zero) interference from formaldehyde absorption. From the simulations undertaken, the following concentrations (with their respective peak absorption cross sections) were obtained:

At 6623.52 $cm^{-1}$, $H_2CO$ concentration of 2 x $10^{14}$ molecules $cm^{-3}$ with $\sigma_{peak}$ = 9.9 x $10^{-23}$ $cm^2$

At 6623.57 $cm^{-1}$, $HO_2$ concentration of 8 x $10^{11}$ molecules $cm^{-3}$ with $\sigma_{peak}$ = 1.3 x $10^{-19}$ $cm^2$.

Considering the absorption cross section and concentrations involved, it was noted that distinguishing between $HO_2$ and $H_2CO$ may be problematic as both may give a similar absorbance given the uncertainty in the modelling (approximately 5 x $10^{-8}$ $cm^{-1}$), and in addition to further knowledge of the absolute frequency scale provided by a wavemeter, more detailed investigation would be required to confirm that the absorption features measured are due to $HO_2$, as will be presented in section 5.4.

## 5.3. Experimental

A schematic of the experimental setup is shown in Figure 4.1, with the only difference being the introduction of UV lamps, suspended from the cavity lid, and the addition of flow controllers for the gas handling. The radiation source used in the experiment was an external cavity diode laser (ECDL) operating at 6623.32 $cm^{-1}$ (1510 nm), with a power of around 2 mW emitted by the laser. The ECDL was operated at 32.2 $^{o}C$, with a current of 100 mA and scanned with a sinusoidal ramp of 1.8 V peak-to-peak at a frequency of 0.532 Hz giving a scan range of 12 GHz.

The reaction scheme has been outlined previously in section 5.2.1 and the flow rates for the input gases calibrated. Due to the large voltages required to start the lamps (900 V) and considering the Paschen Curves (relating the break-down voltage, distance between conducting pins and pressure of gas) for Argon and the small distance between the feed-through pins for the lamps inside the vacuum housing, it was not sensible to turn the lamps on at pressures lower than 760 Torr without a spark ensuing. As a result, they were turned on in a high pressure atmosphere of nitrogen to negate this electrical shorting issue. The steel and Perspex vacuum assembly housing the ring cavity was first evacuated, to $10^{-4}$ Torr, before being filled to 760 Torr with nitrogen. After switching on the lights, the chamber was evacuated to a pressure of 40 Torr

and the flows of constituent gases started. Flows of 1% $Cl_2$ in Ar (certified purity 1.00% in Argon balance) , $O_2$ (BOC certified purity 99.5%) and Ar (BOC Pureshield 99.998% purity) were controlled by mass flow controllers (Tylan FC-260), with flows of $CH_3OH$ vapour being controlled through a calibrated needle valve. Pressures inside the reaction cell were measured with two capacitance manometers (MKS instruments 0-100 Torr and 0-760 Torr) attached to the cell, with the total pressure in the cell of reactants and buffer gas (Ar) being controlled actively with a valve (Edwards Speedivalve SP25) in the exit path before the pump. The pump rate ensured that the gases in the cavity were replaced every 120 seconds.

With the flows and lamps on, the locking procedure was implemented, as outlined in the previous chapter. In an identical way to that outlined in chapter 2, the cavity finesse was determined using an unassigned $CH_4$ transition at 6623.18 $cm^{-1}$ returning a finesse of 2800 ± 200.

## 5.4. Results

Results obtained for *fm*-NICE-OHMS on $HO_2$ and associated reaction products are presented in the following section. Firstly, in order to ensure that $HO_2$ was being generated and detected, results are presented for formaldehyde, which

had the potential to interfere with the $HO_2$ detection process. Following this, results for detection of $HO_2$ are presented for a number of transitions, with the data fitted and calibrated to obtain concentrations. Finally, the kinetics of the $HO_2$ reaction sequence is also investigated and compared with simulations, in order to definitively prove that $HO_2$ was indeed generated and detected.

### 5.4.1. Investigation into the interference of $H_2CO$

Given the similarity in the calculated Doppler widths of both the $HO_2$ (427 MHz) and $CH_2O$ (448 MHz) absorption features in the region of interest, fitting the absorption features alone does not definitively prove that $HO_2$ is generated, and so further investigation must be undertaken, involving accurately measuring the positions of the line centres, relative to one another to investigate whether $HO_2$ can be selectively identified.

A sample of 5 Torr of formaldehyde gas was prepared by thermal decomposition of paraformaldehyde, as described by Spence and Wild [25]. The purity of the sample was estimated to be >95%, using an FTIR calibration [26], and absorption cross section comparisons with FTIR measurements by Gratien *et al*, [27], for the identical method of formaldehyde preparation. 50 mTorr of $H_2CO$ was admitted into the cavity, following which an *fm*-NICE-OHMS sur-

vey spectrum was carried out. Given the expected concentrations of $H_2CO$ predicted by the kinetic model (~30 mTorr), 50 mTorr of $H_2CO$ was used in the cavity for the survey spectrum, to determine the expected signal level should $H_2CO$ production be a significant interference issue. Figure 5.3 shows the series of short scans (indicated by the change in colours of the upper trace) which were undertaken around the 6623.1 to 6623.9 $cm^{-1}$ region, with the purple trace showing the continuous spectrum taken from Staark *et al* [28], and the black trace showing its first derivative.

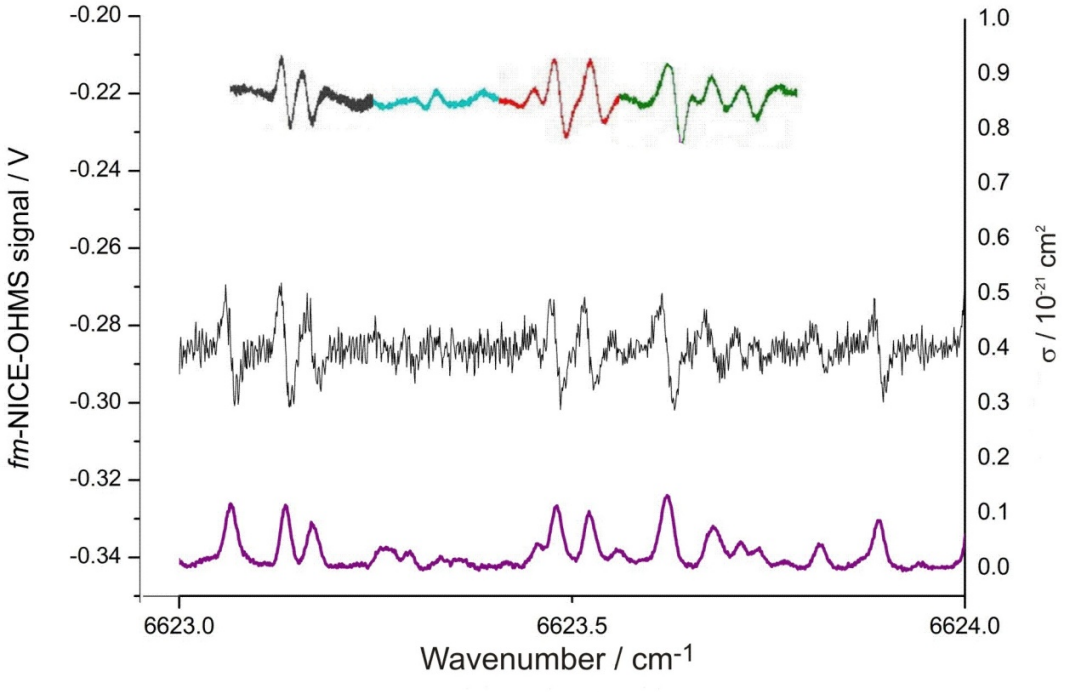


**Figure 5.3 *fm*-NICE-OHMS survey spectrum of 50 mTorr formaldehyde in the spectral region of interest (upper trace) and $H_2CO$ spectrum taken with CEAS from Staark *et al* [28] (lower trace) and its first derivative (black).**

The spectra collected from the 50 mTorr of formaldehyde clearly show the spectral features which are identified and characterised in the Staark spectrum. The unassigned formaldehyde spectrum was noted to be very congested but the $H_2CO$ transitions are tentatively assigned to transitions in the $3_1 4_2 5_1$ combination band centred at 6635.7 $cm^{-1}$ [28]. To verify whether $H_2CO$ would indeed interfere in the detection of $HO_2$ and to verify that $HO_2$ has been generated, a more specific localised investigation of the spectral region around both the $HO_2$ absorption features identified as suitable for study, at 6623.32 and 6623.57 $cm^{-1}$, respectively (assignments in section 5.3) was performed.

Two short scans of ~0.1 $cm^{-1}$ were completed around the $HO_2$ features of interest, with the resultant traces shown in Figure 5.4 and Figure 5.5. In both cases, two experimental runs were undertaken, comprising one with the $HO_2$ generation process in operation, as described previously, followed by one with the cavity evacuated and then filled with 50 mTorr of $H_2CO$. In both cases, the wavemeter (Burleigh WA-1000) was used to record the frequency limits of the scan, and these were the same for both the $HO_2$ and the $H_2CO$ runs. In both figures, the lower (blue) trace shows the absorption feature from 50 mTorr $H_2CO$, with the upper (black) trace showing the absorption feature from the $HO_2$.

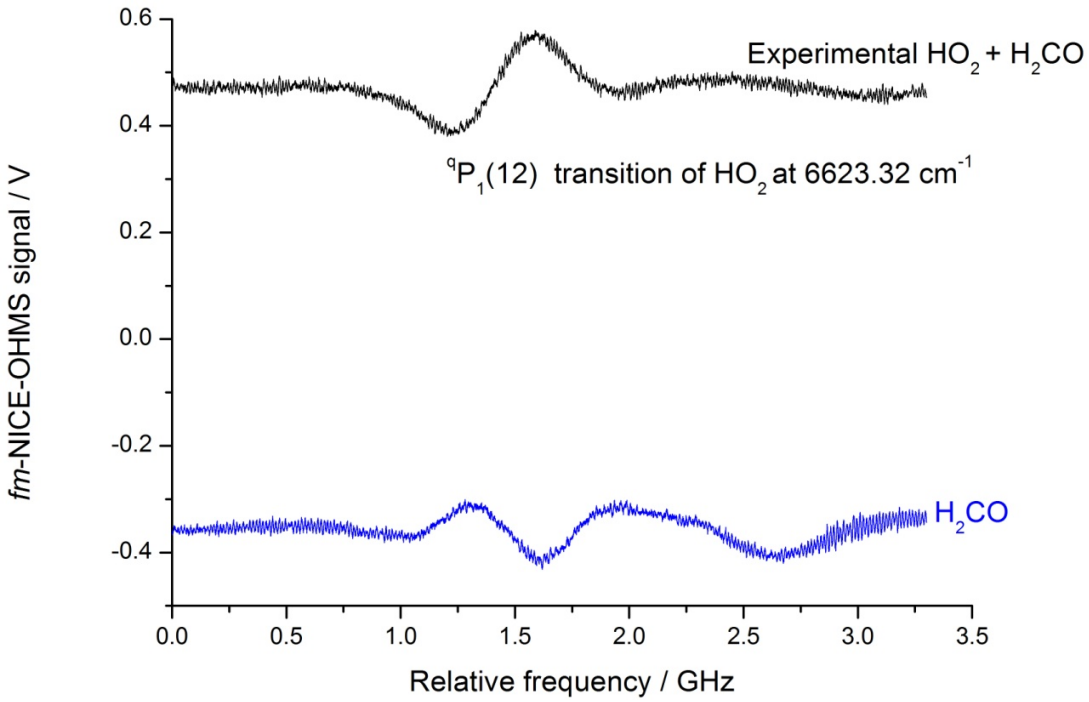


**Figure 5.4 $HO_2$ (upper) and $H_2CO$ (lower) absorption features in region 6623.28 to 6623.39 $cm^{-1}$ with data offset in the y direction for clarity.**

It is clear that the $HO_2$ absorption features at 6623.32 and 6623.57 $cm^{-1}$ are not affected by the presence of an $H_2CO$ feature at higher relative frequencies. The modelled concentration of $H_2CO$ shown in Figure 5.2 indicates that around 3 x $10^{14}$ molecules $cm^{-3}$ would be generated. The corresponding signal from this would be clearly visible on the scans; however, considering the data in Figure 5.5 in particular, the formaldehyde features are not evident. Considering the noise level on the baseline of the $HO_2$ data, it can be inferred that the concentration of $H_2CO$ is less than 6 x $10^{13}$ molecules $cm^{-3}$, compared with the modelled estimated concentration of 3 x $10^{14}$ molecules $cm^{-3}$.

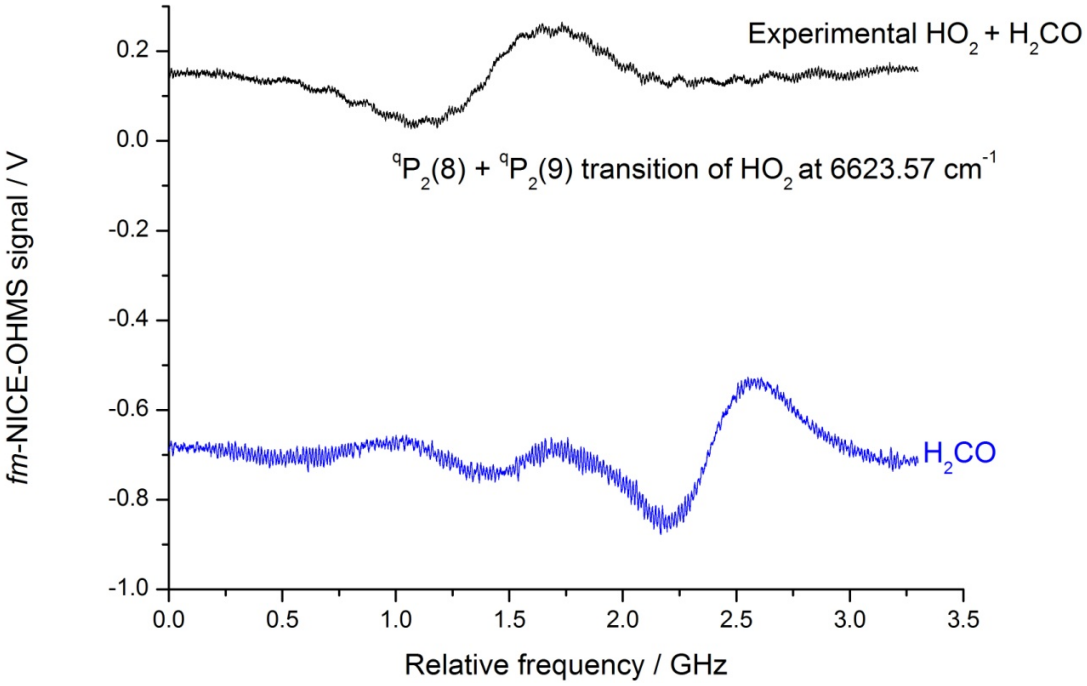


**Figure 5.5 $HO_2$ (upper) and $H_2CO$ (lower) absorption features in region 6623.51 to 6623.60 $cm^{-1}$ with data offset in the y direction for clarity.**

From this, we must conclude that there is a more significant loss process of $H_2CO$ operating than was initially incorporated into the simulation.

Consideration was given to the diffusion of $H_2CO$ to the cell walls as it is known to cause problems of sticking to surfaces. The surface loss time ($\tau_{surf}$) of $H_2CO$ due to diffusion to and absorption on the walls was estimated using the method outlined by Chantry *et al* [29], where:

$$\tau_{surf} = \frac{\Lambda_0^2}{D} + \frac{4l_0}{\nu}\frac{(1-\beta/2)}{\beta}$$ **Equation 5.5**

where $v = \sqrt{8k_bT_{gas}/\pi m}$ is the mean speed with Boltzmann constant $k_b$, mass of species $m$, and gas temperature $T_{gas}$. The diffusion constant $D$ was taken to be 1.6 x $10^{-5}$ $m^2$ $s^{-1}$ at 298 K [30]. The diffusion geometry ($\Lambda_0$) was calculated for the rectangular steel cell [29], with $l_0$ being the volume/surface area ratio for the cell and $\beta$ being the sticking coefficient for formaldehyde (taken as the same as $NH_3$ = 0.2 [31] as no literature values are known). The resulting time taken for the $H_2CO$ to diffuse to and absorb on the walls was 1.48 seconds. This value is much shorter than the pump out rate of the cell, 120 seconds, and could account for the much reduced concentration of $H_2CO$ resulting than that originally modelled. Refining the model with the inclusion of an additional loss term for the $H_2CO$ results in the predicted concentrations shown in Figure 5.6. Figure 5.6 shows that the $H_2CO$ concentration drops below the detection limit of 6 x $10^{13}$ molecules $cm^{-3}$ after 20 seconds, when the measurements were taken, and accounts for the lack of signal from $H_2CO$.

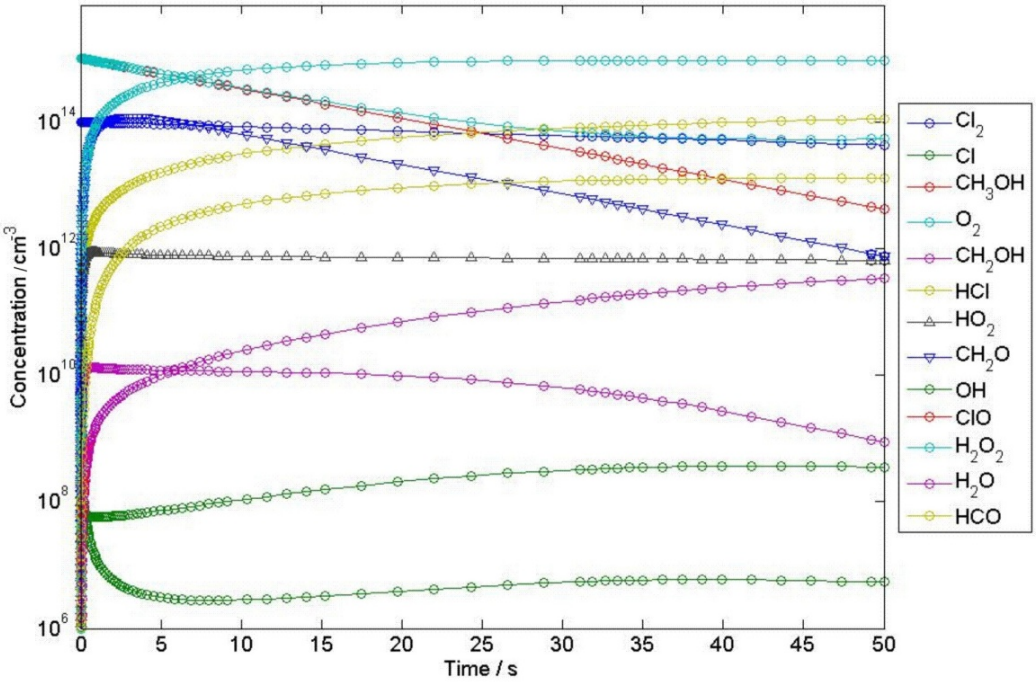


**Figure 5.6 Simulation including loss rate of $H_2CO$ to the walls.**

As the absolute concentration of $H_2CO$ in the experiments above was known, and with both of the data sets being taken at the absorption phase, the relative heights of the signals for both species were compared, to confirm that the $HO_2$ concentration is as expected from the model. In this case, the $HO_2$ concentration used is that calculated from the modelling, and the height of the expected signal X from this estimated concentration can be estimated, and then compared to the signal retrieved, with the data given in Table 5.3.

**Table 5.2 Calibration data for $HO_2$ with $H_2CO$ as the reference species.**

| Species | Peak height / V | Line position/ $cm^{-1}$ | σ peak / $cm^2$ | Concentration /$cm^{-3}$ |
|---|---|---|---|---|
| $HO_2$ | *X* | 6623.57 | $1.3 \times 10^{-19}$ | $8 \times 10^{11}$ (calculated) |
| $H_2CO$ | 0.31 | 6623.52 | $9.89 \times 10^{-23}$ | $1.65 \times 10^{15}$ (measured) |

From this, *X* (the estimated size of the $HO_2$ signal expected) is 0.20 V. From the data in Figure 5.5, the measured peak to peak signal height is 0.21 V, which corresponds well to the estimate.

## 5.4.2. Analysis of $HO_2$ results

Figure 5.7 shows an *fm*-NICE-OHMS spectrum of $HO_2$ at 6623.32 $cm^{-1}$, where the peak absorption cross section is $\sigma = 9.7 \times 10^{-20}$ $cm^2$. A fit to the absorption feature is shown in red, and the returned Gaussian width of 426 MHz ± 15 MHz (FWHM) agrees well with that calculated for Doppler broadened $HO_2$ of 427 MHz. The data showed no indication of pressure induced line broadening.

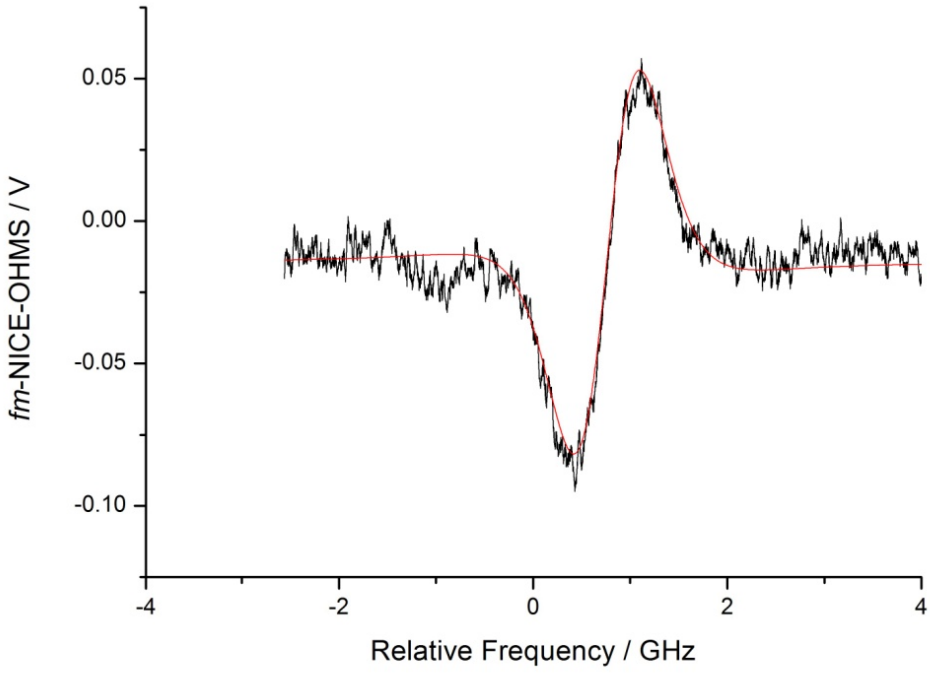


**Figure 5.7 *fm*-NICE-OHMS spectrum of $HO_2$ on the $^qP_1(12)$ transition at 6623.32 $cm^{-1}$, with a fit to the data shown in red.**

The data were calibrated against a known concentration of a different absorber, $CH_4$, in the same spectral region and taken at a similar time to the $HO_2$ measurement. The methane transition chosen was the 6623.185 $cm^{-1}$ transition, with a peak absorption cross section of $\sigma = 1.685 \times 10^{-23}$ $cm^2$. With 1.98 Torr of $CH_4$ in the cavity, the *fm*-NICE-OHMS spectrum was taken and is shown in Figure 5.8.

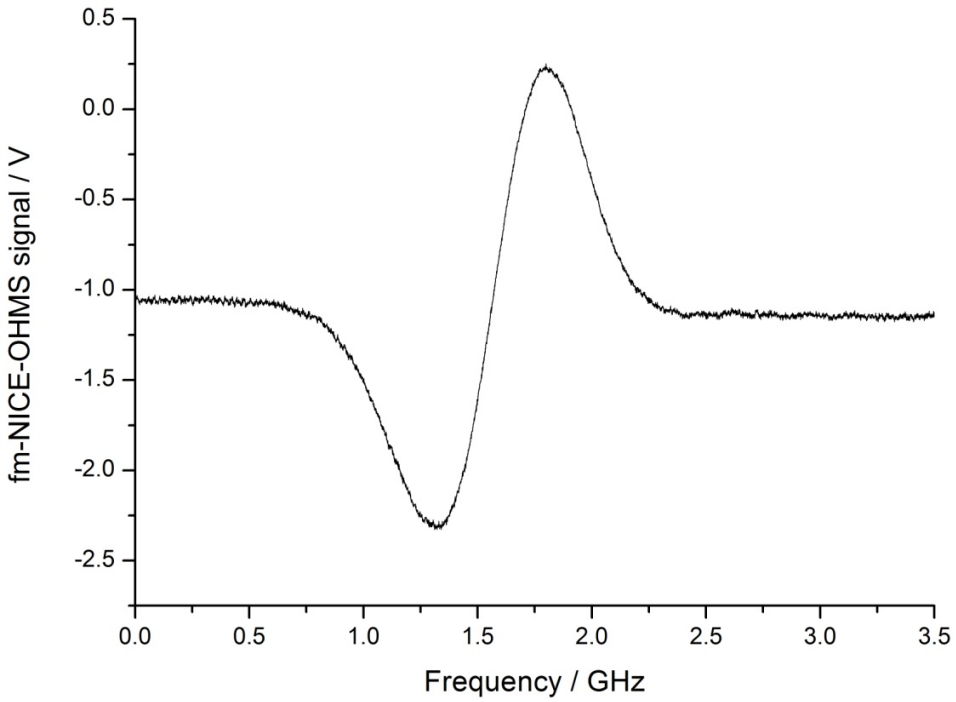


**Figure 5.8 *fm*-NICE-OHMS spectrum of 1.98 Torr $CH_4$ at 6623.185 $cm^{-1}$ used for $HO_2$ calibration.**

With both the datasets being taken at the same phase (absorption), the relative heights of the signals and the peak absorption cross sections were compared for the calibration, with the data given in Table 5.3.

**Table 5.3 Calibration data for $HO_2$ with $CH_4$.**

| Species | Peak height / V | Line position / $cm^{-1}$ | σ peak /$cm^2$ | Concentration /$cm^{-3}$ |
|---|---|---|---|---|
| $HO_2$ | 0.14 | 6623.32 | $1.3 \times 10^{-19}$ | $C_{HO_2}$ |
| $CH_4$ | 2.55 | 6623.18 | $1.685 \times 10^{-23}$ | $6.42 \times 10^{16}$ |

The concentration of $HO_2$ was determined to be $4.55 \times 10^{11}$ $cm^{-3}$. Figure 5.6 shows that the simulated values matched the experimental yield of $HO_2$ rea-

sonably well. Using this calibrated $HO_2$ concentration and the S/N ratio of 38 determined in Figure 5.8, a minimum detection sensitivity of ~ 4 x $10^{10}$ radicals $cm^{-3}$ can be inferred, leading to a minimum detection sensitivity of 1.8 x $10^{-9}$ $cm^{-1}$. Comparing this value with those given in Chapter 4, it can be seen that the sensitivity reported here is an order of magnitude lower than those reported for *fm*-NICE-OHMS in Chapter 4. These measurements were conducted towards the end of the lifetime of the laser source, which was suffering degradation from the repeated modulation over several years. The setup was also not working under optimal conditions as one of the piezo-electric transducers received an erroneously large voltage which reduced its performance, and meant that no WMS could be performed at this stage.

### 5.4.3. $HO_2$ kinetics analysis

As a further confirmation that the species produced and detected from the photolysis experiments in the cavity are $HO_2$, a kinetic analysis was undertaken. Firstly, analysis of the time taken for the $HO_2$ signal to disappear following the shutting off of the chlorine flow, and secondly, analysis of the time taken for the $HO_2$ signal to disappear following the switching off of the UV lamps were investigated.

The input flow rates for the flow controllers were set so that the residence time in the cavity was 120 seconds. Once all the flows were on and the laser was locked and stable with *fm*-NICE-OHMS data being collected on $HO_2$, the chlorine flow was turned off. As the lamps remain on during this time, the photolysis reaction of $Cl_2$ → 2Cl continues and it is this which is driving the formation of $HO_2$ until all of the $Cl_2$ is used or pumped away.

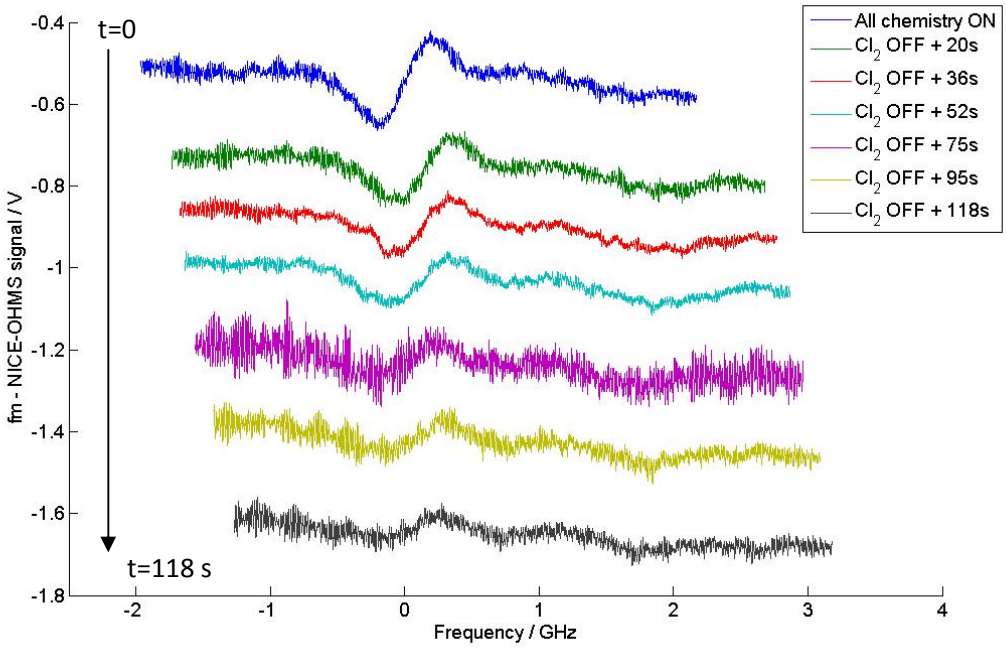


**Figure 5.9 *fm* NICE-OHMS data recorded over 2 minutes following the shutting off of the chlorine flow (data offset in the y direction for clarity).**

The laser remained locked, with all the other flows on, and data from scans over the same $HO_2$ peak region (6623.32 $cm^{-1}$) were taken at approximately 20 second intervals. These data are shown in Figure 5.9 and have been offset in

the y-direction for clarity. It can be seen from the data in Figure 5.9 that over the 120 seconds following the shutting off of the chlorine flow, the concentration of $HO_2$ drops steadily as the remaining chlorine in the cavity is removed by pump out.

The formaldehyde creation reactions would also continue during this time, and so the kinetic evidence for $HO_2$ generation needs to be augmented in order to completely rule out $H_2CO$ as the product under investigation. This can be achieved by quickly stopping the $Cl_2 \rightarrow 2Cl$ reaction which drives the scheme, by turning off the UV lamps. The $H_2CO$ is a stable species and so it remains in the cavity, whereas $HO_2$ is rapidly lost, and hence, if the photolysis process was ended, an immediate loss of $HO_2$ should be detected; this would be convincing evidence that $HO_2$ was under investigation, rather than $H_2CO$.

Modelling of this scenario where the lamps were turned off, was undertaken in Matlab, following the same scheme as outlined earlier in this chapter and is shown in Figure 5.10. The model was stopped at 10 seconds, and then re-started again with the rate constant for the chlorine photolysis set at 0, hence simulating turning off the lamps, and allowing the model to continue to run.

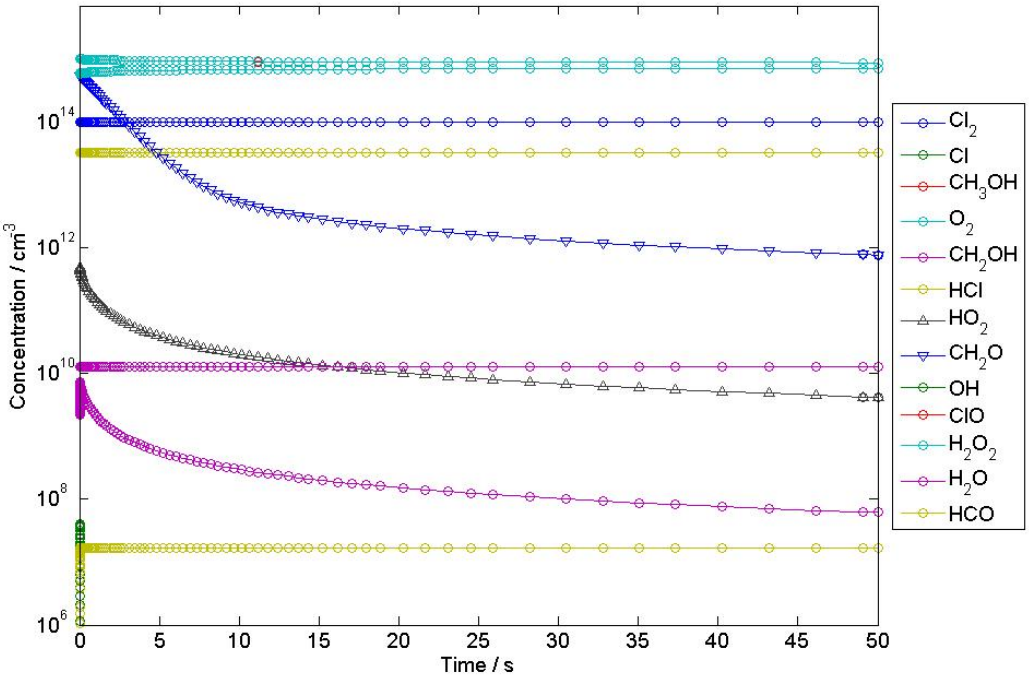


**Figure 5.10 $HO_2$ simulation with the lamps turned off, k=0 for $Cl_2$-->2Cl.**

The simulated model results for this are shown in Figure 5.10. It can be seen that the concentration of $HO_2$ drops to below the minimum detectable level (4 x $10^{10}$ molecules $cm^{-3}$ – see section 5.4.1) after about 4 seconds. This was experimentally verified by measurement of the decay of the $HO_2$ peak after the lamps were switched off. The results are shown in Figure 5.11 with the red line being the $HO_2$ concentration from the simulation shown in Figure 5.10. It can be clearly seen from Figure 5.11 that the red trace, showing the results of simulations for the losses of $HO_2$ via the reactions outlined in Table 5.1 [7, 8, 9, 11], shows good agreement with the measured decay of $HO_2$ (black circles).

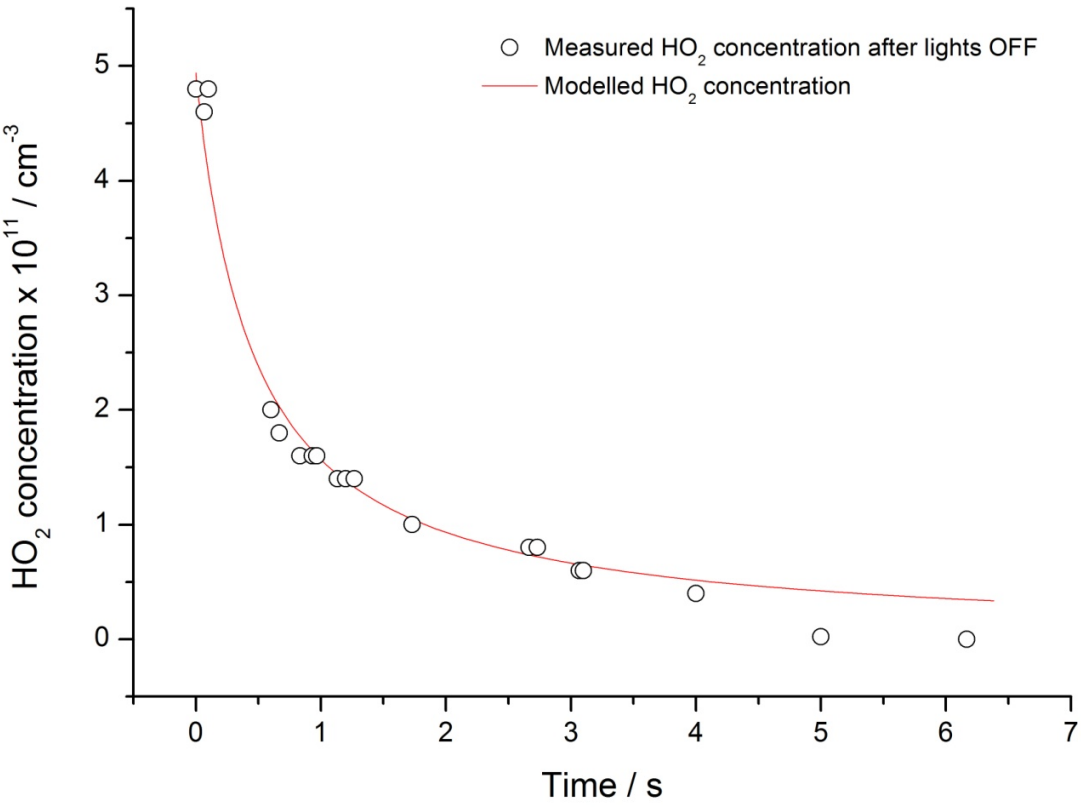


**Figure 5.11 - $HO_2$ concentration vs. time after UV lamps turned off with the modelled $HO_2$ concentrations.**

This is further convincing evidence that the species being measured is indeed $HO_2$ as intended, and not formaldehyde.

## 5.5. Discussion and Conclusions

The NICE-OHMS spectrometer developed and characterised in Chapter 4 has been successfully applied to the detection of $HO_2$. Although the aim of detecting $HO_2$ at atmospheric levels was not realised, a minimum detection level of 4 x $10^{10}$ molecules $cm^{-3}$ has been demonstrated, giving a minimum detection

sensitivity of 1.8 x $10^{-9}$ $cm^{-1}$. The sensitivity reported for the detection of $HO_2$ in this chapter is not as high as for the detection of $CH_4$ previously reported in chapter 4. This decline in sensitivity has probably occurred due to the PZT and laser in the setup degrading. It may seem that the application of NICE-OHMS to atmospheric $HO_2$ detection is inadequate, due to the required sensitivity not being realised, with the current work being three orders of magnitude off the required sensitivity (2 x $10^{-12}$ $cm^{-1}$). However, a number of factors must be considered. From the data in Chapter 4, it would be expected that at least one order of magnitude increase in sensitivity would be attained, should WMS be applied. Considering the sensitivity values obtained in Chapter 4, it is also evident that a further loss of an order of magnitude has resulted from the laser degradation. Further increases in detection sensitivity along with increased ease with which the laser locking could be achieved would involve the incorporation of a narrow band higher power source, such as an erbium doped fiber laser (EDFL) with a much narrower free-running linewidth of 1 kHz. Not only would the locking be achieved more easily, the amount of power circulating the cavity would also be increased with the higher power laser source, thereby offering further improvements to the detection sensitivity. However, this is tempered with the reduction in wavelength flexibility that an EDFL offers over a broadly tunable ECDL, as currently in use, meaning

fewer transitions could be investigated. Should the above improvements be made, the use of higher reflectivity mirrors could subsequently be implemented, leading to the required sensitivity for detection of atmospheric $HO_2$ being attained.

This work marks the first application of a NICE-OHMS spectrometer to detection of radical species, and marks a key step in applying this ultra-sensitive spectrometer to real atmospheric scenarios. One of the key features of a detection technique most useful to atmospheric detection scientists is one which utilises a direct and speciated solution. It has been demonstrated in this chapter, that the NICE-OHMS spectrometer can provide this on application to $HO_2$. One main drawback with the current NICE-OHMS setup as described here is the laser source used in the setup. Although having a broad range, with a tunable ECDL allowing greater flexibility in the selection of the detection wavelength, the relatively large linewidth (2 MHz) of the laser locking system adds a further level of experimental complexity to the system. With improvements to the laser source and improvements to the piezo-electric transducers to return the system to its optimal operating conditions, NICE-OHMS offers a viable spectrometer for application to atmospheric remote sensing situations.

## References

[1] X. Ren, H. Harder, M. Martinez, R.L. Lesher, A. Oliger, J.B. Simpas, W.H. Brune, J.J. Schwab, K.L. Demerjian, Y. He, X.L. Zhou, H.G. Gao, *Atmospheric Environment*, **37**, 3639-3651 (2003)
[2] T.J. Johnson, F.G. Wienhold, J.P. Burrows, G.W. Harris, H. Burkhard, Journal of Physical Chemistry, **95**, 6499-6502 (1991)
[3] C.A. Taatjes, D.B. Oh, *Applied Optics*, **36**, 5817-5821 (1997)
[4] A. Aluculesei, A. Tomas, C. Schoemaecker, C. Fittschen, *Applied Physics B - Lasers and Optics*, **92**, 379–385 (2008)
[5] S. Aliosio, J.S. Francisco, R.R. Friedl, *Journal of Physical Chemistry A*, ***104***, 6597-6601 (2000)
[6] M.E. Jenkin, M.D. Hurley, T.J. Wallington, *Physical Chemistry Chemical Physics*, **9**, 3149-3162 (2007)
[7] B. Hanoune, S. Dusanter, L. ElMaimouni, P. Devolder, B. Lemoine, *Chemical Physics Letters*, **343**, 527-534 (2001)
[8] S.P. Sander, R.R. Friedl, Jet Propulsion Laboratory, http://jpldataeval.jpl.nasa.gov (2003)
[9] V. Riffault, Y. Bedjanian, G. Le Bras, International Journal of Chemical Kinetics, **33**, 317-327 (2001)
[10] P.D. Lightfoot, B. Veyret, R. Lesclaux, *Chemical Physics Letters*, **150**, 120-126 (1988)
[11] A.C. Noell, L.S. Alconcel, D.J. Robichaud, M. Okumura, S. P. Sander, *Journal of Physical Chemistry A*, **114**, 6983–6995 (2010)
[12] S. Dóbé, M. Otting, F. Temps, H.G. Wagner, H. Ziemer, *Berichte der Bunsen-Gesellschaft-Physical Chemistry Chemical Physics*, **97**, 877–883 (1993)
[13] G.D. Hayman, F Battin-Leclerc, *Journal of the Chemical Society, Faraday Transactions*, **91**, 1313-1323 (1995)
[14] J.P. Burrows, G.S. Tyndall, G.K. Moortgat, *Journal of Physical* Chemistry, **89**, 4848-4856 (1985)
[15] J. Thiebaud, S. Crunaire, C. Fittschen, *Journal of Physical Chemistry A*, ***111***, 6959-6966 (2007)
[16] O.J Nielson, M.S. Johnson, T.J. Wallington, L.K. Christensen, J. Platz, *International Journal of Chemical Kinetics*, **34**, 283-291 (2002)
[17] D. Stone, D.M. Rowley, *Physical Chemistry Chemical Physics*, **7**, 2156-2163 (2005)
[18] M.S. Zahniser, A.C. Stanton, *Journal of Chemical Physics*, **80**, 4951–4960 (1984)
[19] M.S. Zahniser, K.E. McCurdy, A.C. Stanton, *Journal of Physical Chemistry*, **93**, 1065–1070 (1989)
[20] M.E. Jenkin, R.A. Cox, G.D. Hayman, L.J. Whyte, *Journal of the Chemical Society, Faraday Transactions 2*, **84**, 913 (1988)
[21] E.H. Fink and D.A. Ramsay, *Journal of Molecular Spectroscopy*, **185**, 304-324 (1997)
[22] L.E. Christensen, M. Okumura, S.P. Sander, R.R. Friedl, C.E. Miller, J.J. Sloan, *Journal of Physical Chemistry A*, **108**, 80-91 (2004)
[23] N. Kanno, K. Tonokura, A. Tezaki, M. Koshi, J. Mol. Spectrosc, **229**, 193-197 (2005)
[24] J. D. DeSain, A.D. Hob, C.A. Taatjes, *Journal of Molecular Spectroscopy*, **185**, 163-169 (2003)
[25] R. Spence, W. Wild, *Journal of the Chemical Society*, 338 -340 (1935)
[26] M.B. Crow, A. Gilchrist, G. Hancock, R. Peverall, G. Richmond, G.A.D. Ritchie, S.R. Taylor, *Journal of Physical Chemistry A*, **113**, 6689–6696 (2009)
[27] A. Gratien, E. Nilsson, J.-F. Doussin, M. S. Johnson, C.J. Nielsen, Y. Stenstrom, B.J. Picquet-Varrault, *Journal of Physical Chemistry A*, **111**, 11506-11513 (2007)
[28] M. Staark, E.W. Gash, D.S. Venables, A.A Ruth, *Journal of Molecular Spectroscopy*, **229**, 115-121 (2005)

[29] P.J. Chantry, Journal of Applied Physics **62** , 1141 - 1148 (1987)
[30] R.W. Gillett, H.K Reibich, G.P. Ayers, *Environmental Science & Technology*, **34**, 2051-2056 (2000)
[31] A. Scheibe, U. Lins, R. Imbihl, *Surface Science*, **577**, 1-14 (2005)

# Chapter 6
# Future directions

This thesis has demonstrated the use of an external cavity diode laser based NICE-OHMS system, and its application to detection of a range of species of atmospheric importance. This work demonstrates the highest sensitivity to date for this type of laser source, and also presents the first measurements of radical species, with the production and detection of $HO_2$ being performed in the optical cavity. The sensitivity for the detection of $CH_4$ was $4 \times 10^{-11}$ $cm^{-1}$ $Hz^{-1/2}$ which clearly demonstrates the impressive sensitivities which such an instrument can deliver.

As described in the previous chapter, the experimental sensitivity limit achieved for detection of $HO_2$ was 1.8 x $10^{-9}$ $cm^{-1}$, which was not sufficiently sensitive to achieve detection of atmospheric levels. However, were improvements to the system made, then there is significant and real potential that these limits would be achieved. In the current setup, there are two main limitations – the laser source and the piezo electric transducer. The ECDL source currently used is of very low power and not particularly narrow linewidth, and so achieving and maintaining the lock of the laser to the cavity during the wavelength scanning for data acquisition is difficult. With the implementation of an improved laser source, such as an erbium-doped fiber laser (EDFL), this would be improved as the much narrower line width of the laser would be more easily locked to the cavity. Higher powers would also improve the signal size with an associated reduction in the shot noise limit for the setup. The current sensitivity was achieved with a cavity of relatively low finesse, which could be improved by the use of higher reflectivity mirrors; it should be noted however that this will change the locking response of the cavity. Although the implementation of a narrow line width EDFL would improve the ease of locking, due to the spectral coverage limitations of such laser sources, a wider tuning range would be required which may be beyond the performance limits of the laser in the atmospheric pressure broadened regime.

Recent work has extended investigations of different laser sources to include distributed feedback lasers (DFB) which offer a wider and fast tuning range [1], or quantum cascade lasers (QCLs) whereby access could be gained into wavelength ranges corresponding to the fundamental molecular vibrational transitions [2].

Although impressive sensitivities have been demonstrated with the use of the technique, the fact that there are so few NICE-OHMS setups in existence indicates that the implementation of the systems is challenging. However, the benefits of using the technique are clear (i) an intrinsic noise immunity to laser frequency imperfections, (ii) impressive sensitivities demonstrated with a range of laser sources, (iii) the detection of both pressure broadened and sub Doppler signals and (iv) the option to measure both absorption or dispersion signals at arbitrary phase angles [3]. The NICE-OHMS technique is still in its developmental stages, and now that the experimental complexities have mostly been overcome, moves to miniaturise the system in order to make measurements in various locations, e.g. in field instrumentation or medical diagnostics can be considered.

Comparisons between techniques which also offer the potential of achieving such sensitivities, such as cavity ring down spectroscopy (CRDS) are inevita-

bly made. Consideration might be given to experimental complexity and economic outlay, relative to the gains in sensitive which can be achieved. Developments in CRDS, such as frequency locking continuous wave CRDS are capable of achieving sensitivities of 1 x $10^{-12}$ $cm^{-1}$ $Hz^{-1/2}$ [4] however, these gains in sensitivities still require complex and demanding experimental techniques, with more simple setups only capable of achieving sensitivities in the ranges $10^{-9}$ -$10^{-10}$ $cm^{-1}$ [5]. However, where truly ultrasensitive detection is required, for example in atmospheric trace gas detection, the potential that NICE-OHMS offers is unrivalled. With the majority of the experimental work in achieving the high sensitivities now undertaken and published, and with the development of more suitable lasers at a more economic price range, the unrivalled sensitivity which NICE-OHMS has to offer as an absorption based technique should continue to be pursued in the field of atmospheric detection.

## References

[1] A. Foltynowicz, J. Wang, P. Ehlers, O. Axner, *Optics Express* **18 (**18) 18580-18591 (2010).
[2] M. S. Taubman, T. L. Myers, B. D. Cannon, and R. M. Williams, *Spectrochimica. Acta, Part A* **60**, 3457-3468 (2004).
[3] A. Foltynowicz, W. Ma, F.M. Schmidt, O. Axner, *Applied Physics B* **92** 313-326 (2008).
[4] T. G. Spence, C. C. Harb, B. A. Paldus, R. N. Zare, B. Willke, R. L. Byer, *Review of Scientific Instruments* **71**, 347- 353 (2000).
[5] J. Morville, D. Romanini, A.A. Kachanov, M. Chenevier, *Applied Physics B* **78**, 465-476 (2004).